The Dissertation Committee for Michael Scott Daugherity
certifies that this is the approved version of the following dissertation:

Two-Particle Correlations in Ultra Relativistic Heavy Ion Collisions

Committee:

Gerald Hoffmann, Supervisor

Alexander Huk

Christina Markert

Robert Ray

Takeshi Udagawa

Two-Particle Correlations in Ultra Relativistic Heavy Ion Collisions

by

Michael Scott Daugherity, B.S.; B.S.

Dissertation

Presented to the Faculty of the Graduate School of

The University of Texas at Austin

in Partial Fulfillment

of the Requirements

for the Degree of

Doctor of Philosophy

The University of Texas at Austin

August 2008

To Beth and Molly

Acknowledgments

There are many, many people who have contributed to make this work possible. First, I would like to thank my wife Beth and daughter Molly, but I'm at a loss for words to express my gratitude for the years of love, support, and understanding. Every single day I see the glint of Heaven in your eyes. Thank you both for the joy in my life.

I thank my parents and in-laws for their constant support, and believing in me even when I couldn't believe in myself. I thank my friends for the perspective and balance in my life. The communities at University Avenue and Immanuel Austin churches have been our extended family providing tireless support throughout the years.

The two people who have invested the most in my research are Lanny Ray and Tom Trainor. Thank you for your patience and wisdom; and thank you for teaching me what it means to be a scientist. Thanks to Jerry Hoffmann, Christina Markert, and Rene Bellwied for all of the opportunities. Thanks to my fellow graduate students and the postdoc at UT for making work fun and interesting, but mostly for asking hard questions which are the most helpful of all. Thanks to the STAR Collaboration and BNL for providing a great place to learn; I could write pages and pages expressing my gratitude to the many people who have helped. I must especially thank the Event Structure working group for all of the opportunities. It has truly been a privilege to work with you.

Finally, thanks to Lanny, Liz, and Dylan for editing this dissertation. They have offered numerous improvements while saving me from countless embarrassing errors. Any remaining mistakes are my own.

Michael Scott Daugherity

The University of Texas at Austin
August 2008

Two-Particle Correlations in Ultra Relativistic Heavy Ion Collisions

Publication No. ____________________

Michael Scott Daugherity, Ph.D.
The University of Texas at Austin, 2008

Supervisor: Gerald Hoffmann

The Relativistic Heavy Ion Collider (RHIC) accelerates gold nuclei to nearly the speed of light and smashes them together, forming the most extreme conditions of high energy and density ever produced in a laboratory. The first detailed study of the energy and centrality (collision overlap) dependence of two-particle autocorrelations is presented for charged hadrons produced in $\sqrt{s_{NN}} = 62$ and 200 GeV Au+Au collisions and measured by the STAR detector at RHIC. This analysis is unique in using a large momentum acceptance of $p_t > 0.15$ GeV/c, $|\eta| \leq 1.0$, and full 2π azimuth to form all possible two-particle pairs to measure minimum-bias correlations. Proton-proton collisions at 200 GeV are studied as a reference, where correlation structure in these collisions is dominated by a peak centered at zero relative opening angles on η and ϕ due to minimum-bias jets (minijets) from semi-hard parton scattering. Correlations in heavy ion collisions show significant deviations from this reference revealing new interactions. A sudden and dramatic increase of the minijet peak amplitude and η width is observed relative to binary-collision scaling which occurs at an energy-dependent centrality point. These results confirm a rapid transition of minijet correlation properties suggested in previous studies at 130 GeV. There is a possible scaling of the transition point with transverse particle density. This transition leads to a large excess of minijet correlations in more-central Au-Au collisions relative to binary-collision scaling. Additional studies of charge-dependence and transverse correlations reveal important distinctions between correlations from the originating minijets and the additional correlations emerging above the transition point. When considered with similar systematic trends from studies of transverse momentum in single-particle spectra and two-particle correlations, these results appear to be strongly inconsistent with often made assumptions of rapid thermalization in RHIC heavy ion collisions.

Contents

List of Tables

List of Figures

Chapter 1

Introduction

1.1 Terminology

Relativistic heavy ion physics, while encompassing many aspects of particle, nuclear, and high-energy physics, has developed a terminology unique to the field. The terms and concepts discussed in this chapter provide a general introduction to this area of research, while specialized topics will be covered in later chapters.

1.1.1 Observables

The basic experimental goal is to collide two particles or nuclei together at high energies. A single collision is called an *event*, and while the first publications from the STAR Collaboration examined a few hundred thousand events, current analyses often use tens of millions of events. Each experiment at the Relativistic Heavy Ion Collider (RHIC) consists of a group of complementary detectors centered around a beam crossing point where events occur. The collider facility is designed to provide a high rate of events to each experiment, though determining when an event has occurred and which events are suitable for physics analysis are the first of many experimental challenges to come.

When colliding gold ions at top energy, a single event may produce on the order of several thousand particles. The number of produced particles is the event's *multiplicity*. The individual detectors within an experiment are each optimized to examine properties such as momentum or energy of one or more particle types. For example, a time projection chamber records momentum of charged particles but is insensitive to neutral particles, while a calorimeter measures energy but has a low chance of detecting certain particles. Experiments are prohibited from placing detectors inside the beam line so each detector is limited to a finite volume, though cost and overall balance of detectors are large considerations. Each detector has a certain *acceptance*, area covered by the detector, and *efficiency* in detecting the particles that pass through. In other words, the probability that a particle will reach a detector is related to acceptance, and the probability of that particle actually being detected is the efficiency. The information recorded for all detected particles is used in physics analysis.

1.1.2 Kinematics

The precise location of an event is referred to as the event *vertex*. Particles travel from the vertex outwards to the detectors which can measure the components of the particle's momentum. The most convenient coordinate system is often a combination of cylindrical and spherical coordinates. Consider an event centered at the origin of a Cartesian coordinate system. The direction of the collider's beam defines the z-axis. To exploit any potential symmetries around the beam line we resolve the momentum vector p into *longitudinal* component along the beam axis and a *transverse* component perpendicular to the beam. The $x - y$ plane is represented in cylindrical coordinates as a vector with magnitude p_t, for transverse momentum (also written as p_T or $p_\perp$) with $p_t^2 = p_x^2 + p_y^2$, and azimuthal angle ϕ (used as shorthand for p_ϕ).

To be consistent with cylindrical coordinates we could consider p_z, the longitudinal momentum along the beam axis, as the final component. However, in particle and nuclear physics a quantity called *rapidity* is often used to make relativistic transformations more convenient. Rapidity may be defined in several ways, the most common are (see *e.g.* the *Kinematics* chapter of the Particle Data Book [1]):

$$\begin{aligned} y &= \ln\left(\frac{E+p_z}{m_t}\right) &\quad (1.1)\\ &= \frac{1}{2}\ln\left(\frac{E+p_z}{E-p_z}\right) &\quad (1.2)\end{aligned}$$

for total energy E and transverse mass $m_t = m^2 + p_t^2$ for a particle of mass m. It must be noted that rapidity is a longitudinal measure, though transverse rapidity $y_t = \frac{1}{2}\ln\left(\frac{E+p_t}{E-p_t}\right)$ will be considered later.

Calculating rapidity requires measuring the particle's total energy (or momentum and mass). When this information is not available the *pseudorapidity* is used, which is defined as rapidity in the high energy limit of $E \gg m$ as

$$\eta = -\ln\left[\tan\left(\frac{\theta}{2}\right)\right] \quad (1.3)$$

for polar angle θ where $p_z = p\cos\theta$. At angles perpendicular to the beam $\theta = \pi/2$ and $\eta = 0$, while $\eta = \pm\infty$ along the beam. Thus, the transverse momentum components are similar to cylindrical coordinates, while longitudinal momentum when using pseudorapidity is related to the polar angle found in spherical coordinates.

1.1.3 Centrality

The total center-of-mass energy E_{cm} is the energy available to produce new particles during a collision. At RHIC this energy is conventionally expressed as $\sqrt{s} = E_{cm}$. For symmetric collisions, where the same particle is used in both beams such as p+p or Au+Au, the center-of-mass energy per nucleon is $\sqrt{s_{NN}} = \sqrt{s}/A$ for beam ions with atomic number A. Therefore, there are two ways to adjust the total energy of an event: set $\sqrt{s_{NN}}$ in the collider energies, or change the number of nucleons "participating" in the collision.

Consider a beam ion as a sphere with radius R. The minimum distance between the centers of two colliding ions is the *impact parameter*, denoted as b. Events will span the entire continuum from $b = 0$ head on collisions to glancing $b = 2R$ collisions. The degree of overlap defines the *centrality* of a collision, from most central at $b = 0$ to least central, or *peripheral*, collisions at $b = 2R$. The experiments at RHIC have widely varying detector acceptances, and consequently they would observe a huge range of multiplicity in measuring the same event. Centrality enables inter-experiment comparisons by ensuring that all parties are looking at the same types of events.

Impact parameter is one of many centrality measures. The most common method is to assume that on average multiplicity increases monotonically with centrality. Then by measuring the distribution of multiplicities over many events, it is possible to assign centrality fractions to multiplicities. For example, within a certain detector if 10% of events have multiplicities of 500 or greater, and 20% have 450 or greater, then events with between 450 and 500 particles are in the 10-20% centrality range, and events with more than 500 are in the 0-10% range. Somewhat counter-intuitively, when dealing with centrality fractions 0% refers to the most central while 100% corresponds to most peripheral.

Centrality fractions is also the least model-dependent way to estimate centrality, though care must be taken to correct for undetected particles and events to ensure that the measured fractions match the true centrality. Nonetheless, event multiplicities are the only quantity which are directly observable in an experiment. Other centrality measures such as impact parameter,the number of participating nucleons in the collision N_{part}, or the total number individual nucleon-nucleon interactions N_{bin} (also written as N_{coll}) are often estimated using a computer simulation known as a Monte Carlo Glauber model [2]. First, nucleons are randomly positioned inside two nuclei based on parameterizations of nuclear density profiles. Next, an impact parameter is randomly chosen and the two nuclei are overlapped. If any two nucleons lie within a minimum distance based on the inelastic scattering cross section then they interact. This procedure gives distributions of other centrality measures which may be related to centrality fractions. These measures are used to search for scaling trends in different collision systems, for example testing if production of a certain kind of particle scales as N_{part} or total multiplicity.

1.2 Overview

The scope of this dissertation covers a correlation analysis on data from the STAR detector at RHIC. The aim of this work is to document the analysis procedure, results, and discuss physical interpretations of these measurements. This section discusses the organization of chapters in this dissertation.

Progress in relativistic heavy ion physics is irrevocably linked to the ability to build ever larger and more powerful accelerators. Chapter 2 begins with a brief history of early accelerators, followed by a summary of the immense effort and development required to build RHIC. Next, the path of the beam is traced through the entire complex as it is accelerated to 99.995% the speed of light. The RHIC accelerator is only half of the story. The next step is measure the collisions and extract physics information. Chapter 2 continues with an overview of the STAR detector, and the steps required to detect an event, track the outgoing particles, and analyze the collected information.

Chapter 3 provides a motivation for this research by tracing the evolution of a powerful physics analysis method. Previous studies and theoretical expectations suggested that fluctuations in certain properties of the collision event may reveal critical phenomena indicative of a phase transition, or even a certain class of unusual events. Non-statistical fluctuations were indeed observed for the first time at RHIC, but neither critical phenomena or special events were found. Fluctuations may be caused by significant correlations among the particles, and it was later realized that correlations provided much more detailed and differential information which is more easily related to physical processes than fluctuation measures. Most of chapter 3 is devoted to surveying the previous studies on particle correlations while examining open questions to be addressed by this research. The analysis method developed here is not designed to make a single, specific measurement, instead it outlines an entire research program unfolding at RHIC.

Following this conceptual overview of physics analyses, chapter 4 gives the detailed mathematical formalism of this correlation analysis. Only in recent years has this analysis been directly related as a heavy ion physics application of other statistical tools such as Pearson's correlation coefficient and the autocorrelation originally developed to study Brownian motion. Finally, chapter 4 studies the relationship between correlations and previously studied fluctuations.

Chapter 5 lists the remaining details necessary to the analysis. First, criteria for event selection is studied along with the method of centrality determination. Then particles are chosen from these events based on kinematics, track reconstruction quality, and particle identification. These particles are formed into pairs for the correlation analysis, though certain two-track reconstruction inefficiencies may be corrected by careful pair selection.

Based on all of this framework, chapter 6 presents the angular correlation results. The measured correlation structures are decomposed into physically relevant components. The energy and centrality dependence of these components is studied for the first time, yielding some expected behavior as well as some new surprises.

Chapter 7 extends these angular correlations by studying the dependence on relative electric charge. Each of the physical mechanisms which serve as a correlation source has a specific dependence on charge, so this analysis provides valuable clues for the interpretation of results. Correlations which are charge independent are not present, somewhat simplifying the analysis in this chapter. The combined angular correlations begin to point to an interesting picture of RHIC physics.

The final analysis is shown in chapter 8. Whereas the previous chapters studied angular correlations, this analysis examines the complementary transverse correlations. The results in this chapter are not amenable to model function fits, although the individual sources may be at least partially isolated by decomposing the correlations on relative charge sign and azimuth.

The final chapter summarizes the results of this research and discusses the physics interpretations and implications. While these studies present a comprehensive survey of correlations in heavy ion collisions, these results become even more suggestive when placed in the larger context of previous studies. Finally, some avenues for future work are discussed to explore open questions. In many ways, this field is still evolving as we try and make sense of the huge amount of RHIC data now available. Looming over this is the imminent turn on of the LHC which will challenge our understanding thus far. The correlation analysis used in this research is reaching maturity after years of intense development by a group of many people. The proof of principle of this analysis was shown in data from the first RHIC run. The research presented here documents the developments in this method since this initial exploratory attempt and new results over a much larger sample of data. This novel technique offers new insight into many unexplored areas of RHIC physics. In this way, this research represents one small step in a long journey of studying matter in extreme conditions.

Chapter 2

Experimental Facilities

The Relativistic Heavy Ion Collider at Brookhaven National Laboratory provides unique access to matter in an unprecedented regime of energy and density. The STAR detector primarily studies this extreme state of matter by characterizing as much information as possible from each heavy ion collision. The purpose of this chapter is to explore these experimental facilities.

2.1 Relativistic Heavy Ion Collider

2.1.1 History

Early Accelerators

The history of the design and construction of the Relativistic Heavy Ion Collider is deeply embedded in the larger story of the development of particle accelerators. Upon the establishment of the United States National Laboratory system two laboratories were set to focus on elementary particle physics: Lawrence Berkeley National Laboratory on the West coast, and Brookhaven National Laboratory on the East coast. It soon became clear that each lab had to construct ever larger accelerators to remain competitive for the limited resources available to the national laboratory system. In 1948 these laboratories along with their funding agency, the Atomic Energy Commission (AEC), worked out a gentleman's agreement providing a logical and amicable construction schedule of alternating new facilities between the labs. Thus Brookhaven built the 3 GeV Cosmotron in 1952 followed by the 6 GeV Betatron at Berkeley in 1956, which was followed by the 33 GeV Alternating Gradient Synchrotron (AGS) at Brookhaven in 1960.

The balance was upset in 1965 by an AEC-commissioned site selection committee from the National Academy Sciences. Upon their recommendation the next accelerator was to be built at the facility in Illinois now known as Fermilab. The situation was further complicated by the Stanford Linear Accelerator Center becoming operational in 1966. Brookhaven scientists rallied for the next facility, so lab management appointed a committee headed by Val Fitch, would had recently completed work for which he would receive the Nobel Prize, to propose a new facility. The committee began to study fixed-target accelerators in the 1 to 2 TeV range as the next natural step in the gentleman's agreement. This energy range was required to keep pace with the exponentially increasing trend in accelerator energies, essentially a Moore's Law for particle physics, observed from 1930 to 1960 [3] and shown in figure 2.1.

ISABELLE

Advancements in the early 1970's caused the Fitch committee to move in another direction. The world's first hadron collider, the Intersecting Storage Rings (ISR) at CERN, came on-line in 1971 with a beam energy reaching 31.5 GeV. It was thus decided that the next major American facility should be a 200 GeV proton-proton collider. The proposed machine was named ISABELLE for "Intersecting Storage Accelerator + BELLE for beauty" [4]. The committee's report, finalized in November of 1971, indicated that key aspects of the project were the advantages of

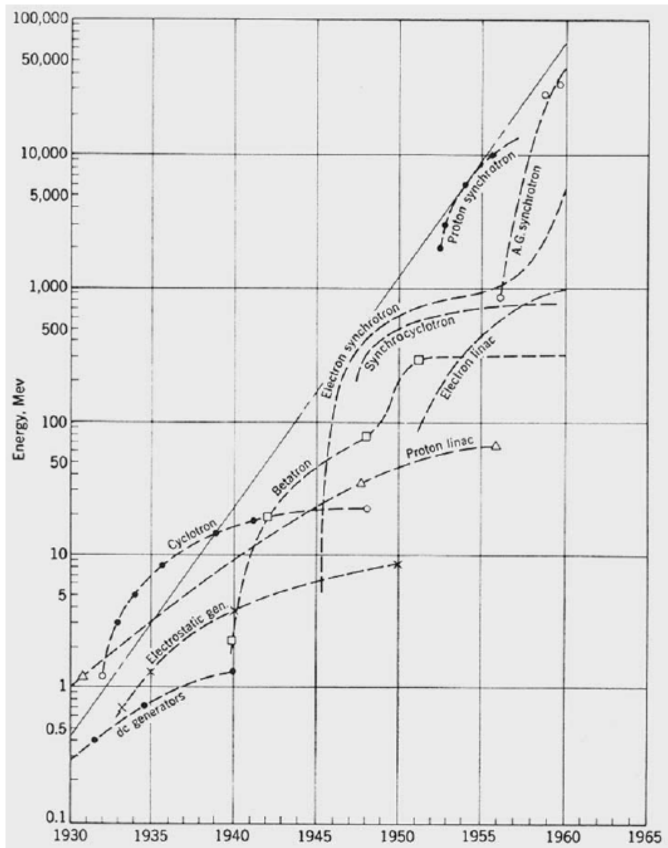

Figure 2.1: The Livingston-Blewett curve showing exponential growth of early accelerator energies [3].

colliders over fixed-target experiments and the need for superconducting magnets to run the ambitious new facility.

Ultimately these superconducting magnets would prove to be the Achilles' Heel of the ISABELLE project [5]. Unprecedented economic conditions in the United States including a 13% inflation rate in 1974 reduced available funding. To make ISABELLE a more competitive project, in 1977 the proposed beam energy was increased from 200 to 400 GeV requiring increases in the circumference of the ring and the magnetic field strength from 40 to 50 kG. Impressed with this new promise, the funding agencies approved the upgraded ISABELLE. Ground was broken on October 27, 1978 and 200 acres of land were cleared of trees. However, prototype after prototype for the magnets was failing to reach the new field requirements, and the entire project began to stall. A final attempt was made to rename the project as the Colliding Beam Accelerator (CBA) and recast it to higher energies. Regardless of the new approach, after spending approximately $200 million the entire project was terminated in 1983 [6] largely to make way for the new Superconducting Supercollider, also doomed to failure.

RHIC

The quark model developed in the 60's was uncomfortably waiting for confirmation, and ideas of using heavy-ion colliders to search for deconfined quarks or abnormal nuclear were being explored, as illustrated in a 1975 review article by T. D. Lee [7]. Berkeley had upgraded the Bevatron by linking it to the SuperHILAC linear accelerator. The new machine, called Bevalac, was exploring nuclei in GeV regime beginning with Oxygen ions in 1975 and including Uranium in 1982. Following on the success of the Bevalac, only weeks after the termination of ISABELLE/CBA in 1983, a Brookhaven-based task force on relativistic heavy ion physics presented recommendations to lab management for the design parameters of a Relativistic Heavy Ion Collier that could be built in the footprint of the previous project [8]. Whereas nothing would be salvaged from the death of the SSC, ISABELLE had left in her wake a tunnel, support structures, a cryogenic system, and perhaps most importantly, hard-won progress on the design of superconducting magnets. Key aspects of RHIC included the ability to accelerate a full range of beam species from nuclei to heavy ions, and to do so asymmetrically to allow for proton-nucleus collisions.

During that same summer of 1983 a crucial milestone was reached when the ten-year Long Range Plan for Nuclear Physics committee identified RHIC as the "highest priority new scientific opportunity within the purview of our science [9]." For the remainder of the decade, intense efforts finalized the design concept for RHIC including the target energy and luminosity as well as a spin program made possible by contributions from RIKEN. As the planning was taking place, two consecutive construction projects at the AGS allowed for the acceleration of gold ions to relativistic energies. In 1988, the Department of Energy requested a RHIC Project Start in 1990, which was declined by the Office of Management and Budget. After years of planning and design, the construction of RHIC began in 1991 with a total line-item budget of $616.6M including funding for the collider, detectors, accelerator research and development, and operations.

Much unlike its predecessor, the construction of RHIC remained largely on schedule. The first magnet sextent was tested in 1997, magnet production was completed in 1998, and the rings were assembled in 1999. The first engineering run of the collider took place from June to September of that year. Operations for physics data in 2000 began with cool-down to an operating temperature of 4.6 K on March 10. First collisions occurred on June 12 at 56 GeV total energy and target luminosity (10% of design goals) was reached for 130 GeV on June 12 [10].

2.1.2 Design

Accelerator Design

While some of RHIC's design was constrained by the existing ISABELLE facilities, a large number of complex factors had to be considered for the final plan. The proposed physics program calls for the unique feature of colliding beams of different ion species at the same energy per nucleon. In the most extreme case of colliding protons with gold ions the beam rigidities differ by a factor of 2.5, requiring a machine design based on separate rings that can operate with different magnetic fields.

These magnets must attain high fields for extended periods of time to produce sufficient beam energies within the fixed accelerator circumference. The necessary parameters required the use of superconducting magnets which minimize power consumption while allowing higher field strength than conventional magnets. However, superconducting magnets also require a extensive cryogenic systems to reach the operating temperature of 4 K. A cost optimization of magnet design suggested that filling the ring with relatively low field magnets was the most economical approach. With this layout, achieving 100 GeV per nucleon beams of gold ions and 250 GeV proton beams requires a 3.458 T field [11]. It is notable that this is less than the 5 T magnets required for ISABELLE which proved so problematic over the project lifetime.

Beyond the dipole magnets used for bending the beam around the collider circumference, a vast array of magnets are required for focusing. The intrabeam scattering caused from mutual Coulomb repulsion among beam particles is proportional to Z^4/A^2 [12], thus the heavy ions constrain this aspect of the accelerator design. To minimize the effect of this expansion of the beam, the RHIC arc sections have stronger focusing using short dipole and quadrupole half-cells than typical proton accelerators.

The spin program poses another large challenge of designing the highest energy polarized proton facility in the world by far. Maintaining beam polarization during acceleration is complicated by the increasing spin vector precession frequency, which grows with the Lorentz factor γ. As this rate increases, so do the number and strength of depolarizing resonances, which limit the effective length of time that a polarized beam may be stored [12]. Thus maintaining beam polarization becomes more difficult with higher energy, providing more obstacles for the RHIC spin program to overcome.

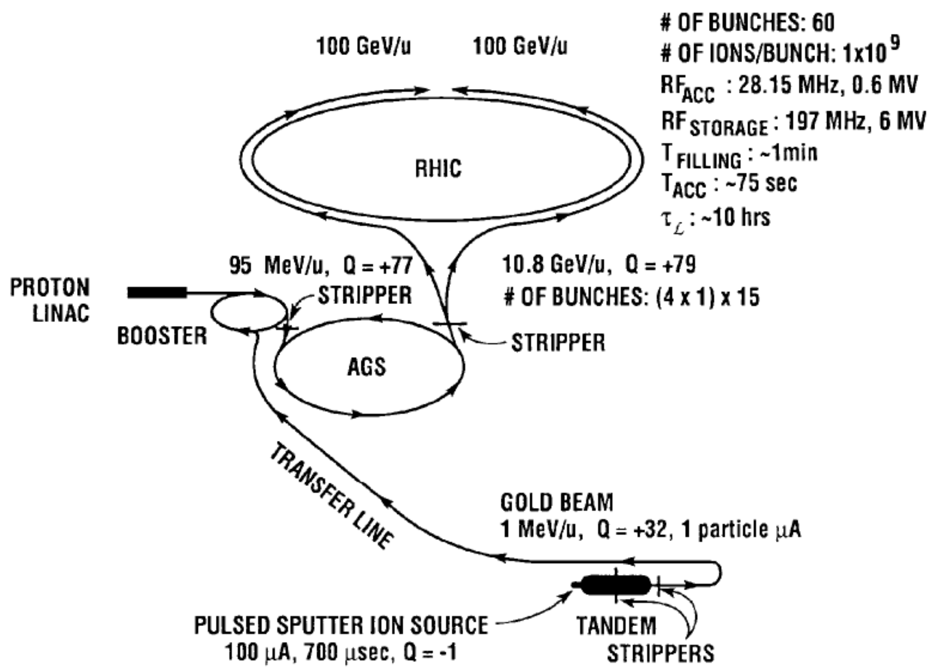

Figure 2.2: The layout of the RHIC accelerator complex.

Facility Layout

The complete RHIC facility contains a complex set of accelerators interconnected by transfer lines. Figure 2.2 traces the path of the beam from the ion source to the booster, the AGS, and finally the RHIC rings where the final energy is reached [11].

The journey begins with a negative ion source at ground potential. The ions, produced with charge Q = -1, are accelerated from ground to +15 MeV using the first in a pair of tandem Van de Graaf accelerators. Electrons are removed by passing the beam through a stripping foil, leaving positively charged ions which are then accelerated back to ground potential with the second accelerator. For gold, the only case that will be detailed here, the ions are partially stripped to a Q = +12 charge state and leave the Tandem accelerators with a kinetic energy of 1 MeV per nucleon. Upon exiting, the ions are further stripped to Q = +32 and sent along a 550 m transfer line to the Booster synchrotron traveling at less than 5% the speed of light.

In less than 100 ms the Booster accelerates this beam to 0.65 T. A two cavity RF system provides accelerating potential and bunches the beam by operating on the eighth harmonic of the revolution frequency, producing one bunch per harmonic and ultimately reaching 5 MHz with a kinetic energy of 95 MeV per nucleon. At extraction the eight bunches are merged into four, and the ions are stripped once again to Q = +77 and sent to the AGS at around 37% the speed of light.

The Alternating Gradient Synchrotron, or AGS, is filled by four of these Tandem-Booster cycles which occur at a rate of 5 Hz. The sixteen bunches in the AGS are accelerated and eventually merged into a single bunch with energy of 10.8 GeV per nucleon. These bunches, which by now are reaching 99.7% the speed of light, are stripped of their two final electrons and sent to RHIC.

Each RHIC ring is nominally filled with 60 bunches from the AGS. Each bunch consists of roughly 10^9 ions, which contributes to the large intrabeam scattering. Filling both rings must take place as quickly as possible to minimize this effect, and is accomplished in about one minute. Maintaining and accelerating the beams which sit only 90 cm apart around the 3.8 km circumference requires a large array of magnets. The main components are the insertion system, including 108 dipoles with 216 quadrupoles, and the arc system consisting of 288 dipoles and 276 quadrupoles. Additional smaller magnets include 72 trim quadrupoles, 288 sextupoles and 492 corrector magnets. A more detailed layout of the RHIC beams is shows in figure 2.3. The superconducting magnets are cooled below 4.6 K by circulating supercritical helium supplied by ISABELLE's 24.8 kW refrigerator. All of these components drive the beam to reach 99.995% the speed of light.

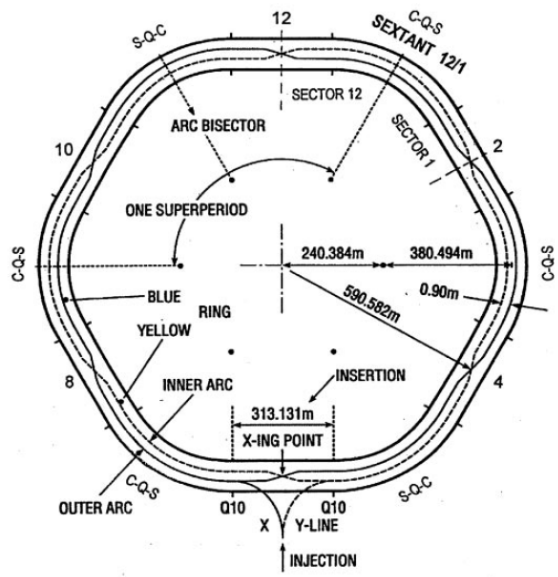

Figure 2.3: A more detailed diagram of the beamlines at RHIC.

2.1.3 Performance

The RHIC accelerator has already achieved and surpassed its specifications. The 200 GeV center of mass energy goal was met with gold ions in Run 2. The luminosity goal has been surpassed by a factor of two for heavy ions and a factor of five for polarized protons [9]. A summary of RHIC runs is given in table 2.1 from [13], and RHIC's luminosity development in comparison to other hadron colliders in shown in figure 2.4.

The first glimpse of new physics available in the inceptive RHIC run proved to be impressive. Multiplicity in central collisions, first published by PHOBOS [14], show a logarithmic increase in produced particle density with collision energy so that the multiplicity density per nucleon pair significantly exceeds that from nucleon-nucleon colliders. The energy density obtained by PHENIX [15] using the Bjorken formulation reached $\epsilon_{BJ} = 4.6$ GeV$/fm^3$. Such estimates are strongly

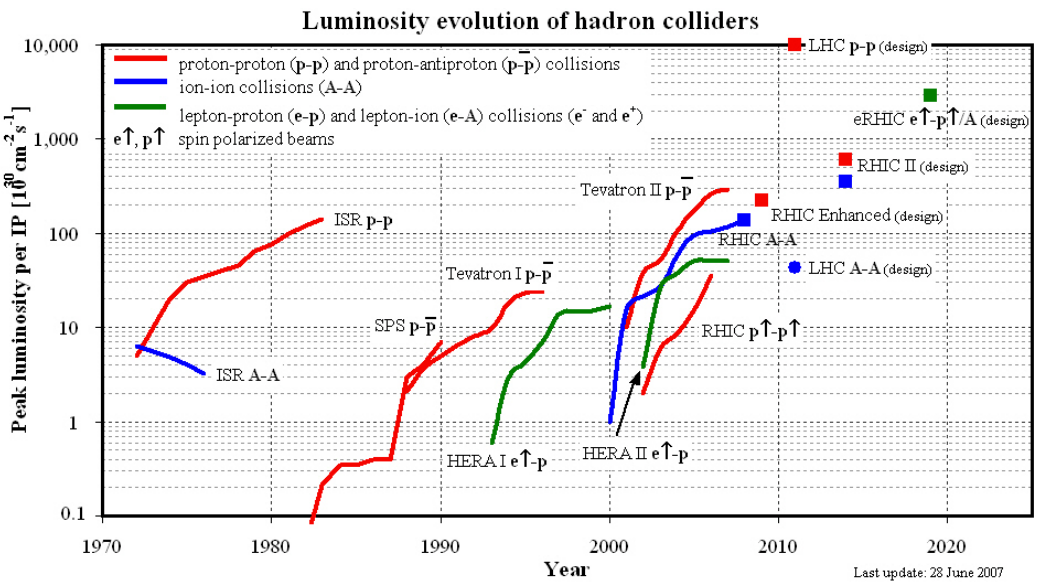

Figure 2.4: The luminosity evolution of hadron colliders.

dependent on the formation time, which is usually taken as 1 fm/c. More aggressive estimates with smaller times lead to ϵ_{BJ} of 15 GeV/fm^3 or larger. This approach gives a model dependent, though not unreasonable, estimate of energy density well above the 1 GeV/fm^3 for normal nuclear matter, and a necessary but not sufficient condition for the creation of QGP.

2.2 The STAR Detector

Each of the RHIC experiments takes a unique approach to characterizing the matter produced in heavy ion collisions. Four of the six beam intersection regions are populated with physics detectors. The largest by weight at 4,000 tons is the PHENIX detector which is a collection of a dozen subsystems each largely specialized to search for specific processes. Conversely, the other large detector, STAR, is designed to track as many particles as possible to obtain more overall information about each event. These are complemented by the two smaller experiments: BRAHMS, which

Table 2.1: Summary of RHIC runs

Run ***(year)***	**Species**	**Energy** *[GeV/nucleon]*	**Time**	**Luminosity**	**Average Polarization**
Run 1 (2000)	$Au^{79} - Au^{79}$	65.2	5.3 weeks	20 μb^{-1}	–
Run 2 (2001-2)	$Au^{79} - Au^{79}$	100.0	15.9 weeks	258 μb^{-1}	–
		9.8	16 hours	0.4 μb^{-1}	–
	pol p – p	100.0	8.3 weeks	1.4 pb^{-1}	14%
Run 3 (2002-3)	$d - Au^{79}$	100.0	10.2 weeks	73 nb^{-1}	–
	pol p – p	100.0	9.0 weeks	5.5 pb^{-1}	34%
Run 4 (2003-4)	$Au^{79} - Au^{79}$	100.0	12.0 weeks	3530 μb^{-1}	–
		31.2	9 days	67 μb^{-1}	–
	pol p – p	100.0	6.1 weeks	7.1 pb^{-1}	46%
Run 5 (2004-5)	$Cu^{29} - Cu^{29}$	100.0	7.8 weeks	42.1 nb^{-1}	–
		31.2	12 days	1.5 nb^{-1}	–
	pol p – p	100.0	9.4 weeks	29.5 pb^{-1}	46%
Run 6 (2006)	$d - Au^{79}$	100.0	13.1 weeks	93.3 pb^{-1}	58%
	pol p – p	31.2	12 days	1.05 pb^{-1}	50%
Run 7 (2006-7)	$Au^{79} - Au^{79}$	100.0	12.8 weeks	7250 μb^{-1}	–
Run 8 (2007-8)	$d - Au^{79}$	100.0	9.0 weeks	437 nb^{-1}	–
	pol p – p	100.0	3.4 weeks	38.4 pb^{-1}	45%

very precisely measures a very small subset of produced particles, and PHOBOS, which detects the largest fraction of particles but records the least information about them. While areas of overlap does exist among the four experiments, each is specialized to examine a certain aspect of RHIC physics.

Only the STAR detector, specifically the components most relevant to this research, will be considered further. The authoritative reference for detailed information about all four RHIC experiments can be found in a special issue of *Nuclear Instruments and Methods in Physics Research A*, volume 499, issues 2-3 (2003).

2.2.1 Overview

STAR, the Solenoidal Tracker At RHIC, was primarily designed for measurements of hadron production over a large solid angle. As the name suggests, the central

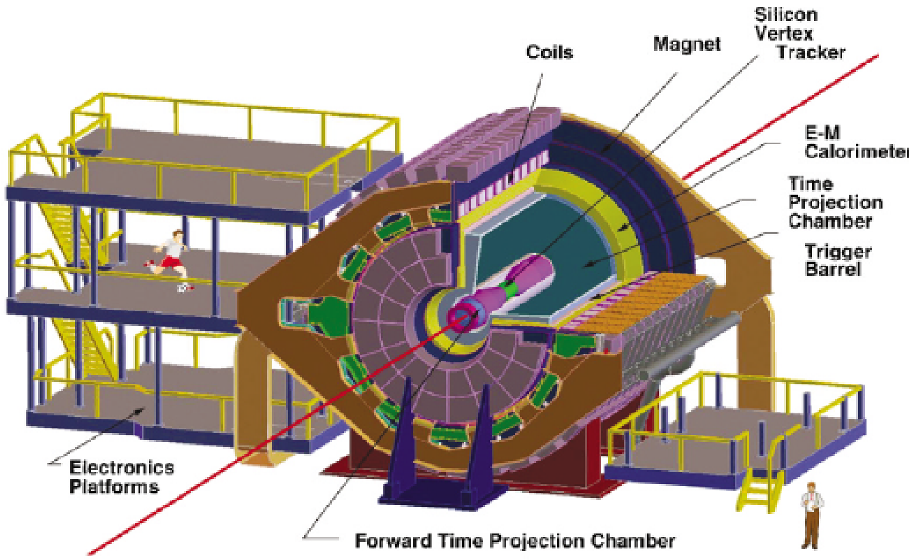

Figure 2.5: Perspective view of the STAR detector.

feature of STAR is a large cylindrical detector, the Time Projection Chamber (TPC), capable of simultaneously tracking thousands of particles. A diagram of STAR is given in figure 2.5. The large acceptance of charged particles makes STAR ideally suited for event-by-event measurements as well as detecting hadron jets at mid-rapidity. Figure 2.6 illustrates the subsystems which contribute to the precision tracking, momentum and energy resolution, and particle identification [16]. The TPC, forward TPC (FTPC), and Silicon Vertex Tracker (SVT) in conjunction with a powerful magnet provide tracking and momentum analysis of charged particles. The particle identification capabilities are extended with the time of flight (ToF) and Ring Imaging Cherenkov (RICH) detectors . The Electro-Magnetic Calorimeter (EMC) allows for detection of neutral particles. Also shown are the Central Trigger Barrel (CTB) and the Zero Degree Calorimeter (ZDC), the two primary triggering systems.

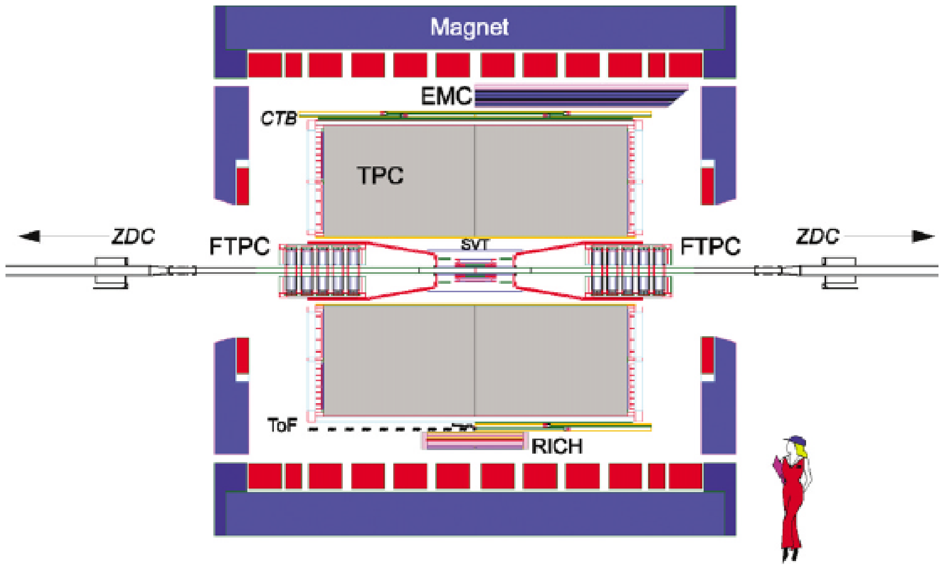

Figure 2.6: Side view of the STAR detector as configured in 2001.

2.2.2 Trigger and Data Acquisition Systems

The entire STAR detector is capable of reading events at 100 Hz. With high luminosity RHIC beams, an interaction is likely to occur in each bunch crossing at a rate of nearly 10 MHz. Therefore the goal of the triggering system is to reduce this rate by five orders of magnitude while ensuring the quality of each event, as well as providing subsets of events with special properties tailored to match physics goals [17].

Fast Detectors

Information is provided to the trigger system in stages. Initial triggering decisions are based on the fast detectors which operate at the RHIC bunch crossing rate (every 107 ns). More decisions are made as information from the other detectors becomes successively available. The fast detectors are a Zero Degree calorimeter

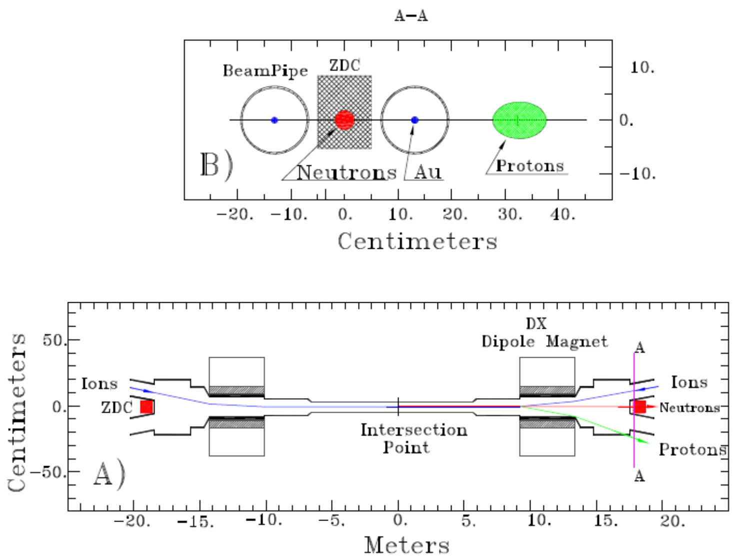

Figure 2.7: Top panel: View along beam axis of ZDC position. Bottom: Overhead view.

(ZDC) outside of the dipole magnets and the Central Trigger Barrel surrounding the TPC.

The ZDC is designed to detect evaporation neutrons produced along the beam axis as heavy ions break apart. By placing the ZDC outside of the dipole magnets, charged particles such as beam ions, protons, and other charged fragments are swept away before reaching the ZDC [18], see figure 2.7. The ZDC consists of tungsten absorber plates with fiber optical connections to a PMT. Identical ZDCs are in place at each RHIC experiment for use as a beam luminosity monitor as well as an event trigger.

The other fast detector is the CTB consisting of 240 slats surrounding the TPC to measure charged particle multiplicity in $|\eta| \leq 1$ and 2π in azimuth. Coincidence of neutrons detected in the ZDC with a minimum threshold met in the CTB provides the basis for a minimum-bias trigger for heavy ion collisions. CTB

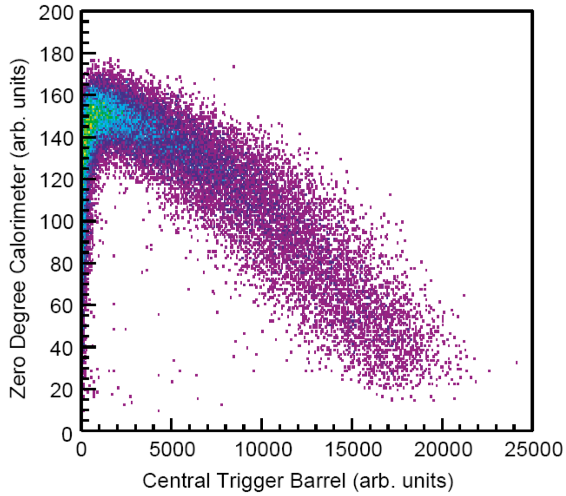

Figure 2.8: Summed pulse heights in the ZDC and CTB for reconstructed events.

signals increase monotonically with centrality, while ZDC signals depend on the collision geometry as both peripheral and central collisions supply few evaporation neutrons. This relationship between CTB and ZDC signals, figure 2.8, gives a distinct boomerang shape.

Trigger Levels

The fast detectors provide the initial input into the multi-tiered trigger system. The Level 0 trigger processes fast detector information and issues the event trigger. Immediately afterwards there is a period of several milliseconds required for the selected detectors to read out and digitize data. This lag allows time for more detailed analysis of the trigger data with more finely-grained criteria. The Level 1 trigger is given 100 μs while Level 2 gets 5 ms to abort the current event. Otherwise the event proceeds to Level 3.

The third level trigger performs complete online reconstruction of the event using a dedicated farm of computers [19]. Events can be processed at 50 Hz including a simple analysis of basic physics observables. This information is used to make the final decision about an event before it is written to tape.

Data Acquisition

The TPC, along with FTPC and SVT, produces 80 MB of data per event and can read events at 100 Hz. The central task of the data acquisition (DAQ) system is to read this 8,000 MB of data per second, reduce it 30 MB/s, and store the data to tape in the HPSS facility [20].

The large input data rate demands multiple parallel processing at the DAQ front end. This is accomplished by 144 receiver boards for the TPC, 20 for the FTPCs, and 24 for the SVT. The receiver boards and grouped into VME crates which are controlled by a Detector Broker CPU.

The Level 3 trigger must find on the order of 1500 tracks for central collisions and make decisions based on those tracks within 200 ms, which limits the time available for DAQ. The delay between receiving the event and the trigger decision makes it necessary for the DAQ system to manage multiple events simultaneously. Both considerations are met by a dedicated farm of around fifty CPUs integrated within DAQ and responsible for tracking.

2.2.3 The STAR TPC

Overview

STAR boasts the world's largest Time Projection Chamber currently in operation, though that distinction will soon go to ALICE at the LHC. STAR's TPC is a 4.2 m long cylinder and covers a radial distance from 50 to 200 cm from the beam axis, see figure 2.9. As primary particles pass through the TPC, they ionize a gas releasing secondary electrons. These electrons drift along a uniform electric field to the readout end caps. The location of the hits on the end cap provides the x and y

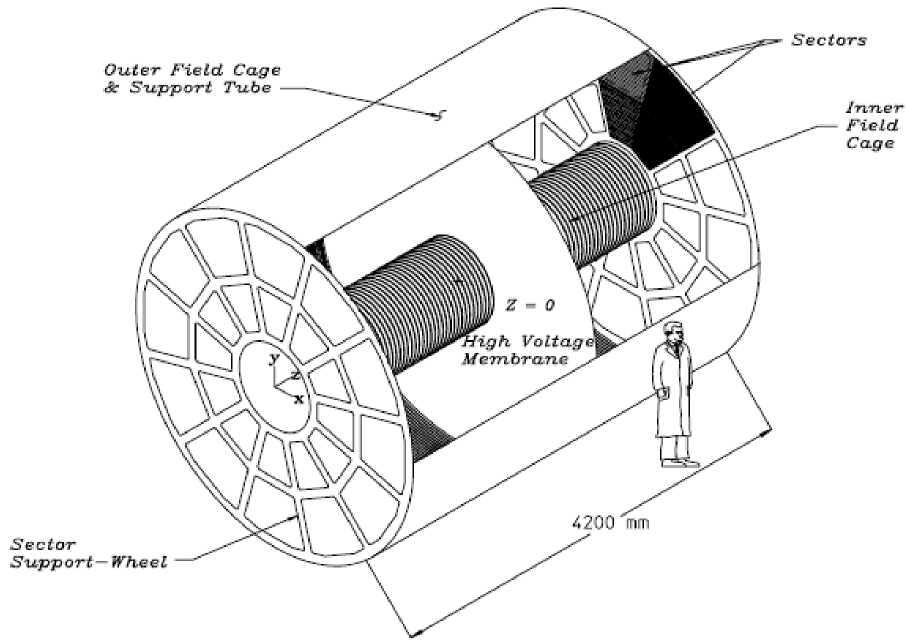

Figure 2.9: A diagram of the Time Projection Chamber.

components of a position on the track of the primary particle, and the electron drift can be used to determine the z component. In this way, each of the 1500 particles produced in a central collision can be tracked simultaneously. A magnetic field parallel to the beam axis creates a momentum-dependent curvature in the primary tracks while leaving the secondary electrons unaffected.

Design

Details of the STAR TPC are documented in [21]. A uniform electric field of 135 V/cm is defined by the central membrane operated at 28 kV and the end caps at ground. The field cage cylinders provide a series of equipotential rings using 183 2 MOhm resistors to ensure a uniform gradient in the electric field.

The construction material for the TPC was chosen to limit the potential for

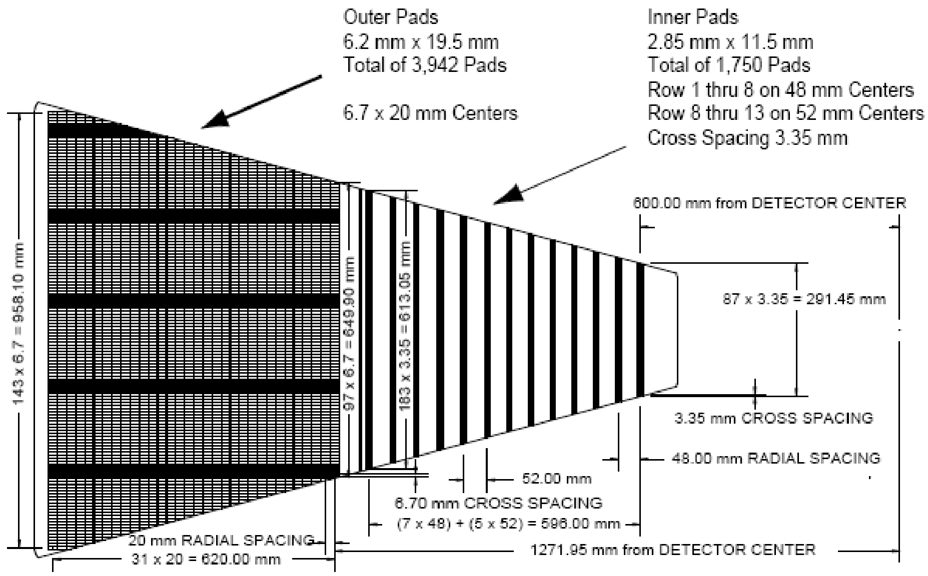

Figure 2.10: Pad layout and dimensions for a single sector of the TPC.

multiple scattering at the inner radius to ensure accurate tracking and momentum resolution. Aluminum was chosen for the inner field cage, using only 0.5% of a radiation length. The outer field cage was constructed with copper to simplify construction and electrical connections. Even though it is significantly thicker than the inner cage, the outer cage is 1.3 % of one radiation length, not much more than the detector gas itself.

The end-cap readout planes are based on Multi-Wire Proportional Chambers (MWPC) with readout pads. The drifting electrons induce an avalanche while approaching the very thin (20 μm) anode wires, providing an amplification of 1000-3000. The positive ions created in the avalanche induce an image charge on the readout pads which is measured. There are a total of 136,608 pads arranged as shown in figure 2.10. The image charged is spread over several adjacent pads, thus the original track position can be reconstructed to within a small fraction of a pad width.

The anode field wires are complemented by a ground grid plane at a distance of 2 mm in the inner subsector and 4 mm in the outer. The primary purpose of the ground grid is to terminate the field in the avalanche region and provide additional shielding for the pads. The outermost wire plane is the gating grid, which is located 6 mm from the ground grid. This grid acts a shutter to control the entry of electrons from the TPC drift volume to the anode planes. The opposite effect of preventing positive ions created by the MWPC from entering the TPC is also desirable. The gating grid is designed to be transparent to the drift electrons while events are being recorded and blocking them the rest of the time.

The TPC is filled with P10 gas, a mixture of 90% argon with 10% methane. This gas has commonly been used in TPCs for the advantageous properties such as a fast drift velocity which peaks at a low electric field. By operating at the velocity peak the drift velocities are insensitive to small changes in temperature and pressure. To maintain purity the gas is held at 2 mbar above atmospheric pressure. Electron absorption is limited by keeping water at less than 10 parts per million and oxygen at less than 100 parts per million.

The TPC is surrounded by a magnet consisting of 30 flux return bars, four end rings, and two poletips [22]. These elements combined weigh roughly 1100 tons and rest on an additional 272 tons of supporting structure. The magnetic field is created by ten main coils with a 5.3 m inner diameter along with two space trim and two poletrip trim coils to maintain field uniformity. At the maximum field strength of 0.5 T these coils carry 4500 A of current and consume 3.5 MW of power.

Particle Tracking

The MWPCs are sensitive to nearly all of the drift electrons reaching the end cap, though the overall tracking efficiency is lower by a number of factors. The acceptance of high momentum particles perpendicular to the beam axis is 96% due to tracks lost

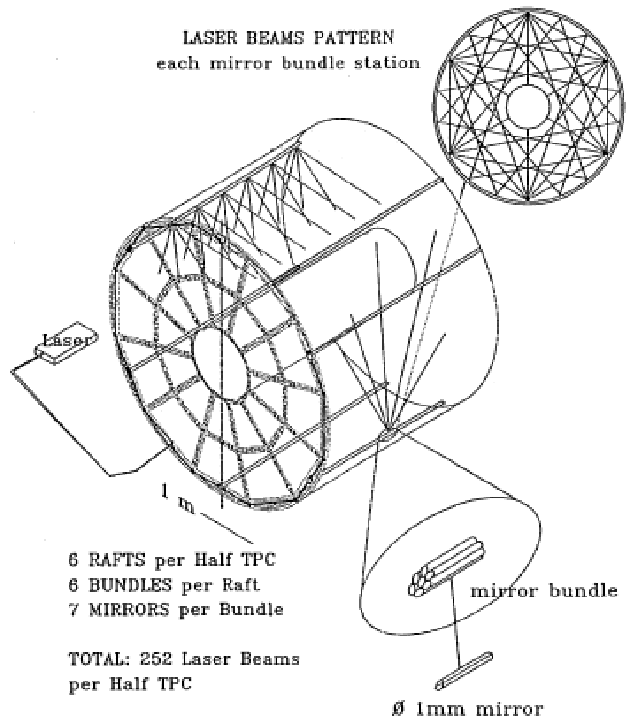

Figure 2.11: Configuration of the TPC laser system.

in the sector boundaries. A fiducial volume cut to exclude hits on the outermost pads reduces the total acceptance to 94%. Accounting for track merging and hardware failures such as bad pads and dead channels lowers the acceptance to 80-90% [21].

To ensure accurate tracking, the drift velocity of electrons must be known to within 0.1% to convert measured time to position. The drift velocity is calibrated using narrow ultraviolet laser beams which imitate charged particle tracks. Using a novel design of splitting a large diameter laser beam with many small mirrors made from glass rods cut at 45 degrees, a total of 252 laser beams are produced to sample each half of the TPC [23]. The configuration is shown in figure 2.11.

After all calibrations and distortion corrections have been applied, the relative error between a point and the track model fit is 50 μm, while the absolute error

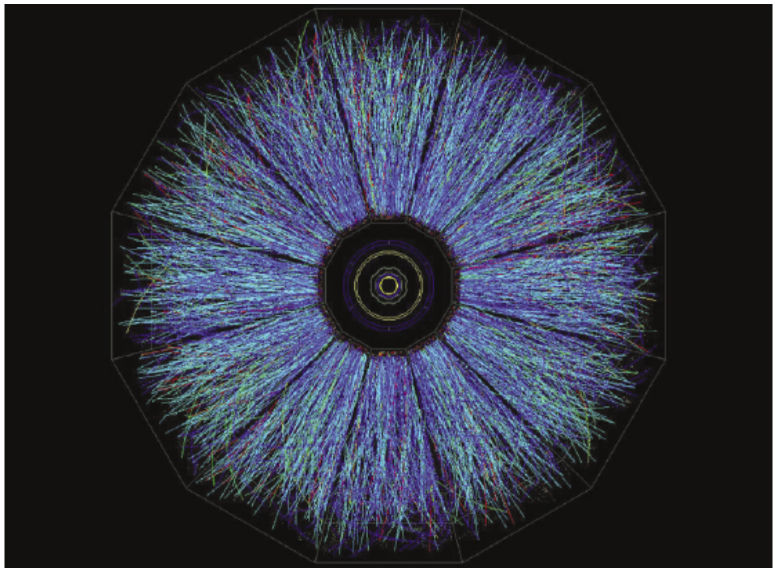

Figure 2.12: Reconstructed tracks in the TPC.

is 500 μm for any single point. Minimizing this error is important for measuring track curvature and thus particle momentum. The primary vertex can also be used to improve momentum resolution as well as to isolate secondary vertices. The primary vertex can be estimated using a global average of all event tracks to within 0.3 mm for central collisions [21]. The transverse momentum is then determined by projecting the track onto the (x,y) plane and fitting a circle through the vertex and hit points. A reconstructed event is shown in figure 2.12.

2.3 Conclusion

The Relativistic Heavy Ion Collider is currently the world's premier facility for heavy ion physics. Even after the Large Hadron Collider begins operation, physics there will be intensely focused on proton-proton collisions for Higgs discovery leaving very little room for a heavy ion program. RHIC's era of dominance has not yet ended, and in many ways the physics impact is just beginning as the emphasis shifts from qualitative statements to quantifying the properties of these collisions. It worthwhile to note the preamble to the RHIC Conceptual Design Report of 1989 [9]:

> The essential motivation for colliding nuclei at ultra-relativistic energies is the production of matter at extreme conditions of temperature and density: extended volumes of hadronic matter with energy densities greater than 10 times that of the nuclear ground state should be realizable, at temperatures which equal or exceed the so-called "limiting temperature" (Hagedorn temperature) at which mesons are emitted in high energy hadron collisions. There is little direct knowledge about what to expect under such conditions. They have not been detected anywhere in the natural universe, and are just beginning to be approached through experiments with ion beams in experiments at Brookhaven and CERN. Thus the proposed facility represents a venture into an almost completely unknown regime for the study of basic properties of matter.

RHIC's venture into the unknown is far from over. Many new surprises may still yet lurk around the next corner, and the potential for new discovery remains as high today as ever.

Chapter 3

Motivation

On February 10, 2000, just at the beginning of RHIC operations, a CERN press release stated that combined data from all experiments in the SPS the heavy ion program presented “compelling evidence for the existence of a new state of matter” [24]. A large number of expected signatures of QGP had been devised and were awaiting confirmation at higher energies than attained at SPS. Therefore analysis of RHIC data began with these experimental and theoretical agendas. However, it became apparent after the first few years that RHIC offered no “smoking gun” proof of quark deconfinement [25].

A recent review [26] emphasizes that “it was not unreasonable to expect a few surprises” at RHIC. The search for QGP may reveal new backgrounds or properties in *ordinary* collisions, thus expected signals of QGP might be found through processes unrelated to deconfinement. Even if a phase transition is observed the new state of matter may have unexpected properties. Also, no comprehensive theoretical model exists to address all of the complexities of heavy ion physics, instead a patchwork of different treatments is applied to various aspects of the collisions each with its own assumptions, adjusted parameters, and uncertainties [25]. This state of affairs has lead to advancements driven primarily by experiment rather than theory. Thus as our understanding of RHIC physics evolves, so do our experimental methods.

This chapter traces one such evolution through its development from a failed smoking gun signal to a powerful new tool allowing novel insight into particle and heavy ion physics. The story will be told in roughly chronological order, though doing much violence to history as many of these concepts and results were developing simultaneously. Finally, this survey of previous work motivates the analysis detailed in the following chapters.

3.1 Fluctuations and Correlations

3.1.1 Fluctuation Measures

One of the expected signatures of a QGP phase transition is the development of critical fluctuations [27]. A system evolving near the boundary of a phase transition should develop significant dynamical fluctuations away from its mean thermodynamic properties. Thus the search for these fluctuations has historically been a central aspect of heavy ion physics research.

One key issue is the separation of expected statistical fluctuations from those which are non-statistical. There is also a significant background of non-critical fluctuations from physical processes unrelated to a thermodynamic phase transition [27]. The inherent difficulty in devising a method to measure fluctuations that minimizes experimental artifacts and discriminates statistical from non-statistical effects has resulted in a vast of array of competing measures, methods, and results which greatly complicates the field. Event-by-event mean transverse momentum fluctuations provide a typical illustration where NA49 and CERES at SPS have each created their own measures, while at RHIC PHENIX has one and STAR has two. These measures are often not directly proportional to one another as bias and acceptance dependences appear. However, they all have an essential element in common: an integral of a covariance. This observation is of fundamental importance, and the implications will motivate the research program below. In this work we will focus on one of STAR's fluctuation measures which incorporates the best principles of measure design learned over the history of the field.

An analysis of event-wise transverse momentum production could potentially yield an indication of critical fluctuations, or a unique class of events outside of the typical distribution. The starting quantity is the average transverse momentum taken as a scalar sum for all particles within a detector's kinematic acceptance for each event:

$$\langle p_t \rangle = \frac{1}{N} \sum_{i=1}^{N} p_{t,i} \tag{3.1}$$

where i is a particle index and N is the event multiplicity. This definition exposes two immediate problems. First, $\langle p_t \rangle$ depends on both the number of particles and distribution of momentum. Both of these are subject to random fluctuations, and fluctuations in either variable contribute to the final ratio. Convoluting these fluctuations limits the usefulness of simply measuring $\langle p_t \rangle$ distributions. Instead, a measure can be designed to separate random multiplicity fluctuations from fluctuations in p_t. The second problem is that of detector acceptance, and more generally, scale dependence. Any fluctuation occurs over a certain scale, or characteristic length, and the range over which a sample of particles is taken determines which fluctuation scales are relevant. In this context, consider particles binned on a histogram in η and ϕ, where the fluctuation is computed for each bin. Here, the histogram bin size determines the scale. The entire detector acceptance provides one limiting scale, while the other limit is the single-particle scale in which bins are small enough that each occupied bin contains exactly one particle. Not only does the scale dependence contain essential physics information, it also provides a basis for extrapolating from one detector's acceptance to another. It also plays an important role in measure design by requiring that any competent fluctuation measure not fail or suffer large systematic error in the single-particle limit.

The $\langle p_t \rangle$ fluctuation measure $\Delta\sigma^2_{p_t:n}$, defined in [28], is designed to specifically address both of these problems. Consider a *parent* p_t distribution, a fixed global distribution which is sampled by all particles from all events, with mean $\hat{p}_t$ and variance $\sigma^2_{\hat{p}_t}$. Then for many events, defined as independent samples of n particles from the parent p_t distribution, the central limit theorem (CLT) states that the r.m.s. width of the $\langle p_t \rangle$ distribution approaches $\sigma_{\hat{p}_t}/\sqrt{n}$. Applying this result, the distribution of $\langle p_t \rangle$ can be converted into a distribution with a mean of zero and variance of one by transforming to the quantity $(\langle p_t \rangle - \hat{p}_t)/(\sigma_{\hat{p}_t}/\sqrt{n})$. This quantity is plotted as the histogram in the top panel of figure 3.1 for 183k central 130 GeV Au+Au collisions. The first observation is that this distribution is smooth. There are no apparent unique classes of events with unusually high or low $\langle p_t \rangle$. The dashed line and the colored line underneath it provide the statistical references. The data are measured to be $13.7 \pm 1.4\%$ broader in r.m.s. width than the references, thus showing non-statistical fluctuations.

This fluctuation can be quantified by comparing the variance of $\sqrt{n}(\langle p_t \rangle - \hat{p}_t)$ to $\sigma^2_{\hat{p}_t}$, which motivates the fluctuation measure

$$\Delta\sigma^2_{p_t:n} \equiv \frac{1}{\epsilon}\sum_{j=1}^{\epsilon} n_j[\langle p_t \rangle_j - \hat{p}_t]^2 - \sigma^2_{\hat{p}_t} \tag{3.2}$$

$$\equiv 2\sigma_{\hat{p}_t}\Delta\sigma_{p_t:n} \tag{3.3}$$

where ϵ is the number of events within the centrality bin, j is the event index, n_j and $\langle p_t \rangle_j$ are the multiplicity and mean p_t of event j, and $\hat{p}_t$ and $\sigma^2_{\hat{p}_t}$ are defined as above as the respective mean and variance of the inclusive p_t distribution of all accepted particles in the event ensemble. Equation 3.2 defines the fluctuation measure $\Delta\sigma^2_{p_t:n}$

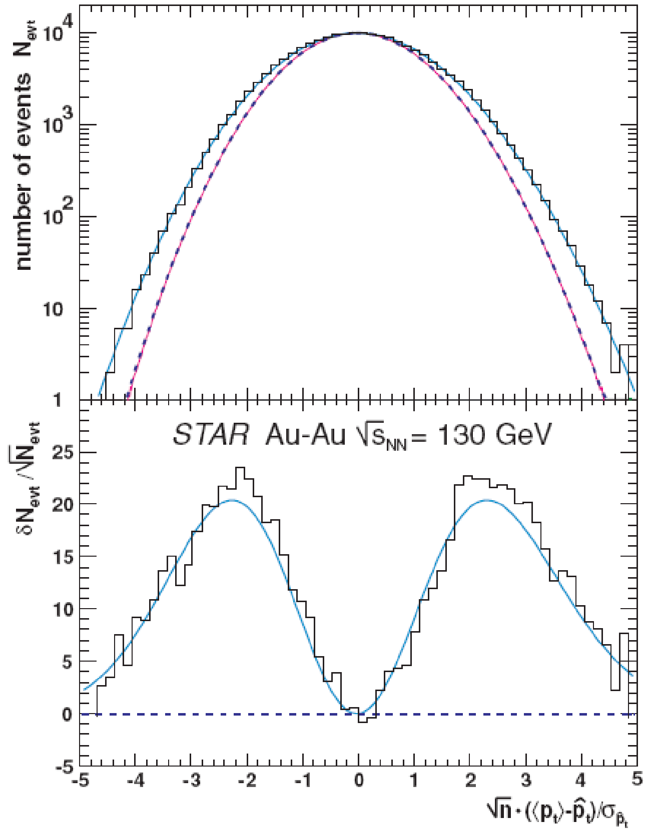

Figure 3.1: Top panel: Distribution of normalized $\langle p_t \rangle$ (histogram) compared to gamma reference (dashed curve) and Monte Carlo references (solid curves). Bottom panel: Difference between data and references scaled by bin error. From [28].

as a variance excess incorporating many desirable properties. First, the CLT scaling of a distribution ensures no dependence on trivial multiplicity fluctuations, and overall multiplicity dependence is removed by defining $\Delta\sigma^2_{p_t:n}$ as excess variance *per-particle*. Second, the statistical reference is built in to the definition, so any non-zero value of $\Delta\sigma^2_{p_t:n}$ shows only non-statistical fluctuations. Finally, by using the scale invariance of the total variance, as shown in the appendix of [28], $\Delta\sigma^2_{p_t:n}$ is by construction able to measure fluctuations at any scale without statistical bias.

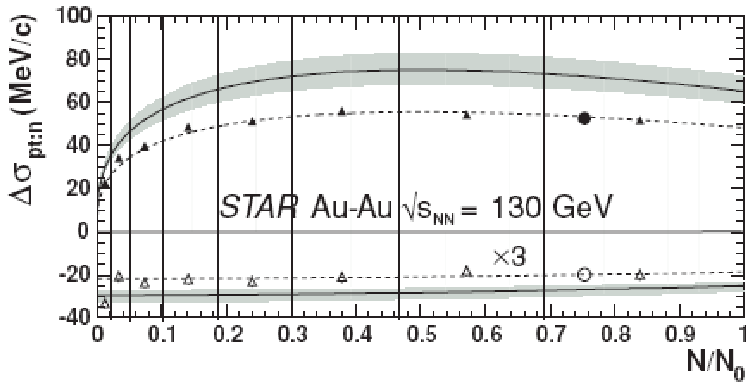

Figure 3.2: Centrality dependence of $\langle p_t \rangle$ fluctuation measure for charge-independent (solid points) and charge-dependent (open points) cases. Solid curves represent efficiency-corrected extrapolations. Ratio N/N_0 shows fraction of event multiplicity N with respect to maximum multiplicity N_0 in the most central collisions.

Equation 3.3 defines difference factor $\Delta\sigma_{p_t:n}$, which is approximately equal to a previously used measure to make inter-experiment comparisons more convenient. The centrality dependence of $\Delta\sigma_{p_t:n}$ is shown in figure 3.2. Solid points represent $\Delta\sigma_{p_t:n}$ as defined above, which is charge-independent (CI) as it does not distinguish the electric charge sign of particles. A charge-dependent (CD) version, shown in open points, can be defined by separating terms in equation 3.2 into sums over positive and negative charges, then taking the difference between the like-sign and unlike-sign pairs. Centrality bins of a min-bias data sample are shown with triangles, while circles show the top 15% central triggered events. Solid curves show the extrapolated result after correcting for detector inefficiencies.

The results from this analysis show no evidence for critical fluctuations or anomalous event classes, but do find significant non-statistical fluctuations. Fixed target heavy ion experiments at the CERN SPS using a 158 GeV per nucleon Pb beam ($\sqrt{s_{NN}} \approx 17$ GeV) measure much smaller values of transverse momentum fluctuations. Using $\Phi_{p_t} \simeq \Delta\sigma_{p_t:n}$, NA49 finds 0.6 ± 1.0 MeV/c for central collisions with a Pb target [29], while CERES measures $3.3 \pm 0.7^{+1.8}_{-1.6}$ using a Au target. STAR's result for central Au+Au collisions at $\sqrt{s_{NN}} = 130$ GeV is $\Delta\sigma_{p_t:n} = 52.6 \pm 3$ MeV/c. The large difference indicates that significant new dynamical mechanisms are taking place. Charge-independent $\Delta\sigma_{p_t:n}$ shows non-monotonic behavior with a rapid increase followed by a slow decrease with centrality. The charge-dependent results are negative, showing that the fluctuation contribution from unlike-sign pairs is larger than like-sign pairs, and the difference is approximately constant with centrality.

The conclusions of [28] state that $\Delta\sigma_{p_t:n}$ is expected to vanish for fully equilibrated events. Since $\Delta\sigma_{p_t:n}$ is found to be large, then RHIC collisions apparently remain highly structured and do not reach complete equilibrium. However, this does not consider the possibility that each event may be completely equilibrated but the global "temperature", the $\langle p_t \rangle$ of a single event, fluctuates from event to event also producing a $\langle p_t \rangle$ fluctuation [47]. Unfortunately, it is difficult to disentangle these effects or attribute the observed fluctuations to another physical mechanism from measuring $\langle p_t \rangle$ fluctuations alone, though the scale dependence will provide insight leading to an interpretation.

3.1.2 Inversion and Correlations

The previous non-statistical fluctuations were measured at a single scale, namely the entire acceptance of the STAR TPC. Fluctuations with characteristic lengths larger than the scale do not contribute on average to the total. By successively reducing the scale, fluctuations with longer lengths are eventually excluded, reducing the total excess fluctuations. At the smallest scale, the single-particle limit, only statistical fluctuations remain and $\Delta\sigma^2_{p_t:n}$ approaches zero. The left panel in figure 3.3 shows the scale dependence of $\Delta\sigma^2_{p_t:n}$ as a function of bin sizes $\delta\eta$ and $\delta\phi$ [31]. Note that

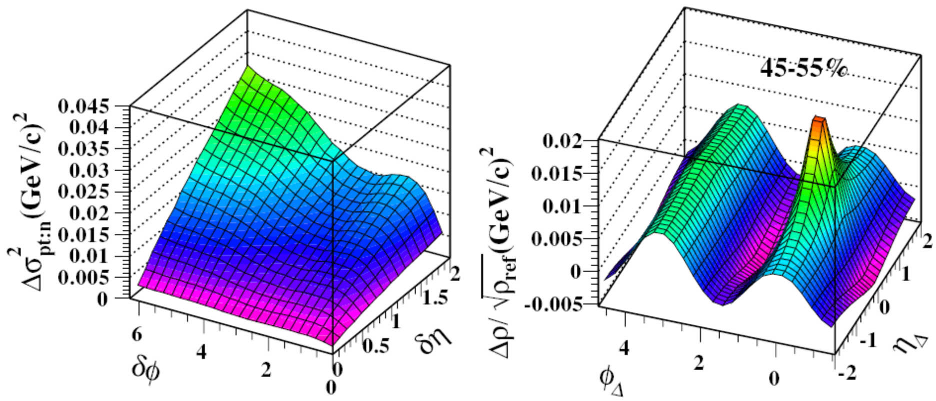

Figure 3.3: Left panel: Scale dependence of $\Delta\sigma^2_{p_t:n}$. Right panel: p_t correlations from inversion. From [31].

the fluctuation excess of figure 3.1 would correspond to the single point at the apex of maximum scale. The scale dependence contains a large amount of information and the surface is obviously structured, but what does the structure mean?

To interpret the result, we return to the common property shared among all fluctuation measures, namely that they all depend on the integral of a covariance. Instead of using this integral to form a fluctuation measure, the covariance can be measured directly. The covariance can be appropriately normalized into a correlation by forming the well-known Pearson's correlation coefficients [32]. The study of *fluctuations* is supplanted by the study of *correlations*. Information is lost as the fluctuation integrates over a highly-structured and complicated correlation surface. It may be replaced through an analysis of scale dependence, but the result obfuscates the connection to physical mechanisms.

Correlation analyses abound at RHIC, but they fall into two overall categories each specialized to study certain phenomena. Quantum correlations and HBT, a technique named after astronomers R. Hanbury Brown and R. Q. Twiss who first used interferometry to measure the size of stars [33], study a restricted phase space of small relative momentum, while high-p_t trigger particle analyses give conditional yields for only the highest momentum particles and ignore the remaining 98%. Jet physics is presently one the largest research programs at RHIC, but the present lack of knowledge regarding correlations at lower p_t limits the ability to separate jets from other correlated backgrounds. Instead of these specialized analyses, a much more general approach to correlations is needed to shed light on fluctuation results and place other correlation analyses within a larger context.

The exact relation between fluctuations and correlations is the subject of [34]. The detailed formalism of correlations, to be studied in the following chapter, is necessary to show the relation rigorously. For present purposes, a simplified relation is:

$$\Delta\sigma^2_{p_t:n}(\delta\eta, \delta\phi) \quad = \quad 4\epsilon_\eta\epsilon_\phi \sum_{i,j} K \, \frac{\Delta\rho(p_t : n)}{\sqrt{\rho_{ref}(n)}}(i\epsilon_\eta, j\epsilon_\phi) \tag{3.4}$$

where kernel K contains histogram binning information, δx represents a fluctuation scale, ϵ_x is a correlation bin width with indices i and j, and $\frac{\Delta\rho}{\sqrt{\rho_{ref}}}$ is a per-particle correlation density related to Pearson's correlation coefficient. Equation 3.4 is a Fredholm integral equation which can be inverted using standard numerical methods to obtain the correlation $\frac{\Delta\rho}{\sqrt{\rho_{ref}}}$ from the (scale-dependent) fluctuation $\Delta\sigma^2_{p_t:n}$. Figure 3.3 shows a corresponding set of $\langle p_t \rangle$ fluctuations and p_t correlations from inversion for 200 GeV Au+Au collisions at 45-55% centrality [31], providing a visualization of the correlations that drive the non-statistical fluctuations observed previously. The axes on the right panel show relative separation $\eta_\Delta \equiv \eta_1 - \eta_2$ and $\phi_\Delta \equiv \phi_1 - \phi_2$. The stated purpose of measuring correlations was to relate measured structures to physical processes, so the next task at hand is to study expected sources of correlations and their contributions to data. These references must be examined before interpretation of the correlations in figure 3.3 is possible.

3.2 Two Component Model

Before embarking on a new research program of minimum-bias correlations, not only as a way to understand fluctuation measurements but to directly probe the dynamics of heavy ion collisions, we need a baseline of expectations. A particularly simple ansatz for studying high energy collisions is the two component model of [35]. Assume that a proton-proton collision produces n_{pp} particles per unit (pseudo)rapidity, and that some fraction x is due to "hard" processes while the remaining fraction is "soft". In this model, a heavy ion collision is then composed of several independent nucleon-nucleon collisions. Each nucleon in the collisions contributes to producing low momentum, or soft, particles, while high momentum hard particles are produced when any two nucleons directly collide. Thus, soft processes are assumed to scale as N_{part}, the number of nucleons participating in the collision, and the hard processes scale as the number of binary nucleon-nucleon collisions N_{bin}. The total multiplicity density is then:

$$\frac{dn}{d\eta} = (1-x)n_{pp}\frac{\langle N_{part}\rangle}{2} + xn_{pp}\langle N_{bin}\rangle \tag{3.5}$$

where angle brackets show event-wise averages.

The same two component model is used by several event generators including Pythia [36] and HIJING [37]. In these simulations, the hard component is implemented as a large momentum transfer hard-scattering pQCD process, which is well understood theoretically, while the soft component contains contributions from elastic scattering, diffraction, and fragmentation based on phenomenological models.

The multiplicity distributions are largely insensitive to values of x as shown in figure 3.4. By introducing centrality measure $\nu \equiv \frac{\langle N_{bin}\rangle}{\langle N_{part}\rangle/2}$ and rearranging equation

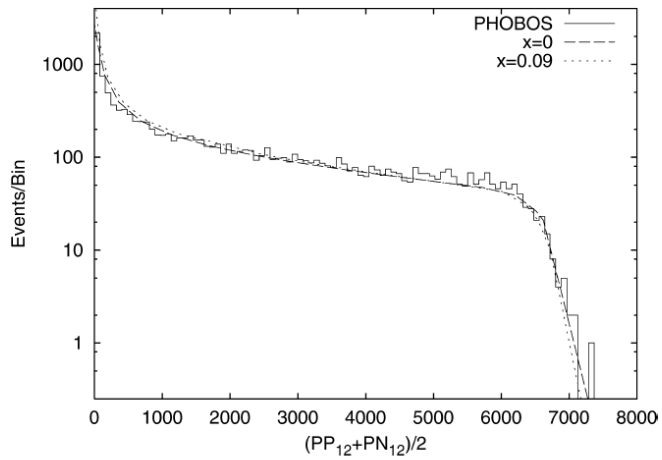

Figure 3.4: The two component multiplicity distributions for two values of x compared to PHOBOS data. From [35].

3.5 we find:

$$\frac{2}{\langle N_{part}\rangle}\frac{dn}{d\eta} = (1-x)n_{pp} + xn_{pp}\nu \tag{3.6}$$

$$= n_{pp}[(1-x) + x\nu] \tag{3.7}$$

$$= n_{pp}[x(\nu-1)+1]. \tag{3.8}$$

Therefore x is best determined by the differential centrality dependence, since $\frac{dn}{d\eta}$ divided by $\langle N_{part}\rangle/2$ should be linear as a function of ν with slope x and should smoothly extrapolate to the p+p limit. Figure 3.5 presents results from [38] showing that this linear relation holds for protons (right panel) and kaons (left panel, bottom), but not pions (left panel, middle). This implies that the pion x has significant centrality dependence as the slope steepens from point to point. The other lines provide linear references for various values of x. The left-most points at $\nu = 1$ are from 200 GeV p+p collisions, while the points in $\nu \approx$ 2-6 represent 200 GeV Au+Au data in five centrality bins. The combined result for all hadrons (left panel,

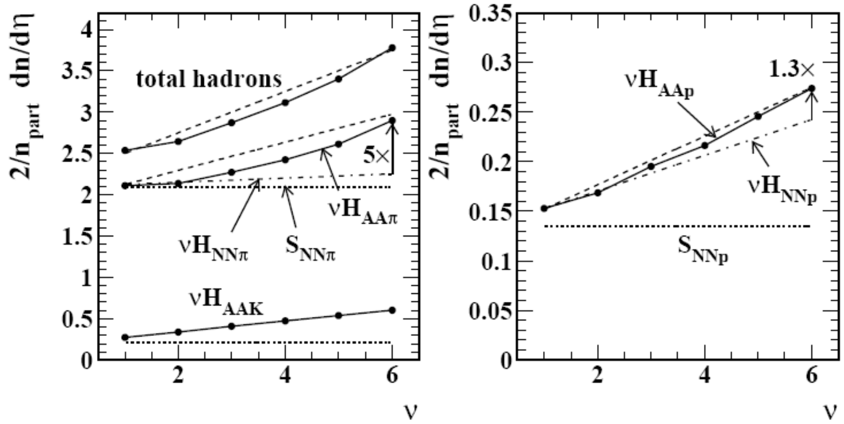

Figure 3.5: Testing two component predictions of a linear relationship with ν and a slope of x. Solid points and lines show data for identified pions (left middle), kaons (left bottom), protons (right), and combined total (left top) for 200 GeV p+p ($\nu =$ 1) and Au+Au in five centrality bins (ν from 2-6). The dashed lines provide linear references for various values of x. From [38].

top) is only approximately linear on ν due to the pion contributions.

3.3 Proton-Proton Reference

The two component model provides a framework for studying correlations in heavy ion collisions. First, we must determine if these components can be observed in a correlation analysis, which may also provide insight as to the contributing physical processes. Then we study how these components change from proton-proton to heavy ion collisions. This section reviews p+p collisions as a simpler system for understanding how different processes contribute to the measured correlations, providing an essential reference for Au+Au data.

3.3.1 Two Component Spectra

The multiplicity dependence of the p_t spectra provides an elegant way for studying proton-proton collisions [39] and testing the validity of the two component model. The soft component is defined as a limiting case where the observed event multiplicity approaches zero. This approach allows the soft component p_t spectrum to be measured without ever invoking a physical production mechanism. Figure 3.6 shows the measured p_t distributions (points connected by dotted lines) for ten event multiplicity classes based on mean number of detected charged particles $\hat{n}_{ch}$. Event classes are offset for clarity from the $\hat{n}_{ch} = 1$ events along the bottom to $N_{ch} = 11.5$ at the top. The solid line shows comparisons to the inferred soft component reference. The lowest multiplicity class is well represented by the soft reference, while other classes show more deviation from the soft reference with higher multiplicity and p_t. The soft component reference was chosen to be a Lévy distribution [40]:

$$S_0(m_t; \beta_0, n) \quad = \quad A_s/(1 + \beta_0(m_t - m_\pi)/n)^n \tag{3.9}$$

for transverse mass $m_t \equiv \sqrt{p_t^2 + m_\pi^2}$ where the pion mass m_π has been assumed for all (unidentified) particles. Amplitude A_s is fixed by normalization while parameters β_0 and n are fit to the data.

The right panel of 3.6 is identical except p_t has been transformed to transverse rapidity y_t with

$$y_t \quad = \quad \ln{(m_t + p_t)}/m_\pi. \tag{3.10}$$

A y_t of 2.0 corresponds to $p_t = 0.51$ GeV/c, similarly $y_t = 3.0 \rightarrow p_t = 1.40$ GeV/c, and $y_t = 4.0 \rightarrow p_t = 3.82$ GeV/c. Longitudinal fragmentation has long been studied on longitudinal rapidity y_z, now the same approach is being applied in the transverse direction. The typical presentation style of showing transverse spectra as a function

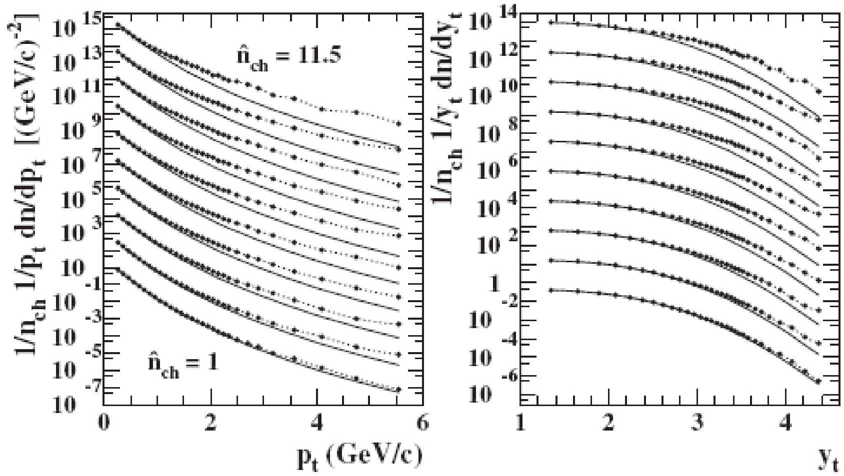

Figure 3.6: Spectra of 200 GeV p+p collisions divided into ten multiplicity classes as a function of p_t (left) and y_t (right). Points with dashed lines show data, while the solid curve is the soft component reference. From [39].

of p_t forces the vast majority of particles to the low p_t edge of the plot. This focuses attention on the tail of the distribution which contains just a few percent of highest p_t particles. Since $y_t \sim \ln p_t$ the transverse rapidity distribution is significantly flatter.

Higher multiplicity events include successively greater fractions of the hard component, which can now be easily isolated by subtracting the soft component from the data with appropriate normalization, as discussed below. Figure 3.7 left panel gives the scaled y_t minus soft reference $S_0(y_t)$. The excess in the left corner is from low multiplicity classes, while high multiplicity classes follow Gaussian curves (solid lines) with constant means and increasing amplitudes. In the right panel event classes have been normalized to overlay each other. Higher multiplicity events show

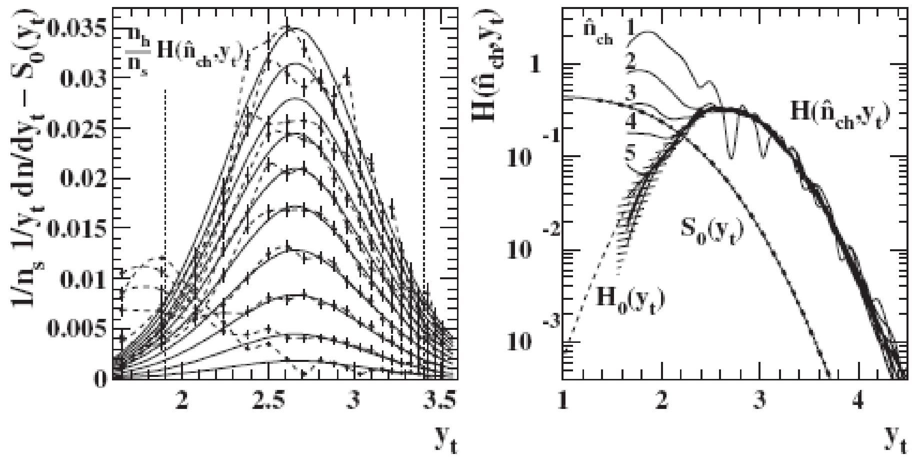

Figure 3.7: Left panel: the isolated hard component follows a Gaussian with constant mean but increasing amplitude. Right panel: when overlayed, the higher multiplicity events show only small deviations from the hard component reference. From [39].

only small deviations from the hard component reference, defined as

$$H_0(y_t; \bar{y_t}, \sigma_{y_t}) \quad = \quad A_h \exp\left\{-\frac{1}{2}\left[\frac{y_t - \bar{y_t}}{\sigma_{y_t}}\right]^2\right\}. \tag{3.11}$$

With the possible exception of the $\hat{n}_{ch} = 1 - 4$ classes at low y_t, all of the p+p data are well-described by a simple combination of these two components. The explicit two component model is then

$$1/y_t\, dn/dy_t \quad = \quad n_s(\hat{n}_{ch})S_0(y_t) + n_h(\hat{n}_{ch})H_0(y_t) \tag{3.12}$$

for event class $\hat{n_{ch}}$ with soft and hard component multiplicities n_s and n_h. Components S_0 and H_0 each have two parameters, and one additional parameter is required for the relative fraction of soft to hard since this is observed to follow a nearly linear trend. It is noteworthy to mention that this model with five parameters provides a better fit to the data than a thirty parameter power-law fit where each event class is fit separately. In terms of the specific Kharzeev and Nardi model, this analysis measures a hard scattering frequency x of 0.012 ± 0.004 per unit pseudorapidity.

3.3.2 Transverse Correlations

We have now identified the soft and hard components in the *transverse* (p_t or y_t) space based on single particle spectra alone. No assumptions have been made as to physical mechanisms generating these components. Now we return to a correlation analysis to search for these components.

Minimum-bias correlations in 200 GeV p+p collisions are well-cataloged in [41]. Figure 3.8 shows a side-by-side comparison of the previous analysis with transverse minimum-bias correlations. The correspondence is striking. The correlations show two distinct regions with a low y_t soft component, and a semi-hard component as a Gaussian with the same mean as in the spectra analysis.

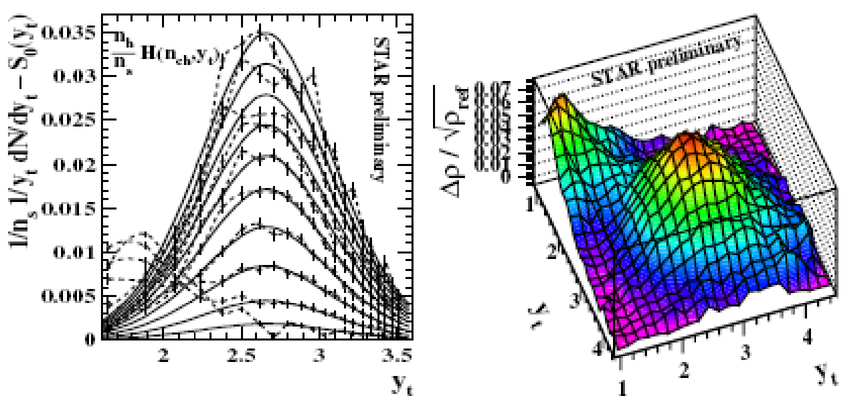

Figure 3.8: Comparison of the y_t components in spectra (left) and correlation (right) analyses. From [41].

The details of the correlation analysis are the subject of following chapters, but the procedure is summarized as forming all possible pairs of particles within an event and simply counting the number of pairs which fall into a certain histogram bin, here (y_{t1}, y_{t2}). Then an uncorrelated background, which is found by mixing particles from different events, is subtracted and the result is normalized to obtain a correlation. A primary source of correlations is multiple particle production from quark fragmentation. The laws of QCD prohibit a single quarks existing freely, so energy from the quark is used to form new quark-antiquark pairs which combine into hadrons. Fragmentation may be a soft or hard process since all quarks, regardless of high or low energy, must form hadrons. From simple kinematic reasons alone, at mid-rapidity a low p_t soft particles are primarily produced from quarks traveling and fragmenting longitudinally, while high p_t hard particles are primarily produced in transverse fragmentation.

Since this is a pair-wise analysis, we can now differentiate between the electric charge signs and opening angles of the pairs to isolate and study different contributions. Figure 3.9 shows transverse correlations for four of these combinations [41]. The rows distinguish pair opening angle on azimuth. Defining $\phi_\Delta \equiv \phi_1 - \phi_2$ gives *same-side* (SS) pairs for $|\phi_\Delta| < \pi/2$, and *away-side* (AS) pairs with $|\phi_\Delta| > \pi/2$. The columns separate electric charge sign into *like sign* (LS) for $++$ and $--$ pairs, and *unlike sign* (US) for $+-$ and $-+$ pairs. The top-left panel is SS LS and is dominated by a soft component. This is interpreted as quantum correlations (HBT), which are expected for SS LS but not US pairs. Local charge conservation suppresses SS LS pair production, unless the parton has sufficient energy to fragment into several hadrons which can create a next-to-nearest neighbor LS correlation. The small signal in the hard component may represent HBT correlations among hard particles instead of LS fragmentation. The top-right panel is SS US, which shows a large hard component peak elongated along the diagonal $y_{t\Sigma} \equiv y_{t1} + y_{t2}$ which runs smoothly into the soft component. These panels show that the same-side is primarily soft LS pairs and hard US pairs. The bottom row in 3.9 contains the away-side pairs. The

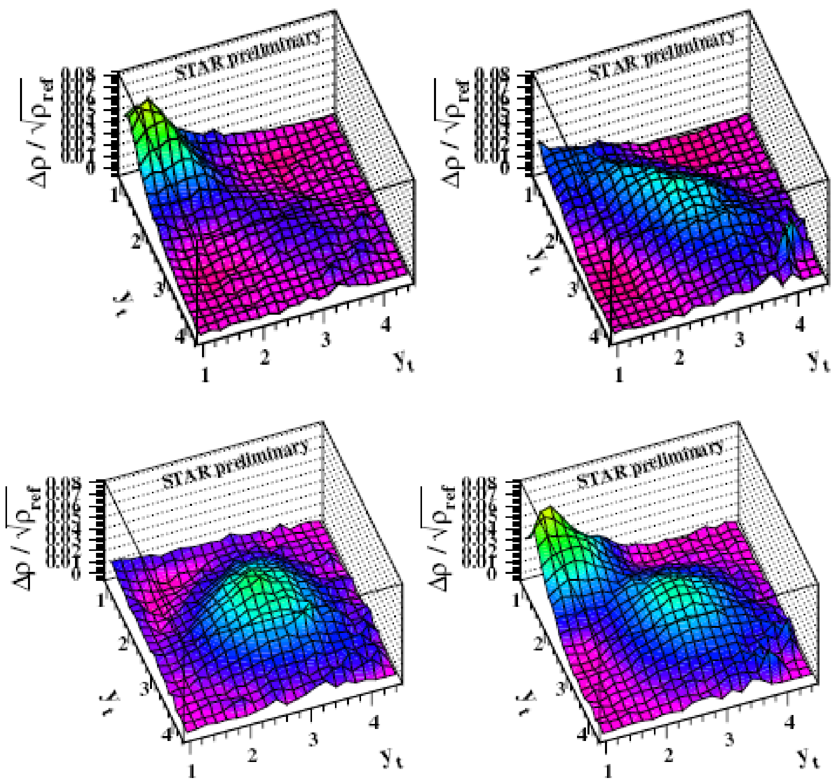

Figure 3.9: Transverse correlations in 200 GeV p+p collisions for four different cases of charge sign and opening angle. Top row: same-side; bottom row: away-side. Left column: like-sign; right column: unlike-sign. From [41].

bottom-left is then AS LS which contains only a hard component. The final panel is the bottom-right with AS US and shows strong peaks in both components.

These observations supply a great deal of information about the physics contributing to each component. It is expected that soft pairs will be produced from low p_t particles with small momentum transfer interactions. Thus soft pairs should be back-to-back in the lab frame with opposite charge sign, explaining the large signal seen in AS US. The soft component signal in SS LS, along with the absence of a large signal in AS LS or SS US, is expected from HBT correlations [42].

The hard component shows SS and AS signals, as expected for back-to-back minijets. The SS US elongation is indicative of a fragmentation process preferentially creating pairs of hadrons with similar values of p_t. The AS hard peaks are more symmetric, simply showing distributions of $p_t$about a mean, and the similarities in the AS LS and US show that the back-to-back correlation is not as charge dependent as the SS fragmentation.

3.3.3 Axial Correlations

A two-particle correlation is a quantity with six momentum components $(p_{t1}, \eta_1, \phi_1, p_{t2}, \eta_2, \phi_2)$. The previous results, preferring $y_t$to p_t, analyzed the *transverse* space (y_{t1}, y_{t2}). Visualizing the four-dimensional $(\eta_1, \phi_1, \eta_2, \phi_2)$ *axial* space is more challenging. However, the problem is simplified by transforming to a coordinate system which takes full advantage of symmetries in the observed correlations.

Figure 3.10 presents axial correlations (η_1, η_2) and (ϕ_1, ϕ_2) for LS and US pairs [43] in 130 GeV Au+Au collisions. The invariance along the main diagonals is immediately apparent. Axial correlations within the STAR TPC show virtually no dependence on $\eta_1 + \eta_2$ or $\phi_1 + \phi_2$. By projecting onto the off-diagonals, defined as $(\eta_\Delta \equiv \eta_1 - \eta_2, \phi_\Delta \equiv \phi_1 - \phi_2)$, the entire 4-D axial space can be shown in only two dimensions $(\eta_\Delta, \phi_\Delta)$ without loss of information.

Returning to p+p, we can now study the soft and hard components in axial space. Since the two components are well separated in (y_{t1}, y_{t2}) they can be isolated by y_t cuts. Figure 3.9 motivates the definition of soft pairs as $y_t < 2$ ($p_t < 0.5$ GeV/c) and hard pairs by $y_t > 2$ for each particle. The soft and hard axial correlations for LS and US pairs [41] is shown in figure 3.11.

From the transverse results, it was concluded that the soft pairs come primarily from HBT (SS LS) and soft fragmentation (AS US). The top row in 3.11 shows soft pairs in axial space. The top-left panel, soft LS pairs, is dominated by

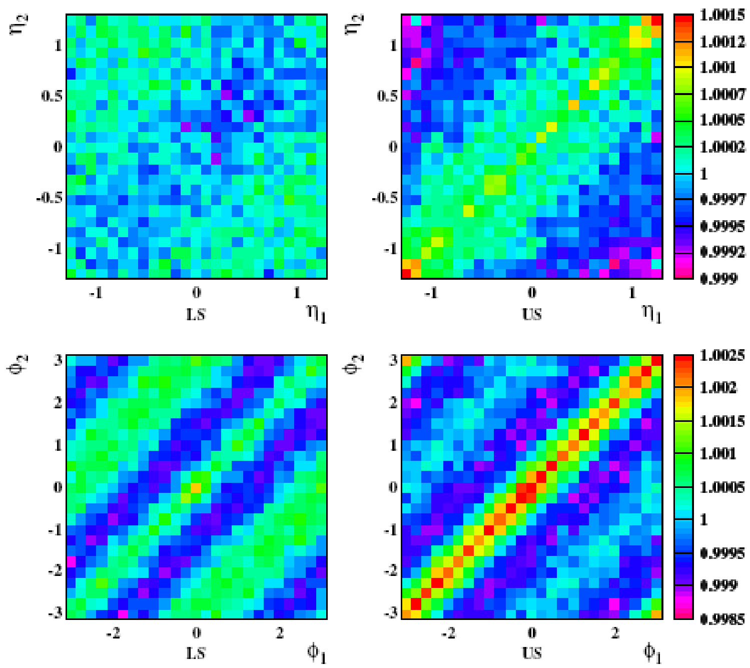

Figure 3.10: 4-D axial correlations for LS (left column) and US (right column) pairs. From [43].

a SS peak consistent with HBT expectations. The US pairs in the top-right panel show a Gaussian on $\eta_\Delta$which is partially suppressed on the SS, and a sharp peak at the origin from electron-positron pairs. Hard pairs are presented in the bottom row, again with LS on the left and US on the right. As seen in the transverse correlations, the hard AS peak is very similar for both charge types, whereas the SS hard peak is dominated by US correlations.

Pythia [36] gives another test of the correspondence from physical processes to correlations. Pythia traces its roots to a program called JETSET which was started in 1978 by the Lund theory group. JETSET is a string fragmentation model based on a phenomenological picture of QCD confinement. The model, now often referred to as the Lund string model [44], gained widespread acceptance after

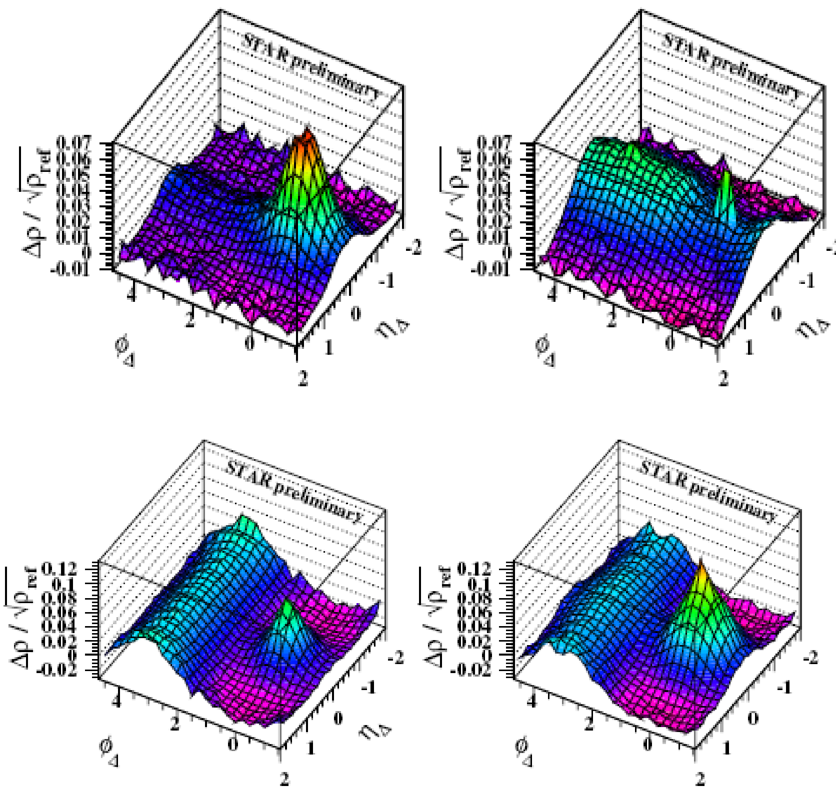

Figure 3.11: Axial correlations in p+p. Top row: soft pairs; bottom row: hard pairs. Left column: like-sign; right column: unlike-sign. From [41].

several specific predictions were confirmed in electron-positron collisions at PETRA and PEP [36]. In this model, partons interact with a one-dimensional color flux tube called a string, which contains an energy per unit length (or tension) on the order of 1 GeV/fm. If interacting partons move apart the binding energy increases. Eventually the string "breaks" and a new quark-antiquark pair is formed from the vacuum. The hadronization is handled iteratively, so when a diquark pair is produced a new hadron is formed and the rest of the string continues to fragment until some minimum energy is reached. As experimentally accessible energies increased, it became necessary to add pQCD hard processes to Pythia which were originally based on simple leading-order matrix element calculations.

A comparison in [45] shows very good agreement between Pythia and STAR data for p+p minimum-bias correlations. The soft US pairs correspond to longitudinal fragmentation as in the Lund string model. The data show strong US nearest neighbor correlations as predicted by string fragmentation, however neither charge type shows any indication of next-to-nearest neighbor correlations. These data suggest that the term 'string' may be a misnomer as only single pair production is observed, thus the more generic term of *longitudinal* fragmentation is preferred. Pythia lacks a model of HBT correlations, and thus underpredicts the soft LS structure. The hard pairs agree well with the minijet fragmentation model. Since this model is based on pQCD and extrapolated to lower momenta, it contains an arbitrary low p_t cutoff not observed in the data.

3.4 Gold-Gold Correlations and Spectra

The p+p correlations have provided a reference of correlation structures. From this basis of understanding, we now explore transverse correlations, axial correlations, and the two component spectra in Au+Au collisions.

3.4.1 Transverse Correlations

Analysis of 130 GeV Au+Au minimum-bias correlations provided the first glimpse of these correlation structures at RHIC. The limited p_t range (< 2.0 GeV/c) and relatively small number of events prohibited a detailed study. Instead, these analyses provided a proof of principle for the minimum-bias correlation technique and evidence for the large role minijets play in heavy ion collisions.

The correlation measure used at 130 GeV, $\bar{N}(\hat{r}-1)$, predates the form directly corresponding to Pearson's correlation coefficient denoted as $\frac{\Delta\rho}{\sqrt{\rho_{ref}}}$. They can be related as

$$\bar{N}(\hat{r}-1) \simeq \Delta\eta\Delta\phi\frac{\Delta\rho}{\sqrt{\rho_{ref}}} \tag{3.13}$$

where $\Delta\eta$ and $\Delta\phi$ represent acceptance ranges, respectively 2.6 and 2π for the 130 GeV analysis. This relation is based on the two-particle density scaling as mean number of pairs: $\sqrt{\rho_{ref}} = d^2N/d\eta d\phi \simeq \bar{N}/\Delta\eta\Delta\phi$, as explained in the next chapter. Additionally, the utility of transverse rapidity y_t was not realized at the time, so the quantity $X(p_t) \equiv 1-\exp\left[-(m_t - m_\pi)/0.4\right]$ was defined to flatten the p_t distribution. Approximately 300k events were divided into four centrality bins defined as 40-70%, 17-40%, 5-17%, and 0-5% of the approximate total cross section. Figure 3.12 shows the transverse correlation structure reported in [47].

Two primary features are apparent in figure 3.12. The peripheral events in panel (d) show a sharp peak at large $X(p_t)$ (corresponding $p_t > 0.6$ GeV/c) revealing the lower edge of the hard component peak, as this analysis was limited to $p_t < 2.0$ GeV/c. This structure persists at all centralities, however increasing centrality also shows the development of a saddle-like structure at lower $X(p_t)$. A model of temperature fluctuations in a partially equilibrated system is shown to reproduce the saddle shape well, see figure 3.13. The left panel shows the saddle model fit for mid-central collisions. The right panel shows the residual of model subtracted from the data, isolating the remainder of the hard component peak.

The fits obtained from the saddle shape are consistent with a few percent global event-to-event temperature/velocity fluctuation or 30% local fluctuations within each event, or some combination of the two. The centrality dependence follows the hypothesis that minijet momentum dissipation into the collision system is the source of local fluctuations. In this picture, minijet fragments are shifted to lower p_t with increasing centrality, asymptotically approaching random temperature or velocity variations within an incompletely equilibrated system.

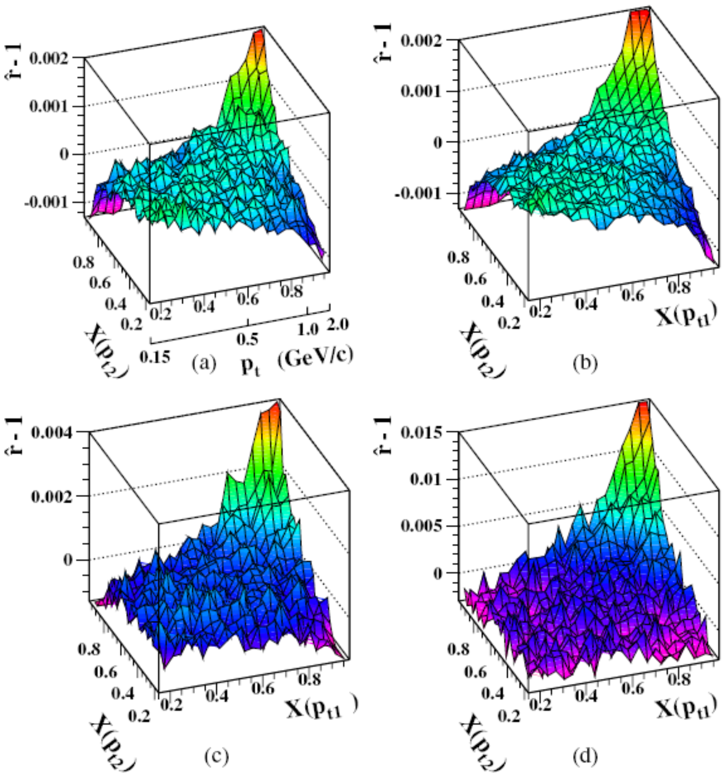

Figure 3.12: Transverse correlations for central (a) through peripheral (d) 130 GeV Au+Au collisions. From [47].

3.4.2 Axial Correlations

The transverse correlation results suggest interactions between the minijets and the heavy ion collision medium. These interactions may also be explored with axial correlations. By using a per-particle correlation measure, which is by construction independent of multiplicity, the structures in p+p collisions in figure 3.11 may be compared directly to those in Au+Au events. As outlined above, the 130 GeV analysis used 300k events among four centrality bins and a correlation measure described in 3.13.

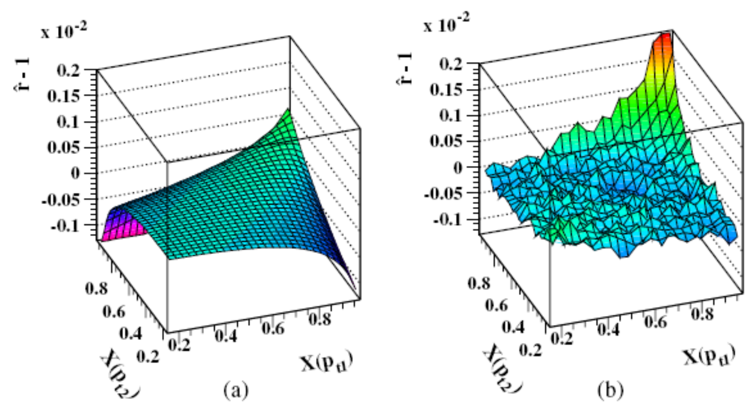

Figure 3.13: Left panel: model function of the saddle shape for mid-central collisions. Right panel: data minus the model showing the remaining sharp peak. From [47].

Charge-Independent

Reference [48] presents the axial correlations for all pair charge types. Figure 3.14 shows the correlation structure from peripheral (panel d) to central (panel a) collisions. The most peripheral bin, covering cross section fraction 40-70%, is substantially different from the p+p results (the limit approaching 100% centrality), as limited statistics prevented a detailed mapping of the transition from nucleon-nucleon to heavy ion collisions. One difference is the large $\cos(2\phi_\Delta)$ correlation, a *quadrupole* term in the language of multiple moments, conventionally attributed to elliptic flow [49]. To facilitate more comparisons, this component along with a significant $\cos(\phi_\Delta)$ dipole most visually apparent in panel (c) have been subtracted in figure 3.15.

In p+p collisions, soft pairs were observed in HBT correlations and US longitudinal fragmentation, which forms a Gaussian along η_Δ. In this analysis, HBT contributions were suppressed by cutting LS pairs with small relative momentum. The flatness of the away-side in figure 3.15 shows no indication of this longitudinal

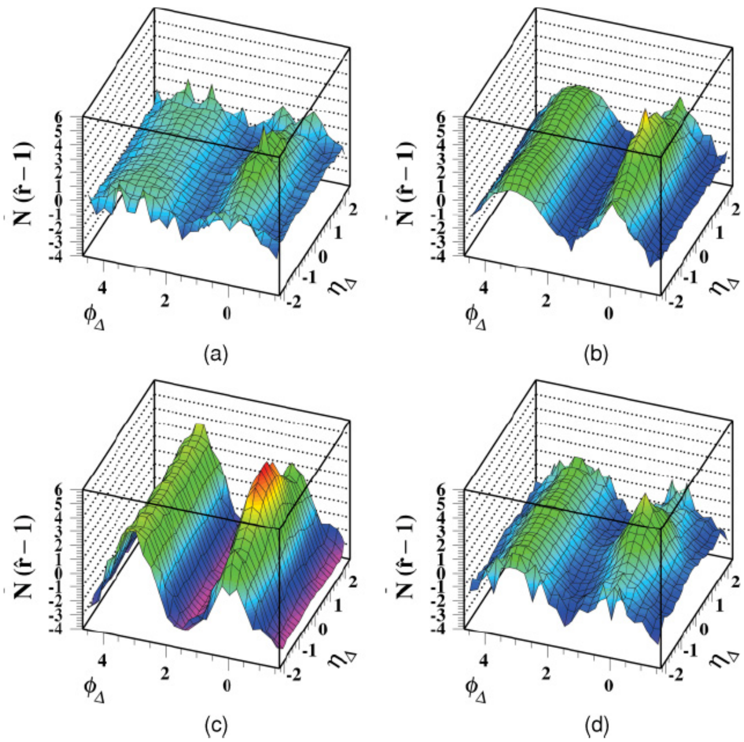

Figure 3.14: Axial correlations in 130 GeV Au+Au peripheral (d) to central (a) collisions. From [48].

fragmentation as observed in p+p, suggesting that the dominant particle production mechanism in nucleon-nucleon collisions may be irrelevant in heavy ion collisions.

The HBT cut ensures that the SS peak almost entirely consists of hard pairs (although a 2.0 GeV/c upper limit on p_t has been imposed). Figure 3.15 shows significant centrality dependence of this peak, which may be quantified by fitting with a two dimensional Gaussian function. Figure 3.16 shows the extracted fit parameters for the amplitude, widths, and volume of this peak moving from left to right panels respectively. These trends reveal a large amplitude and η_Δ width increase along with a ϕ_Δ width decrease for more central collisions, indicating a significant modification of the minijet peak.

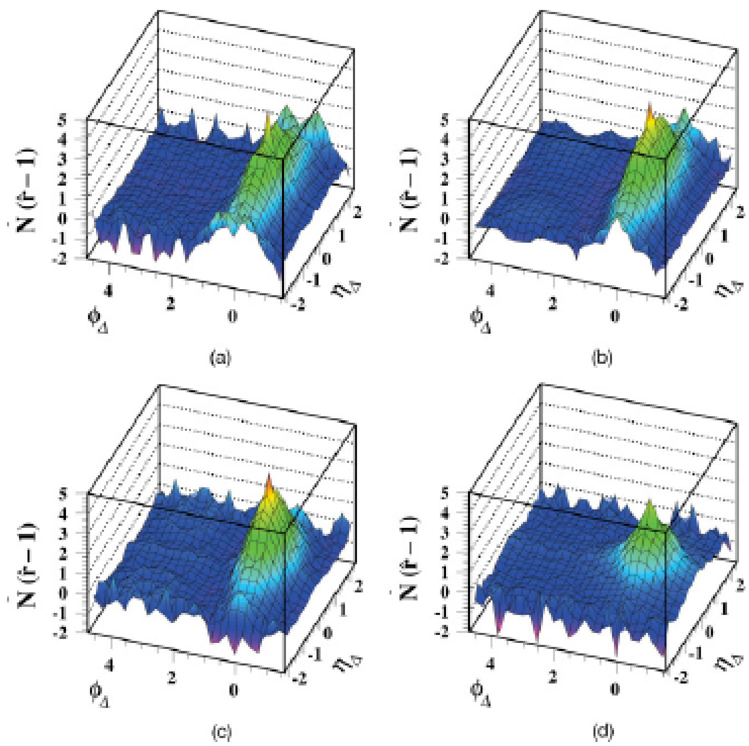

Figure 3.15: Data from figure 3.14 with dipole and quadrupole moments subtracted. From [48].

Charge-Dependent

To directly compare the difference between like-sign and unlike-sign pairs, the analysis in [50] defines the charge-*dependent* correlation CD = LS - US. The results of the previous section contains all pair charge types, and were thus charge-*in*dependent CI = LS + US. The choice of sign in the charge-dependent definition is motivated by pair counting arguments, see chapter 4. The CD correlations are shown in figure 3.17.

The proton-proton CD correlations [45] are dominated by a negative Gaussian on η_Δ from longitudinal fragmentation. HBT and minijet fragmentation con-

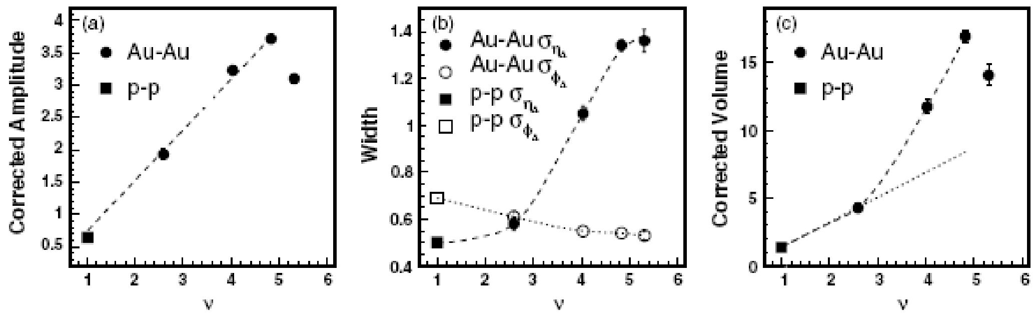

Figure 3.16: Fit parameters of the same-side peak amplitude (a), widths (b), and volume (c) for 200 GeV p+p and 130 GeV Au+Au in four centrality bins. From [48].

tribute to a significant positive component near the origin. This large asymmetry between η_Δ and ϕ_Δ is not observed in the Au+Au data, moreover the shape of the structure is changing as well. Motivated by the apparent trend from a 1-D Gaussian in p+p to a 2-D exponential in Au+Au, the CD correlations were fit with a superposition of these two functions. The left panel in figure 3.18 shows the amplitudes of these terms with the p+p is shown to be purely Gaussian while the most central bin is almost entirely exponential. The right panel presents the exponential widths where $\sigma_\phi \to \infty$ for p+p.

Local charge conservation demands that minijet fragmentation be inherently charge-dependent, as was seen in the large difference between LS and US same-side hard pairs in p+p collisions. The CD correlations can show if the broadening of the same-side minijet peak is due to a change in fragmentation or, as hypothesized above, a medium interaction. Significant η_Δ broadening of the CD correlation would be indicative of a change in fragmentation, while medium interactions are expected to affect all charges equally. The large increase in η_Δ width in CI contrasted with the relatively small changes in CD provide evidence for the medium interaction scenario. The change in shape from Gaussian to exponential may also be consistent

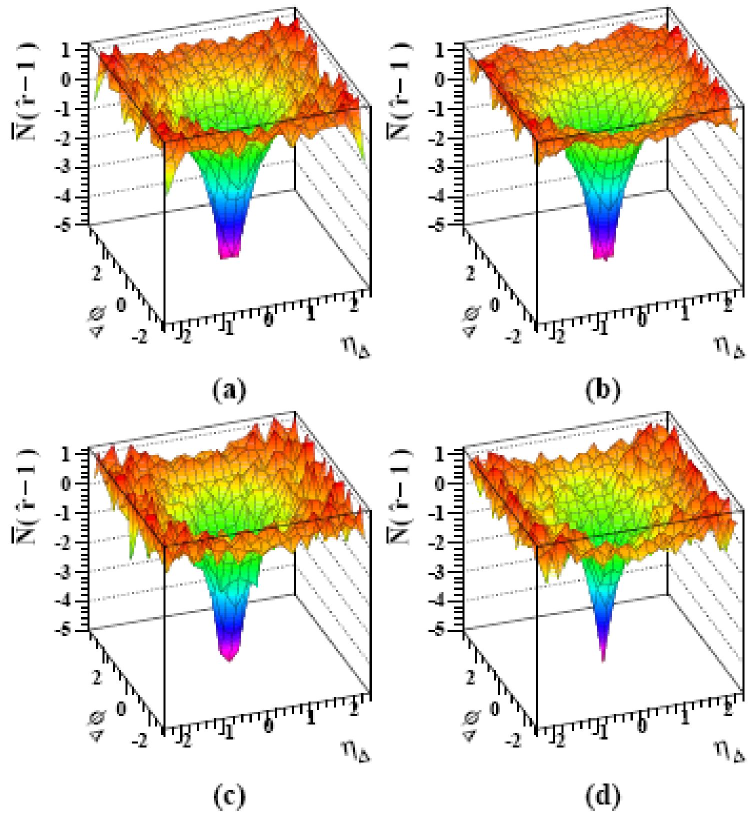

Figure 3.17: Charge-dependent axial correlations in 130 GeV Au+Au data from peripheral (d) to central (a) collisions. From [50].

with this picture, where correlated pairs become increasingly dissociated at larger opening angles.

The dramatic change in CD ϕ_Δ width from p+p to Au+Au corresponds to the absence of a longitudinal fragmentation signal in the CI correlations. This process is the primary mechanism for hadronization of soft particles, so what replaces this process in heavy ion collisions? No distinctly resolvable soft and hard components are apparent in the CD correlations. One possible scenario is that the soft component stops producing correlations, so then the structure is dominated

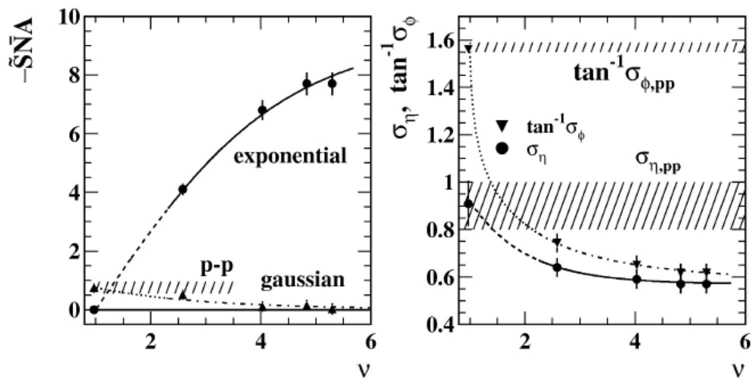

Figure 3.18: Fit parameters of amplitudes (left panel) and widths (right panel) for charge-dependent axial correlations.

by the hard component and soft particles are produced individually rather than in correlated pairs. Another scenario is that the structure of the soft component changes significantly to be more similar to the hard component. In that case soft particle hadronization along one dimensional longitudinal strings is replaced by two-dimensional hadronization along a surface. The detailed p_t dependence of the CD correlations would provide a method for distinguishing these models or alternative scenarios.

3.4.3 Two Component Spectra

The two component spectra analysis of p+p can be extended to heavy ion collisions [38]. Using the same assumptions that the soft component grows with $N_{part}/2$ while the hard component follows N_{bin}, we have

$$\frac{2}{N_{part}}\,\rho_{AA}(y_t;\nu) = S_{NN}(y_t) + \nu H_{AA}(y_t;\nu) \tag{3.14}$$

$$= S_{NN}(y_t) + \nu r_{AA}(y_t;\nu) H_{NN}(y_t) \tag{3.15}$$

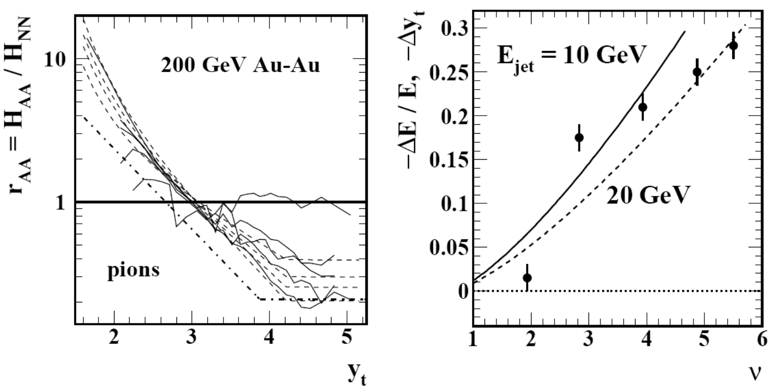

Figure 3.19: Left panel: Hard component ratio r_{AA} for pions (solid lines) compared to an energy loss model (dashed lines). Right panel: Measured energy loss Δy_t (points) and theoretical predictions (curves). From [38].

where $\rho_{AA} = (1/2\pi)\,(1/y_t)\,d^2n/dy_t\,d\eta$, S_{NN} and H_{NN} are the soft and hard references of a nucleon-nucleon collision (a generalization of the p+p limit), H_{AA} is the measured hard component of the heavy ion collisions, and $r_{AA} \equiv H_{AA}/H_{NN}$ gives a two component form of the typical nuclear modification factor R_{AA} [46]. In this model, the nucleon-nucleon soft component is unmodified in heavy ion collisions, thus in 3.14 S_{NN} is used instead of S_{AA}, though the amplitude grows. The hard component H_{AA} is written as a function of ν, so it is allowed to change in shape. The left panel of 3.19 shows the ratio r_{AA} using only particles identified as pions in 200 GeV Au+Au for five centralities. The most peripheral bin of 60-80% centrality follows unity, though all successive centrality bins show a significant drop at higher y_t. Incorporating this into an energy loss model a reduction in transverse rapidity Δy_t is observed representing a uniform fractional momentum reduction as shown in the dash-dot lines. The right panel of 3.19 compares the measured values of Δy_t, shown as solid points, to theoretical predictions of relative energy loss.

The striking feature is the apparent discontinuity between the first two points in contrast to theoretical models predicting a much smoother variation. This behavior is reminiscent of the large increase in η_Δ width of the minijet peak in figure 3.16. After subtracting a soft component which remains unmodified at all centralities, this analysis observes an increase in pion yield at small p_t related to the large p_t energy loss. This increase is manifested in the change in the hard component parameter x, jumping from 0.012 in p+p to 0.10 in Au+Au. The increasing x was also visible in figure 3.5 where the dash-dot line uses the p+p value of x, substantially underpredicting the Au+Au data.

The two component spectra and minimum-bias correlations together suggest interesting behavior in central Au+Au collisions. The hard spectra shows a deficit of high y_t pions with an excess at low y_t. In the same centrality range transverse correlations indicate minijet-medium interactions, while axial correlations show a huge increase in the amplitude and η_Δ width of the minijet peak. These results suggest that large momentum particles loose energy through some mechanism, producing a large number of low momentum particles distributed along a wide η range from the original semi-hard parton. The increased particle production causes the factor of eight increase in x from p+p to Au+Au collisions.

3.5 Fluctuation Inversion and Energy Dependence

3.5.1 Axial p_t Correlations

The minimum-bias correlations on the *number* of particle pairs in gold-gold collisions studied thus far have been dominated by minijet correlations. These results provide a basis for understanding the p_t correlations from fluctuation inversion shown above. Both number and p_t correlations can be expressed as covariances, of either number of pairs or a scalar p_t sum, between histogram bins compared to an appropriate reference. The covariances are then formed into Pearson correlations. A detailed discussion of these correlation measures is postponed to the next chapter.

Scale-dependent fluctuations on $\Delta\sigma^2_{p_t:n}$ with corresponding $\frac{\Delta\rho(p_t:n)}{\sqrt{\rho_{ref}(n)}}$ correlations [31] for 200 GeV Au+Au collisions at three centralities are shown in figure 3.20. Unlike the scale-dependent fluctuation surfaces in the left column, we have seen how the correlation structures (right column) can be directly interpreted in terms of physical processes. As in the number correlations (figure 3.14), the primary correlation structures are a same-side peak, a flat away-side peak modeled by a $\cos(\phi_\Delta)$ dipole, and a $\cos(2\phi_\Delta)$ quadrupole.

However, subtracting the dipole and quadrupole terms reveals two new features unique to p_t correlations. The away-side in figure 3.21 now shows a peak, and a negative structure surrounds the same-side peak. Since these new structures both show significant η_Δ dependence they cannot be the result of incorrectly subtracting the η_Δ *in*dependent dipole and quadrupole.

All three structures are fit with a function similar to a two dimensional Gaussian, except that the exponent (2 for a Gaussian) is also a fit parameter. The same-side positive minijet peak, which is narrow in ϕ_Δ, sits inside a negative Gaussian that is broad on ϕ_Δ. The fit parameters are plotted in figure 3.22. The left panel shows the Gaussian amplitudes for all three structures. The two new structures unique to p_t correlations are plotted as triangles and open circles. These structures are not present in the most peripheral centralities, but increase linearly after their respective onsets. All amplitudes deviate from the linear trends with a rapid drop at $\nu \sim 4.6$. The right panel gives the widths of the positive same-side peak. For $\nu < 2.8$ the η_Δ width is approximately constant while the ϕ_Δ decreases linearly. Both trends change behavior for $\nu > 2.8$, with σ_{η_Δ} increasing as σ_{ϕ_Δ} remains flat.

HIJING agrees well with the most peripheral bin except for overpredicting the η_Δ width of the minijet peak, which is observed to be highly asymmetric in the data. HIJING shows little change for other centralities while the data show substantial non-monotonic variation, and the two new structures which emerge are

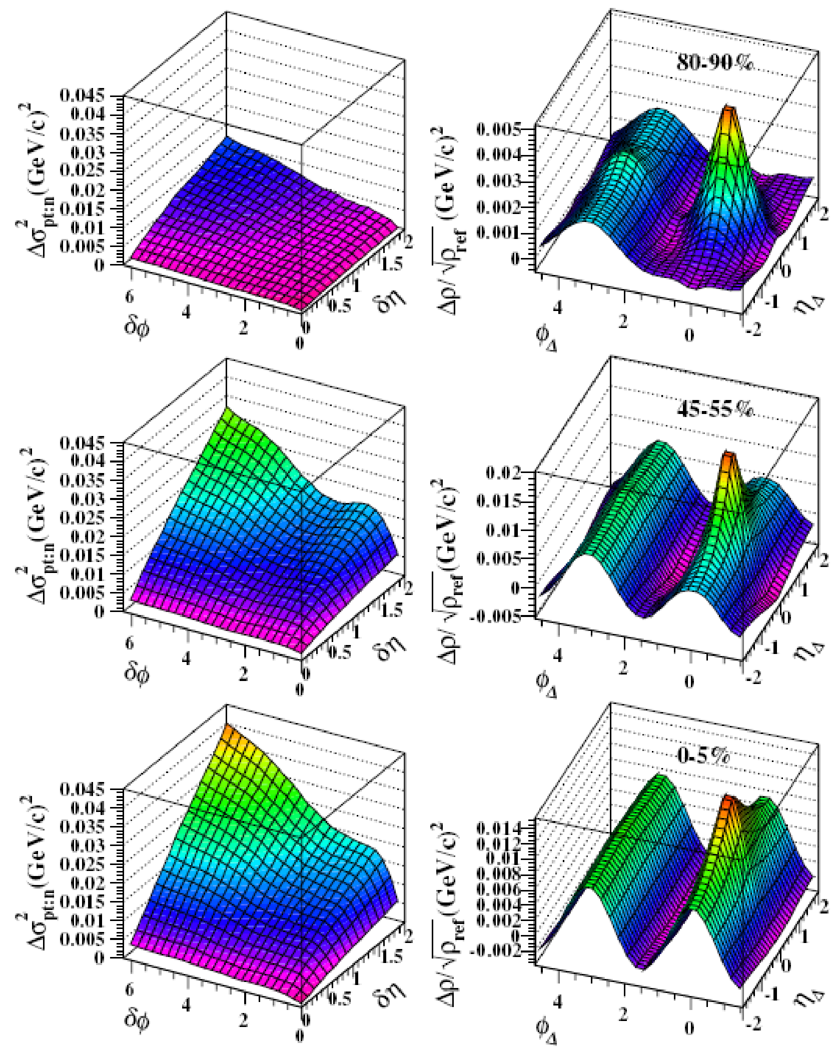

Figure 3.20: Scale-dependent p_t fluctuations (left column) and corresponding correlations (right column) from numerical inversion for 200 GeV Au+Au collisions for peripheral (top), mid-central (middle), and central (bottom) events. From [31].

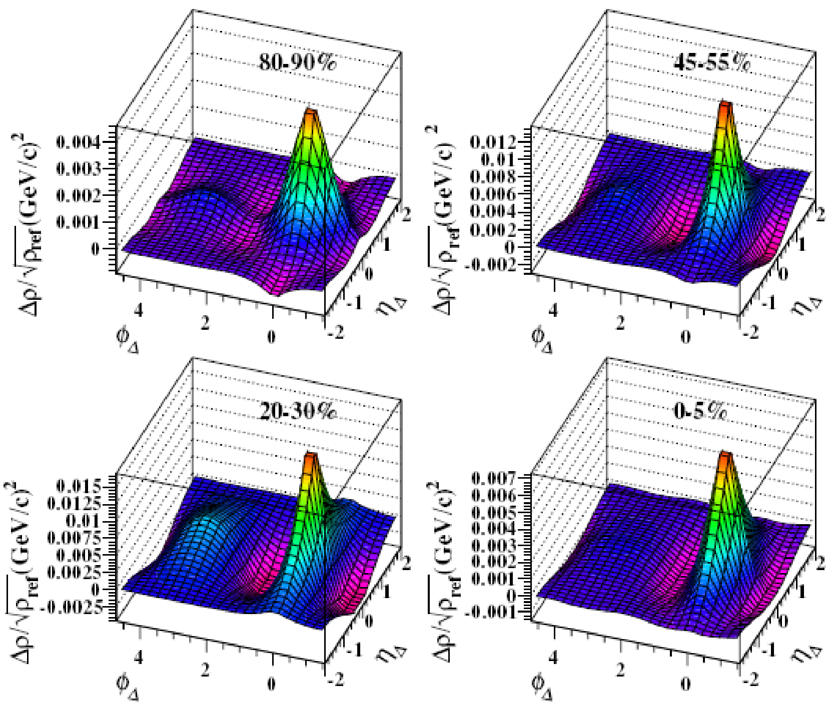

Figure 3.21: p_t correlations with dipole and quadrupole terms subtracted revealing new structures not seen in number correlations. From [31].

completely absent in the simulation. Another reference for comparison is the number correlations in figure 3.16. The minijet amplitude shows similar linear growth to $\nu \sim 4.6$ in both data sets, beyond that the p_t correlations fall off much more rapidly. The ϕ_Δ widths are quite comparable, but though the η_Δ widths have similar trends in number and p_t correlations, the magnitudes are quite different. The minijet η_Δ width increases by a factor of approximately 2.5 in number correlations, but only 1.6 in p_t correlations.

The two new features in p_t correlations demand further attention. Using the fit model, the minijet peak can be subtracted from the data as well as the multipole moments to isolate these structures (see the left panel of figure 3.23). Replotting

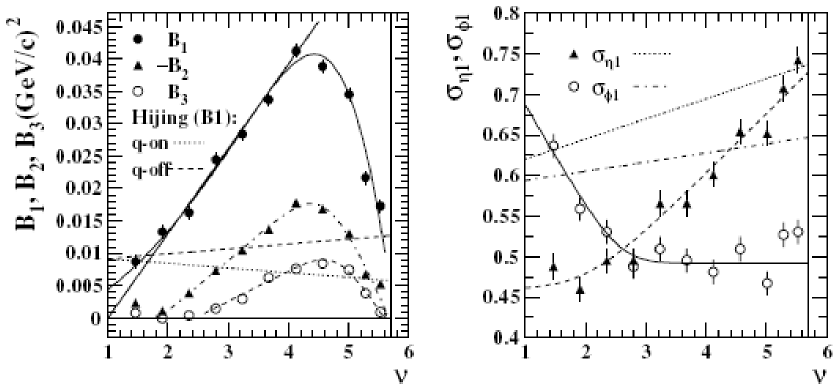

Figure 3.22: Fit parameters for the structures shown in figure 3.21 for 11 centrality bins. Left panel: Gaussian amplitudes for the same-side positive (solid circles), same-side negative (triangles), and away-side (open circles) peaks. Right panel: Gaussian widths of the same-side positive peak. In both panels the dashed lines show HIJING results for the same-side positive peak. From [31].

this histogram with cylindrical axes, shown in the right panel, suggests a physical interpretation. The relative covariances measured by p_t correlations are sensitive to the velocity distributions within an event. Any localized disturbance to these velocities could cause a Doppler shift. The correlations from hadrons produced during fragmentation of a semi-hard scattered parton are shown in the same-side minijet peak. However, that parton has partner moving in the opposite direction, and as it interacts with other particles it may cause a recoil in the medium on the same side as the minijet. In this picture, one scattered parton fragments sharing its momentum with hadrons which appear blue-shifted relative to the other particles, while the back-to-back parton causes a red shift from medium recoil. If only existing particles are being slowed down, then this mechanism would not be seen in the number correlations. An alternative interpretation of a negative p_t correlation is that new particles are being created with a p_t of less than $\hat{p_t}$. In this case a positive number correlation would be observed over the same angular range as the negative

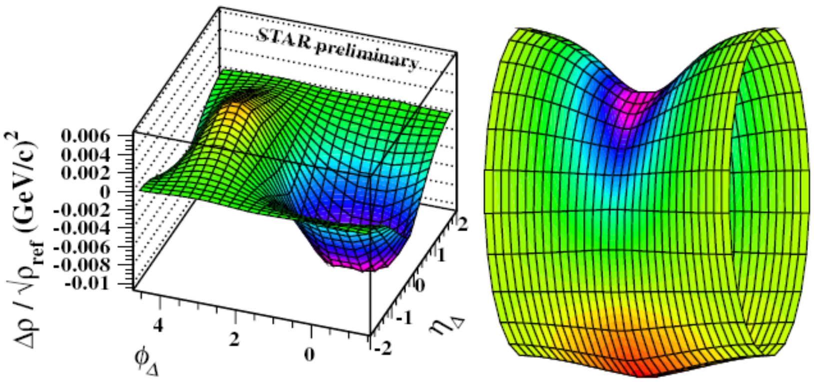

Figure 3.23: New features present only in p_t correlations plotted in the standard format (left panel) and with cylindrical axes (right panel). From [43].

p_t correlation.

3.5.2 Energy Dependence

The previous results have focused on the centrality dependence of correlations and fluctuations. The analysis in [51] examines the energy dependence as well. Fluctuation measure $\Delta\sigma_{p_t:n}$ is shown in the left panel of figure 3.24 for four RHIC energies: 19.6 GeV (open triangles), 62.4 GeV (closed triangles), 130 GeV (open circles), and 200 GeV (closed circles). The lower hatched region shows a range for fluctuations measured at SPS energies of 12.3 and 17.3 GeV extrapolated to full STAR acceptance. The peripheral collisions for $\nu < 2.5$ are barely distinguishable from 62 to 200 GeV, while the central collisions show a large energy dependence as well as non-monotonic variation with centrality.

These fluctuation results are directly related to the *integrals* of the correlation structures shown above. Recalling that the dominant correlation features are the multipole moments, which integrate to zero, and the same-side minijet peak, suggests that the non-statistical fluctuations are driven by minijets. The centrality

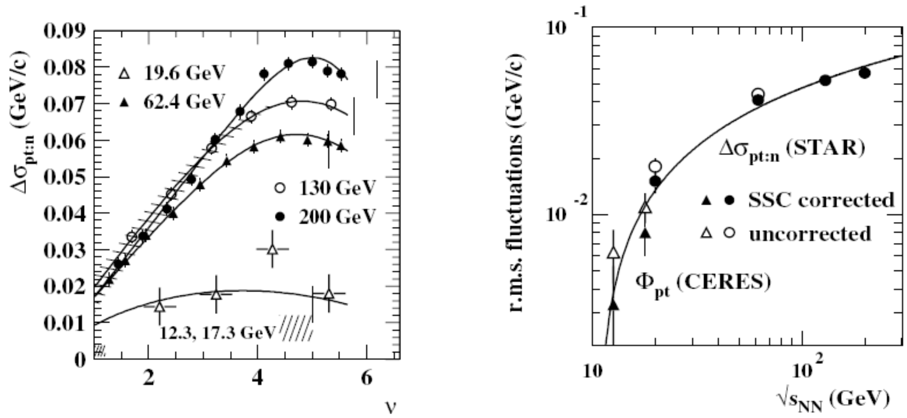

Figure 3.24: Left panel: centrality and energy dependence of fluctuations at RHIC and SPS. Right panel: fluctuations in central collisions following a log $\sqrt{s_{NN}}$ trend. From [51].

dependence of this figure as compared to the minijet peak amplitude in figure 3.22 illustrates this point [51]. The energy dependence is also telling. The theoretical expectation is that minijet production grows as the $\log(\sqrt{s_{NN}})$. Therefore, if the fluctuations are dominated by minijets, then they should also scale this way. The right panel of figure 3.24 shows the fluctuations for central collisions as a function of $\sqrt{s_{NN}}$. The CERES data have been extrapolated to full STAR acceptance. A background of small-scale correlations (SSC) is removed by subtracting the contribution from $\delta\eta < 0.2$. The solid curve is proportional to $\log(\sqrt{s_{NN}}/10.5)$. The excellent agreement has three implications. The first is extremely strong support of the minijet interpretation as the primary source of non-statistical fluctuations. The second implication, from extrapolating this curve to lower energies, is an onset of detectable minijet production near 10 GeV serving as a minimum threshold for observable parton scattering. A final implication is that the large gap between 19.6 and 62.4 GeV in the left panel of 3.24 is only a consequence of the $\log(\sqrt{s_{NN}})$ scaling, and not due to significantly different physics between these two energies.

3.6 Conclusion

While event-by-event fluctuations have failed to provide a smoking gun signal of a phase transition, significant non-statistical fluctuations have been found at RHIC, though their physical origin is largely unclear. Conventionally, two particle correlations have been extensively studied by applying data cuts and projections to minimize background, but when each correlation source is studied in isolation this procedure requires many assumptions and often incurs large systematic errors. The minimum-bias correlation analysis was developed to solve both of these problems. Correlations allow a differential study of fluctuations closely related to physical processes, while studying all correlation sources simultaneously provides maximal information to separate one source from another, while also revealing any previously unexpected correlations.

The results discussed above have independently shown the large role that minijets play in heavy ion collisions as sources of non-statistical fluctuations, components in single particle spectra, and the dominant feature in axial and transverse correlations. Some theoretical estimates predict that 50% of transverse energy at RHIC will be produced by minijets, increasing to 80% at the LHC [37]. If understanding minijets is important to heavy ion physics now, then it will be absolutely essential at higher energies in the future. The overall abundance of minijets and their prevalence in the final state directly addresses the degree of thermalization of RHIC collisions, a fundamental question since thermalization is viewed as a necessary condition for a well-defined state of matter [25]. Beyond minijets, these analyses provide insight into many other sources of correlations and interactions with the dense and energetic QCD environment of heavy ion collisions.

Single particle spectra and p_t correlations are well-studied, while the correspondence to number correlations is tantalizing but incomplete. The limited p_t range and centrality dependence of number correlations at 130 GeV suggest very different minijet behavior from p_t correlations as well as structures unique to each analysis. The energy dependence of number and p_t correlations was not studied.

This suggestive though incomplete picture motivates my dissertation research of the detailed energy and centrality dependence of number correlations in Au+Au collisions. Open questions addressed by this analysis include:

- What correlation sources are observable at RHIC?
- What happens in the transition from nucleon-nucleon to heavy ion collisions?
- What happens to minijet correlations in Au+Au collisions?
- Spectra and p_t correlations suggest a centrality dependent point where minijets behave differently than expected from p+p at 200 GeV. Is this observable in number correlations? Is the centrality point the same at 62 GeV?
- What happens to longitudinal fragmentation?
- How do the quadrupole measurements correspond to conventional elliptic flow studies?
- Do the transverse correlations relate to the two component y_t spectra analysis?
- Do the axial or transverse correlations provide any evidence for or against thermalization?

The technical details and results of this analysis are presented in the following chapters.

Chapter 4

Formalism

4.1 Introduction

We treat kinematic quantities of particles and particle pairs, summed by grouping into histogram bins, as random variables sampling an unknown parent distribution. The outcome of any one sample, particles detected in a single collision event, is random and thus unpredictable. Through statistical analysis of a large number of events we can infer properties of the parent distribution.

4.1.1 Correlations

For a set of N data points x_i with $i \in [1, N]$, the distribution is described by the mean

$$\bar{x} = \frac{1}{N}\sum_{i=1}^{N} x_i \tag{4.1}$$

and the variance

$$\sigma_x^2 = \frac{1}{N}\sum_{i=1}^{N}(x_i - \bar{x})^2. \tag{4.2}$$

The relationship between two data sets x_i and y_i, or between the variables in a two-dimensional distribution (x_i, y_i) is measured with a covariance

$$Cov(x,y) = \frac{1}{N}\sum_{i=1}^{N}(x_i - \bar{x})(y_i - \bar{y}) \tag{4.3}$$

which reduces trivially to the variance in the case of $y = x$. The covariance can be normalized to form a correlation

$$\begin{aligned} R_{xy} &= \frac{Cov(x,y)}{\sigma_x \sigma_y} && (4.4) \\ &= \frac{\sum_{i=1}^{N}(x_i - \bar{x})(y_i - \bar{y})}{\left[\sum_{i=1}^{N}(x_i - \bar{x})^2 \sum_{i=1}^{N}(y_i - \bar{y})^2\right]^{1/2}} && (4.5) \end{aligned}$$

known as Pearson's product-moment correlation coefficient, named after the founder of mathematical statistics Karl Pearson (1857-1936). By substituting $y_i = \pm x_i$, it is easily shown that R ranges from $+1$ for perfectly correlated data to -1 for anti-correlated data. Figure 4.1 shows examples for 100 data points that are uncorrelated (top left), partially correlated (top right), strongly anti-correlated (bottom left), and perfectly correlated (bottom right).

4.1.2 Autocorrelations

It is not necessary for x and y to be separate data sets, but is it meaningful to correlate a distribution with itself? There may be correlations within a one-dimensional distribution. Consider a time series example where x_i is some value measured at time step i. Let $y_i = x_{i+1}$, then R measures the correlation within the same time series lagged by one unit of time, or more simply the degree of relationship between one point and the next averaged over all points. Now generalize to an arbitrary lag

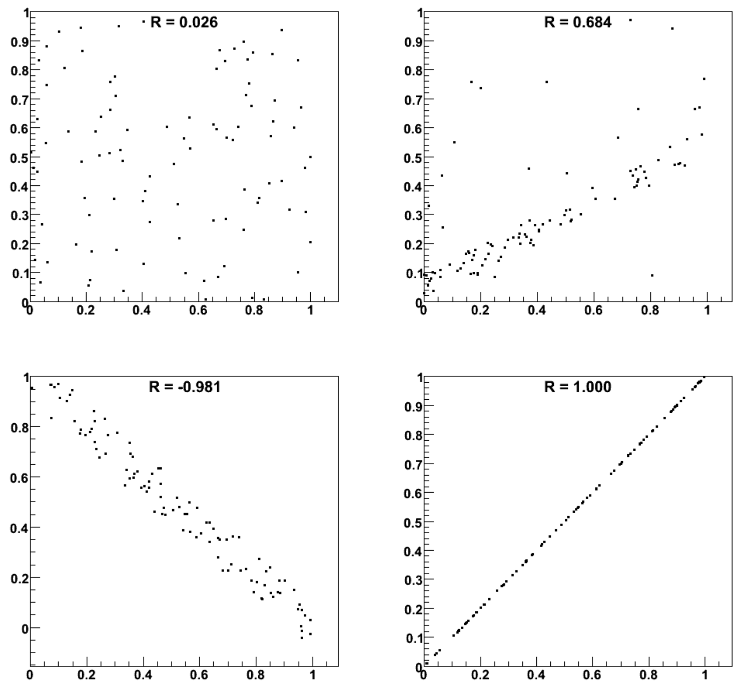

Figure 4.1: Examples of data sets with various degrees of correlation.

of k time units as $y_i = x_{i+k}$, then applying 4.5 gives

$$R_k = \frac{\sum_{i=1}^{N-k}(x_i - \bar{x})(x_{i+k} - \bar{x})}{\sum_{i=1}^{N-k}(x_i - \bar{x})^2} \tag{4.6}$$

Note that this definition requires a *stationary* distribution where features such as the mean and the variance do not depend on location in the time series so are unaffected by the offset k, otherwise a more complicated expression is needed. Equation 4.6 is an example of an autocorrelation, named using the Greek root *auto* meaning "self".

In signal processing, an unnormalized form of 4.6 is often used for the autocorrelation. By not subtracting the mean or dividing by the variances, a simplified autocorrelation is constructed sufficient for determining relative strengths of periodic features, though not absolute correlation magnitudes. One often finds autocorrelations defined for these applications as:

$$R(\tau) = \frac{1}{T}\int_0^T f(t+\tau)f(t)dt \quad (4.7)$$

$$R_k = \sum_{i=0}^{N-k} x_i x_{i+k} \quad (4.8)$$

The top line gives the continuous form averaged over a period T. The bottom line is discrete, and for periodic structures the upper bound on i may be increased to $N-1$ with the final subscript taken modulo N.

The autocorrelation has a long pedigree including contributions from prominent scientists including Einstein, Langevin, Levy, Wiener, and many others. A brief history is given in appendix A of [52] and references therein. The concept of an autocorrelation was introduced by Einstein in 1905 to provide a statistical description of Brownian motion [52, 53]:

> "Another important consideration can be related to this method of development. We have assumed that the single particles are all referred to the same co-ordinate system. But this is unnecessary, since the movements of the single particles are mutually independent. We will now refer the motion of each particle to a co-ordinate system whose origin coincides at the [arbitrary] time t = 0 with the [arbitrary] position of the center of gravity of the particle in question."

He went on to specify a function satisfying the diffusion equation as a probability distribution on relative displacement over a time period. This advance lead to a new analysis tool now commonly used in many diverse fields.

Figure 4.2 shows a simple example of a time series autocorrelation. For the i^{th} time step

$$x_i = Random[-1,1] + \epsilon \sin(i2\pi/10).$$

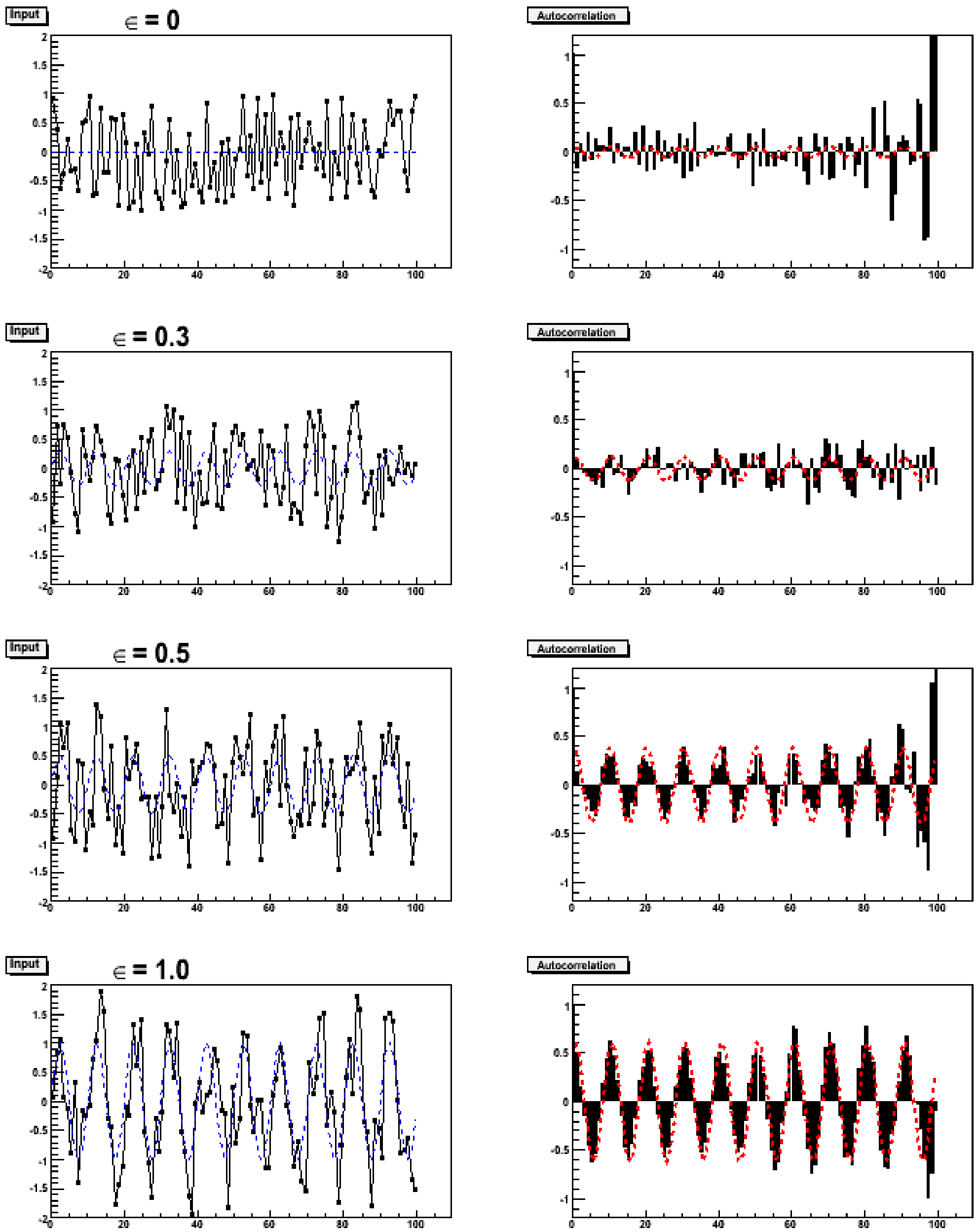

Figure 4.2: Autocorrelations in a time series.

Setting $\epsilon = 0$ gives uncorrelated noise, and increasing ϵ builds a periodic correlation into the data. The left column shows the generated time series with the $\epsilon \sin$ contribution overlayed in a dashed blue line. The right column gives the autocorrelation R_k with a sinusoid fit superimposed. As one might expect, these plots show that an autocorrelation of a periodic structure also has the same period. This example illustrates how autocorrelations reveal trends in the data, even when these trends are buried under random noise.

4.2 Application

The correlation and autocorrelation are directly applicable to physics at RHIC. A certain subset of particles produced in a single ion-ion collision will be detected with some finite resolution. Suppose we construct a histogram with the number of particles n detected in each event binned as function of an arbitrary quantity x. We do this many times, keeping separate histograms for each event, and define $n_i(a)$ as the particle count in bin a for event i. Note that roman indices a and b will always be used to reference histogram bins. We can measure the correlation between any two histogram bins a and b averaged over all N events to see if detecting a particle in one bin at some $x = a$ makes finding a particle with $x = b$ more or less likely. Using this notation, the analogue to the correlation definition in 4.5 is

$$\begin{aligned} R_{ab} &= \frac{1}{N}\sum_{i=1}^{N}\left[n_i(a) - \overline{n(a)}\right]\left[n_i(b) - \overline{n(b)}\right]/\sigma_a\sigma_b && (4.9) \\ &= \overline{(n-\bar{n})_a\,(n-\bar{n})_b}/\sigma_a\sigma_b && (4.10) \end{aligned}$$

using a less cumbersome notation in the second line with an overbar to represent an event average and bin indices as subscripts.

We can also define an autocorrelation among these histogram bins by measuring correlations as a function of relative displacement. This tests the relationship between $n(x)$ in bin a and $n(x+\Delta x)$ in bin $a+k$ as a function of Δx averaged over x; *i.e.* if we embed a test particle into an event how will particles be distributed around it on average. The histogram version of the time series autocorrelation from 4.6 is then

$$R_k = \frac{1}{x_{max}-k}\sum_{a=1}^{x_{max}-k}\overline{(n-\bar{n})_a\,(n-\bar{n})_{a+k}}/\sigma_a\sigma_{a+k} \tag{4.11}$$

4.2.1 Pair Analysis

Correlations between histogram bins only approximate the two-particle correlation, which is the stated goal of this analysis. Histograms are convenient to deal with, but a great deal of information is lost in the binning process. In the equation above, difference Δx is approximated as the distance between bin centers, but depending on where particles fall within their respective bins the difference may be shifted by one bin from the actual pair Δx. Difficulties in resolving two nearby tracks cause pair-wise tracking inefficiencies not easily corrected in a pre-binned distribution. Finally, in using single particle histograms the ability to distinguish pair-wise quantities is lost; *e.g.* separating the correlations of same-side versus away-side pairs. Therefore, to measure two-particle correlations we will not consider a pre-binned *single*-particle histogram, but instead individual particle *pairs*.

The covariance can be suggestively expanded to re-express correlations in terms of particle pairs:

$$\overline{(n-\bar{n})_a\,(n-\bar{n})_b} = \overline{n_a n_b} - \bar{n}_a\bar{n}_b. \tag{4.12}$$

For a two dimensional histogram of particle pairs, $\overline{n_a n_b}$ is the event-wise averaged total number of pairs in bin (a,b), and the product $\bar{n}_a\bar{n}_b$ is the statistical reference of the expectation when a and b are uncorrelated. Both quantities can be measured experimentally. The particles within a given event can be combined to form all possible pairs, and the distribution of these pairs is measured with a two dimensional histogram for the first term of 4.12. These are referred to as *sibling* pairs. The second term is found by forming pairs where each particle comes from a different event, thus measuring uncorrelated *reference* pairs.

Figure 4.3 illustrates the relationships between single-particle and pair histograms [54]. The left panel shows a single-particle histogram measuring a distribution at bins a and b. The middle panel shows the corresponding two dimensional pair histogram. Points along the main diagonal at bins (a, a) and (b, b) measure variances σ_a^2 and σ_b^2, while the off-diagonal represents covariance between a and b. The right panel illustrates such a covariance plotted as deviation from the mean on $n_a - \bar{n}_a$ and $n_b - \bar{n}_b$. The dashed circle represents no correlation between a and b, while the ellipses show correlation and anti-correlation. This histogram can be projected onto an axis to recover the single-particle distribution.

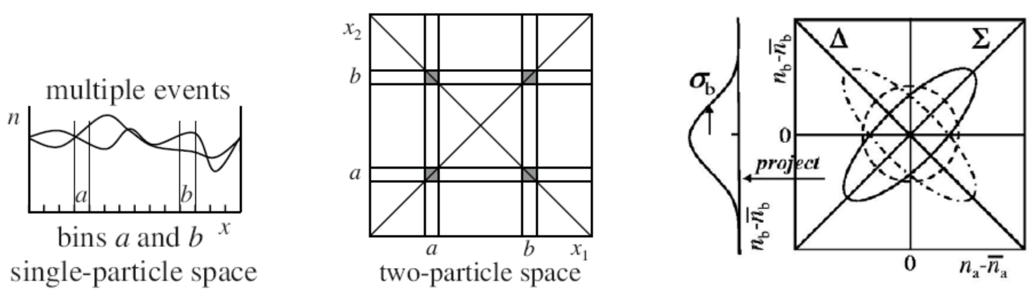

Figure 4.3: Distributions in a single-particle histogram (left panel), and two dimensional pair histogram (middle). The covariance (right) can be seen as deviations from the mean [54].

The equivalence between the formalism of single-particle bins and particle pairs for sibling and mixed events can be shown defining $n_{i,a}$ as the number of particles in bin a for event i with ε total events:

$$Cov(a, b) \quad = \quad \overline{n_a n_b} - \bar{n}_a \bar{n}_b$$

$$
\begin{aligned}
&= \overline{n_a n_b} - \frac{1}{\varepsilon^2}\sum_{i=1}^{\varepsilon}\sum_{j=1}^{\varepsilon} n_{i,a}n_{j,b} \\
&= \overline{n_a n_b} - \frac{\varepsilon(\varepsilon-1)}{\varepsilon^2}\frac{1}{\varepsilon(\varepsilon-1)}\sum_{i=1}^{\varepsilon}\sum_{j=1,j\neq i}^{\varepsilon} n_{i,a}n_{j,b} - \frac{1}{\varepsilon^2}\sum_{i=1}^{\varepsilon} n_{i,a}n_{i,b} \\
&= (1-\frac{1}{\varepsilon})\overline{n_a n_b} - \frac{\varepsilon-1}{\varepsilon}\frac{1}{\varepsilon(\varepsilon-1)}\sum_{i=1}^{\varepsilon}\sum_{j=1,j\neq i}^{\varepsilon} n_{i,a}n_{j,b} \\
&= \frac{\varepsilon-1}{\varepsilon}\left[\overline{n_a n_b} - \frac{1}{\varepsilon(\varepsilon-1)}\sum_{i=1}^{\varepsilon}\sum_{j=1,j\neq i}^{\varepsilon-1} n_{i,a}n_{j,b}\right] \\
&= \frac{\varepsilon-1}{\varepsilon}\left[\overline{n_a n_b} - \bar{n}_a\bar{n}_{b,mixed}\right]. \qquad (4.13)
\end{aligned}
$$

In the first line, $\bar{n}_a\bar{n}_b$ is an inclusive mean taken over all events. The $\bar{n}_a\bar{n}_{b,mixed}$ term in the last line, emphasized by the subscript *mixed*, is a product taken for pairs of different events as set by the $i \neq j$ requirement in the double sum. Ratio $\frac{\epsilon-1}{\epsilon}$ approaches unity for a large number of events.

The covariance is easily expressed with particle pairs, though the denominator in 4.5 is more challenging. In this application, we are measuring the discrete number of particles arriving at a given detector volume within a small amount of time. Particle detection can be approximately modeled as a Poisson process, though particle correlations cause deviations from this model. The number of particles detected then approximately follows a Poisson distribution $f(k;\lambda) = \lambda^k e^{-\lambda}/k!$ for the probability of detecting k particles when the expectation is λ. This distribution has both a mean and variance of λ. Thus we can approximate the denominator in the correlation definition as $\sigma_a\sigma_b \approx \sqrt{\bar{n}_a\bar{n}_b}$, the square root of the number of mixed-event reference pairs in bin (a,b).

Forming the pair autocorrelation can be accomplished in one of two ways. First, following the definition in 4.11 the autocorrelation R_k is found by averaging along the k^{th} diagonal of the pair histogram [54], as shown in the left panel of figure 4.4. Note that this histogram is formed by considering all possible particle pairs and is symmetric by construction. Another approach is to directly bin the histogram on the difference variable $x_\Delta \equiv x_1 - x_2$ as in the right panel. As noted in the figure, the main diagonal represents the sum $x_\Sigma \equiv x_1 + x_2$. This x_Δ, x_Σ notation has been adopted since the reverse Δx is already over-subscribed and often refers to the separation between a high p_t trigger and associated particle, while Σx is easily mistaken in formulae for summation.

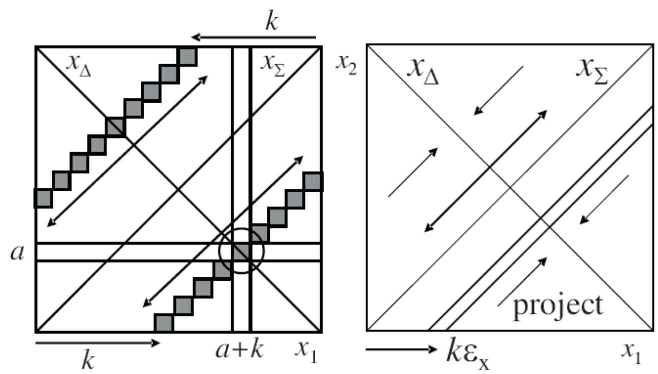

Figure 4.4: Forming a two-particle autocorrelation by averaging along the k^{th} diagonal (left panel) or binning directly on a difference variable (right) [54].

4.3 Constructing the Correlation Measure

Defining event-averaged sibling pair density ρ_{sib} with mixed-event reference density ρ_{ref}, the covariance in 4.13 can be written as the difference $\Delta\rho \equiv \rho_{sib} - \rho_{ref}$. This motivates the notation of the correlation measure introduced in the previous chapter and defined here as:

$$\frac{\Delta\rho}{\sqrt{\rho_{ref}}} = \frac{\overline{(n-\bar{n})_a\,(n-\bar{n})_b}}{\sqrt{\bar{n}_a \bar{n}_b}}. \tag{4.14}$$

Consider that ρ_{sib} contains correlated and uncorrelated pairs, then $\Delta\rho \propto$ *correlated pairs*. Since ρ_{ref} goes as the number of uncorrelated pairs, $\sqrt{\rho_{ref}} \propto$

particles, as evident in 4.14. Then $\frac{\Delta\rho}{\sqrt{\rho_{ref}}} \propto$ *correlated pairs per particle.*

The mixed-event references pairs present both an opportunity and a challenge to this correlation measure. Mixed pair density ρ_{ref} measures uncorrelated pairs as detected by STAR, so this distribution contains experimental artifacts such as incomplete acceptance, inefficiencies, and track loss during reconstruction. Sibling pair density ρ_{sib} contains all of these in addition to the correlated pairs and two-track inefficiencies. We can use the information in ρ_{ref} to remove these backgrounds from the correlation by forming the ratio $r = \rho_{sib}/\rho_{ref}$. This ratio motivated the correlation measure used in the 130 GeV analysis [48, 50, 47]. Then

$$\frac{\Delta\rho}{\sqrt{\rho_{ref}}} = \sqrt{\rho_{ref}}\frac{\Delta\rho}{\rho_{ref}} = \sqrt{\rho_{ref}}(r-1),$$

and the detector acceptance and inefficiencies removed in the ratio r are reintroduced in the factor $\sqrt{\rho_{ref}}$. Thus we must replace this factor by defining an idealized $\sqrt{\rho'_{ref}}$ that has been corrected for experimental artifacts.

As explained in the previous chapter, we visualize the six dimensional two-particle correlation space by separating a transverse (y_{t1}, y_{t2}) correlation and an axial $(\eta_\Delta, \phi_\Delta)$ autocorrelation, though other projections are possible. For correlations, ρ'_{ref} is most readily constructed by applying corrections for the single-particle efficiencies. In general, this spectra correction may be transformed for use in an autocorrelation, however there is a simpler approximation for axial autocorrelations at mid-rapidity. By assuming azimuthal symmetry and longitudinal boost invariance an ideal axial ρ'_{ref} can be formed using $\frac{dn}{d\eta}$ at $\eta = 0$ (see section 4.4.1).

We will construct the correlation measure around this ratio r. To maximize the efficiency in removing experimental artifacts it is necessary to ensure that all events included in the average pair densities have similar structure, otherwise cancellation may not occur in the ratio. To this end, we must analyze events only within a small multiplicity range Δn and primary z-vertex location Δz within the detector, take the sibling to mixed ratio, then combine these ratios across all Δn (within a certain centrality) and Δz with a weighted average. Ultimately we will differentiate by pair charge type as well.

Combining all of these considerations, first all events are analyzed to construct pair densities ρ_{sib} by forming particles into all possible pairs. These are histogrammed as number of pairs per bin $N_\alpha^{sib}(a,b)$ for bin (a,b) where α indexes a $\Delta n, \Delta z$ event class. Note that lower-case n is used for particles, while capital N represents pairs. We take the average for all events and divide by bin widths ϵ (one factor for each dimension of the histogram) to form a density as average number of pairs per event per unit area

$$\rho_\alpha(a,b) \quad = \quad \frac{1}{\epsilon}\bar{N}_\alpha(a,b) \tag{4.15}$$

for sibling and reference pairs (the sib and ref superscripts will only be used when necessary), though forming pairs by taking particles from different events within the same event class α. Experimental artifacts are removed in the ratio

$$r_\alpha(a,b) = \rho_\alpha^{sib}(a,b)/\rho_\alpha^{ref}(a,b). \tag{4.16}$$

Event classes are combined using a weighted average based on total sibling pair count $N_\alpha^{sib} = \sum_{a,b} \bar{N}_\alpha^{sib}(a,b)$ in ratio

$$r(a,b) = \frac{\sum_\alpha N_\alpha^{sib} r_\alpha(a,b)}{\sum_\alpha N_\alpha^{sib}}. \tag{4.17}$$

The final correlation is formed using prefactor ρ'_{ref} as

$$\frac{\Delta\rho}{\sqrt{\rho_{ref}}}(a,b) \quad = \quad \sqrt{\rho'_{ref}}\,[r(a,b)-1] \tag{4.18}$$

recalling that $r - 1 \equiv \Delta\rho/\rho$ and noting that bin index (a,b) is typically either a function of (y_{t1}, y_{t2}) for transverse correlations or $(\eta_\Delta, \phi_\Delta)$ for axial autocorrelations.

4.4 Charge Dependence

The above procedure can be extended to differentiate by (electric) charge sign; *i.e.* distinguish between the $++$, $+-$, $-+$, and $--$ pairs. For unidentified particles, the $+-$ and $-+$ pairs are identical, but in a PID analysis $\pi^+K^- \neq \pi^-K^+$. We add charge indices qq' where q and q' are either $+$ or $-$ to obtain

$$\rho_{qq',\alpha}(a,b) = \frac{1}{\epsilon}\bar{N}_{qq',\alpha}(a,b) \tag{4.19}$$

and similarly for mixed events. The α will be dropped for the remainder of the section to simplify the notation, and the ratio averaging procedure in 4.17 will be assumed and not explicitly shown. Finally, to accommodate a special charge-dependent case we must express ratios in terms of $\Delta\rho/\rho_{ref}$ instead of $(r-1)$ as was done previously.

These pair densities are combined into like-sign (LS), unlike-sign (US), charge-independent (CI), and charge-dependent (CD) forms

$$\rho_{LS} = \rho_{++} + \rho_{--} \tag{4.20}$$

$$\rho_{US} = \rho_{+-} + \rho_{-+} \tag{4.21}$$

$$\rho_{CI} = \rho_{LS} + \rho_{US} \tag{4.22}$$

$$\rho_{CD} = \rho_{LS} - \rho_{US} \tag{4.23}$$

with differences

$$\Delta\rho = \rho_{sib} - \rho_{ref} \tag{4.24}$$

for all charge types. The choice of sign in the charge-dependent definition is motivated by pair counting arguments. Let n_+ be the number of positively charged particles in an event, and n_- the number of negative particles. Then the number of CI pairs is $(n_+ + n_-)^2 = (n_+n_+ + n_-n_-) + (2n_+n_-) =$ LS + US. The charge-dependent case is related to the event's net charge $(n_+ - n_-)$. The CD pairs go as $(n_+ - n_-)^2 = (n_+n_+ + n_-n_-) - (2n_+n_-) =$ LS - US.

The ratio $\Delta\rho/\rho_{ref}$ using the above equations is straightforward for LS and US pairs. Note that the CI ratio, equivalent to 4.16 above for all charges, is a *ratio-of-sums* form where division occurs after the charge types have been added and subtracted. Note that this ratio is still subject to the sibling pair weighted averages in 4.17. Maintaining the correspondence to an analysis that does not distinguish charge signs motivates this definition, which differs from the *sum-of-ratios* form $r_{CI} = r_{LS} + r_{US}$ in the 130 GeV analysis [48] by approximately a factor of $\sqrt{2}$ (by assuming $\rho_{LS}^{ref} \approx \rho_{US}^{ref}$).

The CD ratio must be defined as a special case since the definition of ρ_{CD} in 4.23 is not consistent with the denominator of the ratio as the variance of a Poisson distribution which must contain the sum of all charges. Therefore we define

$$\left.\frac{\Delta\rho}{\rho_{ref}}\right|_{CD} = \frac{(\rho_{LS}^{sib} - \rho_{LS}^{ref}) - (\rho_{US}^{sib} - \rho_{US}^{ref})}{\rho_{LS}^{ref} + \rho_{US}^{ref}} \tag{4.25}$$

$$= \frac{\Delta\rho_{CD}}{\rho_{CI}^{ref}} \tag{4.26}$$

This form also differs from the *sum-of-ratios* form in the 130 GeV analysis [50].

4.4.1 Detector Efficiency and Prefactor Corrections

A more realistic detector model may be used to study the effect of tracking inefficiencies and backgrounds. Defining tracking efficiency ε as the probability that a produced particle will be detected and b as the background fraction, in general the measured number of particles is

$$n = \varepsilon n^{true}(1+b) \tag{4.27}$$

The total measured number of mixed event *pairs* in ρ_{ref} is

$$N_{ref} = \varepsilon^2 N_{chrg}^{true}(1+b)^2 \tag{4.28}$$

for N^{true} pairs produced from all charged particles. The background particles may or may not be correlated, effecting the number of correlated pairs N_{corr} measured by $\Delta\rho$. We model this as

$$N_{corr} = \varepsilon^2 N_{corr}^{true}(1+b)^k \tag{4.29}$$

where $k = 0$ corresponds to uncorrelated background with $k = 2$ for a fully correlated background. In the 130 GeV analysis it was conservatively assumed that $k = 1 \pm 1$ to estimate a mean and systematic uncertainty due to the correlation content of background tracks. In that earlier analysis the measured correlation is

$$\frac{\Delta\rho}{\sqrt{\rho_{ref}}} = \frac{\varepsilon^2 N_{corr}^{true}(1+b)^{1\pm1}}{\varepsilon N_{chrg}^{true}(1+b)} \tag{4.30}$$

$$= \varepsilon(1+b)^{0\pm1}\left[\frac{\Delta\rho}{\sqrt{\rho_{ref}}}\right]_{true} \tag{4.31}$$

Defining the correction factor S as the ratio of true over uncorrected $\frac{\Delta\rho}{\sqrt{\rho_{ref}}}$, equation 4.31 gives

$$S_{130} = \frac{1}{\varepsilon} \tag{4.32}$$

$$= (1+b)\frac{n^{true}}{n} \tag{4.33}$$

using equation 4.27 in the last line. The 130 subscript emphasizes that this estimate was used in the 130 GeV analysis.

In the current analysis, the estimate of k of revisited to potentially reduce uncertainty. By varying track selection criteria such as the distance of closest approach parameter discussed in the next chapter, the background fraction was adjusted. The results showed little difference in the final correlation implying that the background is correlated along with the primary particles and that k is approximately 2. Then

$$\begin{aligned} S &= \frac{1}{\varepsilon(1+b)} \qquad (4.34) \\ &= n^{true}/n \qquad (4.35) \end{aligned}$$

In the present formalism, the correction factor S is included in the definition of prefactor $\sqrt{\rho'_{ref}}$ which is constructed to be free from experimental artifacts (see section 4.3).

For a transverse analysis it is generally most convenient to scale the measured particles by the efficiency correction in S. Since the two particles in the mixed event pair are uncorrelated, ρ_{ref} can be factored into a product of two single-particle distributions.

$$\rho_{ref}(y_{t1}, y_{t2}) = \frac{d^2N}{dy_{t1}dy_{t2}} = \frac{d\mathrm{n}}{dy_{t1}}\frac{d\mathrm{n}}{dy_{t2}}. \qquad (4.36)$$

It is most straightforward to find ρ'_{ref} by estimating the tracking efficiency $\varepsilon(y_t)$ and correcting the measured pair distribution

$$\rho'_{ref}(y_{t1}, y_{t2}) = \rho_{ref}(y_{t1}, y_{t2})/\varepsilon(y_{t1})\varepsilon(y_{t2}) \qquad (4.37)$$

In an axial analysis, the autocorrelation may be formed by averaging the single-particle distributions over η_Σ and ϕ_Σ (as in figure 4.4, left panel)

$$\rho_{ref}(\eta_\Delta, \phi_\Delta) = \frac{\int_{\Omega(\eta_\Delta)} d\eta_\Sigma \int_{\Omega(\phi_\Delta)} d\phi_\Sigma \frac{d^2 n_1}{d\eta_1 d\phi_1} \frac{d^2 n_2}{d\eta_2 d\phi_2}}{\int_{\Omega(\eta_\Delta)} d\eta_\Sigma \int_{\Omega(\phi_\Delta)} d\phi_\Sigma} \tag{4.38}$$

where $\Omega(x_\Delta)$ represents the integration limits along the x_Σ axes. We can factorize $\frac{d^2n}{d\eta d\phi} = \frac{\mathrm{dn}}{d\eta}\frac{\mathrm{dn}}{d\phi}$ and examine each component. The measured $\frac{\mathrm{dn}}{d\eta}$ distributions by PHOBOS at 62 GeV [55] and 200 GeV [56] and STAR at 200 GeV [57] are uniform from $|\eta| < 1$ within a few percent, thus may be approximated with a constant $\left.\frac{\mathrm{dn}}{d\eta}\right|_{\eta=0}$. Assuming azimuthal symmetry (when averaged over many events) gives $\frac{\mathrm{dn}}{d\phi} = \frac{1}{2\pi}$. Therefore, within the STAR TPC we may approximate the distributions $\frac{d^2n}{d\eta d\phi}$ in 4.38 by constants $\frac{1}{2\pi}\left.\frac{\mathrm{dn}}{d\eta}\right|_{\eta=0}$, making the integration trivial. Then

$$\sqrt{\rho'_{ref}(\eta_\Delta, \phi_\Delta)} \approx \frac{1}{2\pi}\sqrt{\left.\frac{\mathrm{dn}_1}{d\eta_1}\right|_{\eta_1=0} \left.\frac{\mathrm{dn}_2}{d\eta_2}\right|_{\eta_2=0}} \tag{4.39}$$

where n_1 and n_2 may represent different charge types or particle species in a PID analysis. Listing the charge combinations explicitly, we now have:

$$\sqrt{\rho^{ref'}_{LS}} = \sqrt{\rho^{ref}_{++} + \rho^{ref}_{--}} = \frac{1}{2\pi}\sqrt{\left(\frac{\mathrm{dn}_+}{d\eta}\right)^2 + \left(\frac{\mathrm{dn}_-}{d\eta}\right)^2} \tag{4.40}$$

$$\sqrt{\rho^{ref'}_{US}} = \sqrt{\rho^{ref}_{+-} + \rho^{ref}_{-+}} = \frac{\sqrt{2}}{2\pi}\sqrt{\frac{\mathrm{dn}_+}{d\eta}\frac{\mathrm{dn}_-}{d\eta}} \tag{4.41}$$

$$\sqrt{\rho^{ref'}_{CI/CD}} = \sqrt{\rho^{ref}_{++} + \rho^{ref}_{+-} + \rho^{ref}_{-+} + \rho^{ref}_{--}} = \frac{1}{2\pi}\frac{\mathrm{dn}_{ch}}{d\eta} \tag{4.42}$$

4.4.2 Correlations Summary

To summarize, the final correlations are formed by combining the eight pair density histograms (four charge types each for sibling and mixed events) with the appropriate prefactor. The analysis proceeds as follows. First, the eight pair density histograms are measured by forming all possible unique pairs from all accepted tracks within an event, and by taking tracks from two different but similar events. These histograms are binned as a function of either relative opening angles $(\eta_\Delta, \phi_\Delta)$ or transverse rapidity (y_{t1}, y_{t2}), though any other quantities could be used. In this analysis, sibling histograms were normalized to *average number of pairs per event*, and each mixed event histogram was normalized to match the corresponding sibling histogram of the same charge type. Then the sibling-to-mixed pair ratio was calculated as:

$$r_{LS} = \frac{\rho^{LS}_{sib}}{\rho^{LS}_{ref}} = \frac{\rho^{++}_{sib} + \rho^{--}_{sib}}{\rho^{++}_{ref} + \rho^{--}_{ref}} \tag{4.43}$$

$$r_{US} = \frac{\rho^{US}_{sib}}{\rho^{US}_{ref}} = \frac{\rho^{+-}_{sib} + \rho^{-+}_{sib}}{\rho^{+-}_{ref} + \rho^{-+}_{ref}} \tag{4.44}$$

$$r_{CI} = \frac{\rho^{LS}_{sib} + \rho^{US}_{sib}}{\rho^{LS}_{ref} + \rho^{US}_{ref}} \tag{4.45}$$

$$r_{CD} = \frac{\rho^{LS}_{sib} - \rho^{US}_{sib}}{\rho^{LS}_{ref} + \rho^{US}_{ref}}. \tag{4.46}$$

Ratios were found only within event samples containing similar multiplicities and event vertices as detailed in the next chapter. These ratios are then combined to obtain a single ratio per centrality bin using a weighted average based on the total number of sibling pairs from equation 4.17. Finally, these ratios are multiplied by the prefactors described in the previous section to obtain the final correlation

$$\frac{\Delta\rho}{\sqrt{\rho_{ref}}} = \sqrt{\rho^{ref'}}(r-1) \tag{4.47}$$

for each charge type.

4.5 Multiplicity Fluctuations

Section 4.3 constructs the correlation measure using counts of particle pairs. Expressing this again in terms of single-particle distributions directly connects correlations to multiplicity fluctuations, since the observed number of pairs depends on the distribution of event multiplicities. The goal of this research is not to measure multiplicity fluctuations for reasons discussed in the previous chapter, however the connection between correlations and fluctuations is an important component of the formalism and thus included here for completeness.

To examine the effect of event-wise multiplicity fluctuations on pair densities, let event multiplicity $n_i = \bar{n} + \delta_i$ where fluctuations are represented by random variable δ_i with mean $\bar{\delta} = 0$. Using overlines for event averages, the average total number of sibling *pairs* per event is

$$\begin{aligned} \bar{N}^{sib} &= \overline{n(n-1)} \\ &= \overline{(\bar{n}+\delta)\,(\bar{n}+\delta-1)} \\ &= \overline{[\bar{n}^2 + 2\bar{n}\delta + \delta^2 - \bar{n} - \delta]} \\ &= \bar{n}^2 - \bar{n} + 2\bar{n}\bar{\delta} - \bar{\delta} + \overline{\delta^2} \\ &= \bar{n}(\bar{n}-1) + \overline{(n-\bar{n})^2} \\ &= \bar{n}(\bar{n}-1) + \sigma_n^2 \end{aligned} \tag{4.48}$$

for multiplicity variance σ_n^2. The second-to-last line uses $\bar{\delta} = 0$ and substitutes $n - \bar{n}$ for δ. To restore bin dependence, we use this magnitude and define a unit normal

$$\hat{N}^{sib}(a,b) = \sum_i N_i^{sib}(a,b) / \sum_i \sum_{a,b} N_i^{sib}(a,b) \tag{4.49}$$

to write

$$N^{sib}(a,b) = \left[\bar{n}(\bar{n}-1) + \sigma_n^2\right] \hat{N}^{sib}(a,b). \tag{4.50}$$

Event-wise fluctuations average out in mixed events as

$$\begin{aligned}\bar{N}^{mix} &= \bar{n}_i\bar{n}_j \\ &= \bar{n}^2 \qquad (4.51)\end{aligned}$$

by simply using $\bar{n}_i = \bar{n}$. Using the unit normal as above, the average number of mixed pairs per events is

$$N^{ref}(a,b) = \bar{n}^2\hat{N}^{ref}(a,b). \qquad (4.52)$$

Following equations 4.15 and 4.16, the pair counts N are related to pair densities ρ which are formed into a ratio r. Starting with unit normal terms (denoted by a hat symbol)

$$\begin{aligned}\hat{\rho}(a,b) &= \frac{1}{\epsilon}\hat{N}(a,b) \qquad (4.53) \\ \hat{r}(a,b) &= \hat{\rho}^{sib}(a,b)/\hat{\rho}^{ref}(a,b) \qquad (4.54) \\ &= \hat{N}^{sib}(a,b)/\hat{N}^{ref}(a,b) \qquad (4.55)\end{aligned}$$

For the full normalization including multiplicity fluctuation terms the definitions are the same as above without the hat symbols. The effect of multiplicity fluctuations on the ratio is

$$\begin{aligned}r(a,b) &= N^{sib}(a,b)/N^{ref}(a,b) \qquad (4.56) \\ &= \frac{[\bar{n}(\bar{n}-1)+\sigma_n^2]}{\bar{n}^2}\frac{\hat{N}^{sib}(a,b)}{\hat{N}^{ref}(a,b)} \qquad (4.57) \\ &= \left[1+\frac{\sigma_n^2-\bar{n}}{\bar{n}^2}\right]\hat{r}(a,b) \qquad (4.58) \\ &= \left[1+\frac{\Delta\sigma_{n/}^2}{\bar{n}}\right]\hat{r}(a,b) \qquad (4.59)\end{aligned}$$

in terms of fluctuation measure $\Delta\sigma^2_{n/} \equiv (\sigma^2_n - \bar{n})/\bar{n}$, defined as the difference between the per-particle variance $\sigma^2_{n/} \equiv \sigma^2_n/\bar{n}$ and the small-scale limit defined to be 1 [34]. Thus the fluctuation provides an offset which propagates into the final $\frac{\Delta\rho}{\sqrt{\rho_{ref}}}$ correlation.

Note that equation 4.59 provides access to fluctuation measure $\Delta\sigma^2_{n/}$ in a pair-wise analysis using $r = \rho_{sib}/\rho_{ref}$ and $\hat{r} = \hat{\rho}_{sib}/\hat{\rho}_{ref}$ without having to measure the single-particle variance.

4.5.1 Charge Dependence of Multiplicity Fluctuations

Again, the calculation can be repeated while distinguishing between positive and negative charges. Following the method in 4.48 we have average total pairs

$$
\begin{aligned}
\bar{N}^{sib}_{++} &= \overline{n_+(n_+ - 1)} \\
&= \bar{n}_+(\bar{n}_+ - 1) + \sigma^2_{n+} && (4.60) \\
\bar{N}^{sib}_{--} &= \bar{n}_-(\bar{n}_- - 1) + \sigma^2_{n-} && (4.61) \\
\bar{N}^{sib}_{+-} &= \overline{n_+ n_-} \\
&= \overline{(\bar{n}_+ + \delta_+)(\bar{n}_- + \delta_-)} \\
&= \bar{n}_+\bar{n}_- + c_{+-} && (4.62) \\
\bar{N}^{sib}_{-+} &= \bar{n}_-\bar{n}_+ + c_{-+} && (4.63)
\end{aligned}
$$

where $c_{ab} = \overline{\delta_a \delta_b} = \overline{(n_a - \bar{n}_a)(n_b - \bar{n}_b)}$ is the covariance between charges a and b.

The mixed events are readily generalized as

$$
\begin{aligned}
\bar{N}^{ref}_{++} &= \bar{n}^2_+ && (4.64) \\
\bar{N}^{ref}_{--} &= \bar{n}^2_+ && (4.65) \\
\bar{N}^{ref}_{+-} &= \bar{n}_+\bar{n}_- && (4.66) \\
\bar{N}^{ref}_{-+} &= \bar{n}_-\bar{n}_+ && (4.67)
\end{aligned}
$$

The charge type ratios are

$$\begin{aligned} r_{\pm\pm}(a,b) &= N^{sib}_{\pm\pm}(a,b)/N^{ref}_{\pm\pm}(a,b) \\ &= \left[1 + \frac{\sigma^2_{n\pm} - \bar{n}_\pm}{\bar{n}^2_\pm}\right] \hat{r}_{\pm\pm}(a,b) \qquad (4.68) \\ r_{\pm\mp}(a,b) &= N^{sib}_{\pm\mp}(a,b)/N^{ref}_{\pm\mp}(a,b) \\ &= \left[1 + \frac{c_{+-}}{\bar{n}_+\bar{n}_-}\right] \hat{r}_{\pm\mp}(a,b) \qquad (4.69) \end{aligned}$$

where the last line uses $c_{+-} = c_{-+}$ by symmetry for unidentified particles.

These charge types are formed into the LS, US, and CD charge combinations following equations 4.20 through 4.23, and unit normal ratios $\hat{r}$ for these charge types following 4.55. To reduce the tedious notation the bin indices (a, b) are omitted below:

$$\begin{aligned} r_{LS} &= \frac{\bar{N}^{sib}_{++} + \bar{N}^{sib}_{--}}{\bar{N}^{ref}_{++} + \bar{N}^{ref}_{--}} \\ &= \left[1 + \frac{(\sigma^2_{n+} - \bar{n}_+) + (\sigma^2_{n-} - \bar{n}_-)}{\bar{n}^2_+ + \bar{n}^2_-}\right] \hat{r}_{LS} \qquad (4.70) \\ r_{US} &= \frac{\bar{N}^{sib}_{+-} + \bar{N}^{sib}_{-+}}{\bar{N}^{ref}_{+-} + \bar{N}^{ref}_{-+}} \\ &= \left[1 + \frac{c_{+-}}{\bar{n}_+\bar{n}_-}\right] \hat{r}_{US} \qquad (4.71) \\ r_{CI} &= \frac{(\bar{N}^{sib}_{++} + \bar{N}^{sib}_{--}) + (\bar{N}^{sib}_{+-} + \bar{N}^{sib}_{-+})}{\bar{N}^{ref}_{++} + \bar{N}^{ref}_{+-} + \bar{N}^{ref}_{-+} + \bar{N}^{ref}_{--}} \\ &= \left[\frac{\bar{n}^2 + \sigma^2_n - \bar{n}}{\bar{n}^2}\right] \hat{r}_{CI} \qquad (4.72) \\ r_{CD} &= \frac{(\bar{N}^{sib}_{++} + \bar{N}^{sib}_{--}) - (\bar{N}^{sib}_{+-} + \bar{N}^{sib}_{-+})}{\bar{N}^{ref}_{++} + \bar{N}^{ref}_{+-} + \bar{N}^{ref}_{-+} + \bar{N}^{ref}_{--}} \\ &= \left[\frac{(\bar{n}_+ - \bar{n}_-)^2 + \sigma^2_{(n_+-n_-)} - \bar{n}}{\bar{n}^2}\right] \hat{r}_{CD} \qquad (4.73) \end{aligned}$$

Ratio r_{CI} is equivalent to the form that does not distinguish charge types as in 4.59

of the previous section, though here it is written in a way that highlights comparisons to r_{CD}. The charge-independent r_{CI} contains the variance $\sigma^2 n$ of the distribution $n = n_+ + n_-$. In contrast, in the last line r_{CD} uses the variance of the distribution $(n_+ - n_-)$ defined as $\sigma^2_{(n_+ - n_-)} = \sigma^2_{n_+} - 2c_{+-} + \sigma^2_{n_-}$. In this way, the first three of the above equations show the fluctuation of total charge, while the last equation shows the fluctuation of net charge.

Consider a simple example where $\sigma_n^2 = \bar{n}$, as in the Poisson limit, and $\bar{n}_+ = \bar{n}_-$. Then the total charge fluctuation $r_{CI} = \hat{r}_{CI}$, that is, there are no excess fluctuations to contribute to the amplitude. The net charge fluctuation $r_{CD} = (-2c_{+-}/\bar{n}^2)\,\hat{r}_{CD}$, which approaches zero in the absence of covariance between the positive and negative particles.

4.6 Momentum Correlations and Fluctuations

$\frac{\Delta\rho}{\sqrt{\rho_{ref}}}$ has been constructed to measure correlations in the *number* of particles detected, but this may be generalized to include particle properties or kinematics. Returning to the concept of a binned single-particle distribution, equation 4.14 defines a correlation based on the number of particles in two bins relative to a statistical reference. Instead, we could consider quantities other than particle count such as the amount of energy or transverse momentum in a bin, the total number of strange valence quarks in the particles, or the sum of a component of particle spins to list a few examples. At present, within this framework only p_t correlations have been studied in an effort to understand non-statistical p_t fluctuations as described in the previous chapter. This section motivates the correlation measure used in those analyses and shows the relationship to event-wise fluctuations.

4.6.1 Momentum Correlations

Number correlations defined in equation 4.14 are based on the covariance of $(n - \bar{n})$ in different histogram bins. This naturally suggests that transverse momentum correlations should measure $(p_t - \bar{p}_t)$. The $\bar{p}_t$ reference can be expressed as $\bar{p}_t = \bar{n}\hat{p}_t$ where $\hat{p}_t$ is the inclusive (all particles from all events) mean p_t, and this product shows that fluctuations away from the mean in either the number of particles or the average momentum per particle are included in p_t. These terms may be decoupled by manipulating the expression

$$\begin{aligned} p_t - \bar{p}_t &= p_t - \bar{n}\hat{p}_t + n\hat{p}_t - n\hat{p}_t && (4.74) \\ &= (p_t - n\hat{p}_t) + \hat{p}_t(n - \bar{n}) && (4.75) \end{aligned}$$

The proper statistical reference for p_t is $n\hat{p}_t$, *i.e.* the amount of p_t that n particles should have.

Similarly, squaring this equation to perform the same expansion on p_t variance $\overline{(p_t - \bar{p}_t)^2}$ gives

$$\overline{(p_t - \bar{p}_t)^2} = \overline{(p_t - n\hat{p}_t)^2} + 2\hat{p}_t\overline{(p_t - n\hat{p}_t)(n - \bar{n})} + \hat{p}_t^2\overline{(n - \bar{n})^2} \qquad (4.76)$$

which is a variance in mean p_t production, a $p_t - n$ covariance, and a multiplicity variance. Therefore, the p_t correlation measure is defined with the covariance of $(p_t - n\hat{p}_t)$ instead of $(p_t - \bar{p}_t)$. To facilitate comparison between number and p_t correlations, the product of variances in the denominator of the correlation definition will remain the same. The final definition for the p_t correlation measure is then [54]

$$\frac{\Delta\rho(p_t : n)}{\sqrt{\rho_{ref}(n)}} = \frac{\overline{(p_t - n\hat{p}_t)_a\,(p_t - n\hat{p}_t)_b}}{\sqrt{\bar{n}_a\bar{n}_b}} \qquad (4.77)$$

where p_{ta} is the scalar sum of p_t's from all of the particles in bin a.

In a pair-wise analysis, this can be measured by multiplying the terms through

$$\left(p_t - n\hat{p}_t\right)_a \left(p_t - n\hat{p}_t\right)_b = p_{ta}p_{tb} - \hat{p}_t(n_a p_{tb} + n_b p_{ta}) + \hat{p}_t^2 n_a n_b \tag{4.78}$$

In a number correlation analysis, pairs are binned into a histogram $n_a n_b$, where the count in bin (a, b) is incremented for each pair. For p_t correlations, three additional histograms are necessary. The first term is stored in a histogram where bin (a, b) is incremented by the product $p_{t1}p_{t2}$. The second and third terms are stored in histograms incremented by p_{t1} or p_{t2}, respectively. The four terms are combined with appropriate factors of $\hat{p}_t$ after all pairs have been processed.

4.6.2 Momentum Fluctuations

Historically, the transverse momentum fluctuation measure $\Delta\sigma^2_{p_t:n}$ was defined first in [28] motivated by the desire to decouple number and momentum fluctuations as described above compared to a statistical reference. The correlation measure $\frac{\Delta\rho(p_t:n)}{\sqrt{\rho_{ref}(n)}}$ from [31] was constructed to correspond to $\Delta\sigma^2_{p_t:n}$ through an integral equation. Instead of considering pairs, $\frac{\Delta\rho(p_t:n)}{\sqrt{\rho_{ref}(n)}}$ was found by measuring the scale dependence of $\Delta\sigma^2_{p_t:n}$ and inverting the equation through the method described in detail in [34]. This process is computationally more efficient but much more technically challenging than measuring correlations by considering particle pairs. Since the research presented in this dissertation does not measure p_t correlations, an exhaustive derivation will not be given here. Instead, a summary will be presented to provide supporting background for the discussions of fluctuations and correlations in the previous chapter and elsewhere.

The relationship between fluctuations and correlations is concisely given in [54] as follows using one dimension for simplicity, though extending to two dimensions straightforward and necessary for axial autocorrelations. The fluctuation measure $\Delta\sigma^2_{p_t:n}$ over scale δx is written as a sum over pairs of bins with indices (a, b). Within δx there are m total bins with width ϵ_x, thus the mean multiplicity is $\bar{n}(\delta x) = m\bar{n}(\epsilon_x)$. This sum is manipulated into an autocorrelation (equation 4.77) as an average over the k^{th} diagonal, see figure 4.4, left panel.

$$\begin{aligned}
\Delta\sigma^2_{p_t:n}(\delta x) &= \overline{[p_t(\delta x) - n(\delta x)\hat{p}_t]^2}/\bar{n}(\delta x) - \sigma^2_{\hat{p}_t} &\quad (4.79)\\
&= \sum_{a,b=1}^{m} \frac{\overline{[p_t(\epsilon_x) - n(\epsilon_x)\hat{p}_t]_a[p_t(\epsilon_x) - n(\epsilon_x)\hat{p}_t]_b}}{m\bar{n}(\epsilon_x)} &\quad (4.80)\\
&= \sum_{k=1-m}^{m-1} K_{m:k}\frac{\bar{n}_k}{\bar{n}}\left\{\frac{1}{m-|k|}\sum_{1\le a,b\le m}^{a-b=k}\frac{\sqrt{\bar{n}_a\bar{n}_b}}{\bar{n}_k}\right.\\
&\qquad \left.\frac{\overline{[p_t(\epsilon_x) - n(\epsilon_x)\hat{p}_t]_a[p_t(\epsilon_x) - n(\epsilon_x)\hat{p}_t]_b}}{\sqrt{\bar{n}_a\bar{n}_b}}\right\} &\quad (4.81)\\
&= 2\sum_{k'=1}^{m'} K_{m':k'}\epsilon_x \frac{\Delta\rho(p_t:n;k'\epsilon_x)}{\sqrt{\rho_{ref}(n;k'\epsilon_x)}} &\quad (4.82)
\end{aligned}$$

Subtracting the single-particle variance $\sigma^2_{\hat{p}_t}$ in the first line eliminates contributions from self-pairs (forming a pair by combining a particle with itself). In 4.80 and below this term can be omitted by excluding the $a = b$ terms from the summations. Factor $\frac{\sqrt{\bar{n}_a\bar{n}_b}}{\bar{n}_k}$ in 4.81 uses the number of pairs in bin (a, b) as a weight in the average across diagonal k. Kernel $K_{m:k} \equiv (m - k + 1/2)/m$ represents the binning scheme. The term in braces becomes $\frac{\Delta\rho(p_t:n)}{\sqrt{\rho_{ref}(n)}}$ using a factor of bin width ϵ_x to convert to a density. In the last line of the derivation, equation 4.82, the sum indexes bins along relative separation $x_\Delta = k'\epsilon_x$ in a histogram. The factor of two exploits symmetry about the origin.

Moving from a function of one variable to a function of two variables brings out another factor of two and another bin width. For axial autocorrelations on

$(\eta_\Delta, \phi_\Delta)$ the inversion relation is [31]

$$\Delta\sigma^2_{p_t:n}(m\epsilon_\eta, n\epsilon_\phi) \quad = \quad 4\sum_{k',l'=1}^{m,n} K_{mn;k'l'}\epsilon_\eta\epsilon_\phi \frac{\Delta\rho(p_t:n;k'\epsilon_\eta,l'\epsilon_\phi)}{\sqrt{\rho_{ref}(n;k'\epsilon_\eta,l'\epsilon_\phi)}} \qquad (4.83)$$

where the 2D Kernel $K_{mn:kl} \equiv [(m-k+1/2)/m][(n-l+1/2)/n]$ and, as before, primed indices denote binned difference variables for $\eta_\Delta = k'\epsilon_\eta, \phi_\Delta = l'\epsilon_\phi$, at bin centers.

Chapter 5

Analysis Details

The previous chapter reviewed the formalism of combining pair densities into a correlation measure. The specific details of measuring these pair densities are the subject of this chapter.

Analyzing particle pairs can be computationally demanding, particularly when considering millions of events that may each have on the order of millions of possible unique pairs. It is therefore much more efficient to measure many correlations and autocorrelations simultaneously to avoid re-processing the data and forming these trillions of pairs multiple times. The results for the next three chapters, covering charge-independent and charge-dependent axial autocorrelations as well as transverse correlations, were all measured simultaneously in a single pass through each data set. As a consequence event, track, and pair selection detailed here are common to all analyses in the following chapters.

5.1 Event Selection

5.1.1 Events Cuts

Events are drawn from two data sets, the 62 GeV Au+Au collisions from RHIC Run 4 (years 2003-4), and 200 GeV Au+Au from Run 2 (2001-2). A minimum-bias sample of events was selected using STAR's *Hadronic Minbias* trigger requiring a minimum threshold of energy deposited in the Central Trigger Barrel, coincidence in both Zero-Degree Calorimeters, and a reconstructed event vertex. This is accomplished in STAR by examining the 16-bit `triggerWord` identifier for each event. Further, event vertices were required to be located in $|z| \leq 25$ cm, well within the fiducial volume of the TPC which extends to $z = \pm 100$ cm.

5.1.2 Centrality

Each event must be assigned to a certain centrality bin by mapping multiplicity to centrality, and ultimately to a detector-independent collision geometry. The standard in STAR uses a reference multiplicity within the region $|\eta| < 0.5$ to define centrality bins. Determining centrality by constraining the number of particles within a certain angular acceptance, as with the reference multiplicity, introduces an artifact in the correlation structure for $|\eta| < 0.5$ and thus for $\eta_\Delta < 1.0$. (The fact that one could in principle use correlations alone to reverse engineer the acceptance regions for a reference multiplicity testifies strongly to the sensitivity of this analysis.) We are then forced to generate our own mapping from measured multiplicity to centrality for $|\eta|/leq1$.

This is accomplished by measuring the multiplicity frequency distributions for a given set of event and track cuts and integrating the area under the curve into centrality fractions. However, these fractions suffer from inefficiencies in the event trigger, vertex reconstruction, and tracking as well as excesses from background con-

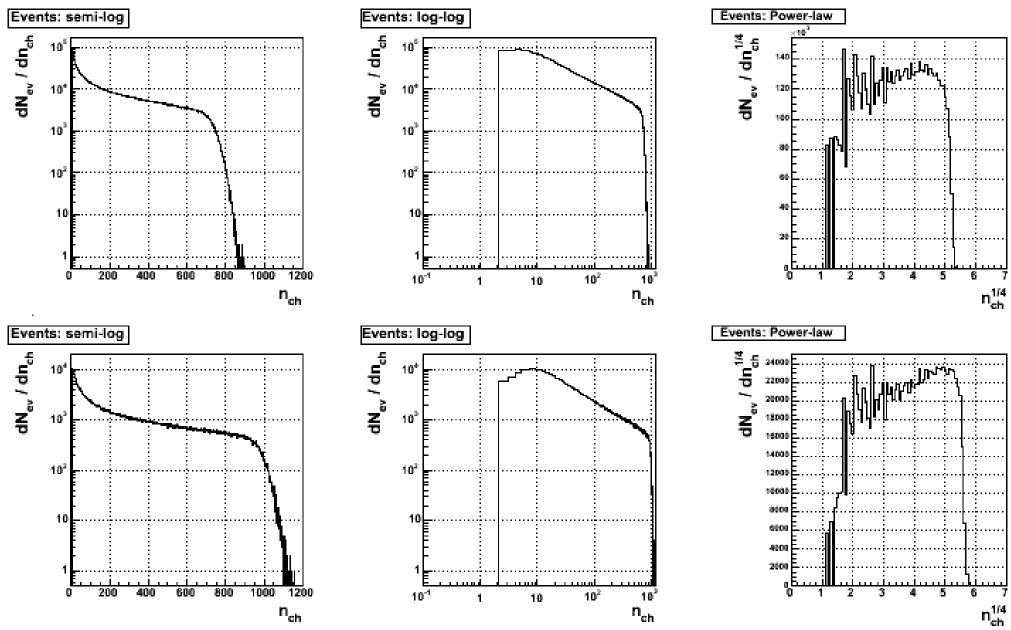

Figure 5.1: Distribution of (uncorrected) event multiplicities in $|\eta| \leq 1$ for 62 GeV (top row) and 200 GeV (bottom row) collisions in semi-log (left), log-log (center), and power-law (right) formats.

tamination. By taking these effects into account the uncorrected (or raw) centrality fractions may be corrected into a detector-independent estimate.

Following this procedure, figure 5.1 shows the multiplicity frequency distributions for both data sets. These histograms can be normalized to unity, then the bin contents summed with a running integral to determine which multiplicity values lie at certain (uncorrected) centrality fractions. This mapping of centrality bin divisions to event multiplicities is listed in table 5.1. This shows, for example, that a 62 GeV event with 300 tracks would fall in the 20-30% centrality bin, and in the 30-40% bin for 200 GeV. Events with multiplicity on a bin edge listed in the table are placed into the more central bin, so a 62 GeV event with 10 tracks is placed in the 80-90% bin rather than the 90-100% bin. This mapping is specific to a certain set of event and track cuts. The event counts for each centrality bin are given

Centrality (%)	**62 GeV Multiplicity**	**200 GeV Multiplicity**
90	10	15
80	24	35
70	46	68
60	81	117
50	129	187
40	194	281
30	280	401
20	389	551
10	532	739
5	622	852

Table 5.1: Mapping of (uncorrected) centrality bin edges to event multiplicities for 62 GeV (second column) and 200 GeV (third column) Au+Au collisions for the system of event and track cuts described in this chapter.

in table 5.2. The events have been divided into roughly equal centrality fractions, though since centrality bins are determined by multiplicity which is constrained to be an integer, the event counts cannot be identical in each bin.

The standard semi-log form of the multiplicity frequency distribution is shown in the left column of figure 5.1 for 62 (top row) and 200 (bottom row) GeV events. These are replotted in a log-log form in the center column, surprisingly revealing a power-law dependence with an approximate slope of -3/4. This dependence gives rise to the power-law centrality method [58], where this distribution is approximated by a $n^{-3/4}$ power-law trend. Then $d\sigma/dn \propto n^{-3/4}$ implies $d\sigma/dn\, n^{3/4} \propto const$ and thus $d\sigma/dn^{1/4} \propto const$ by treating the $n^{3/4}$ term as a Jacobian during the changing of variables $dn = 4n^{3/4}dn^{1/4}$. The right column in figure 5.1 shows the power-law form of $dN_{ev}/dn_{ch}^{1/4} \equiv 4n_{ch}^{3/4}dN_{ev}/dn_{ch}^{1/4}$ versus $n_{ch}^{1/4}$. This form provides an excellent diagnostic of trigger inefficiencies and background contamination in peripheral collisions by comparing the left endpoint of the power-law plot to the proton-proton multiplicity.

Centrality (%)	**62 GeV Events**	**200 GeV Events**
90 - 100	652,126	116,800
80 - 90	733,414	128,262
70 - 80	676,172	126,836
60 - 70	700,306	122,778
50 - 60	675,211	124,000
40 - 50	677,768	124,303
30 - 40	683,859	123,642
20 - 30	674,859	122,732
10 - 20	635,263	122,596
5 - 10	315,298	60,925
0 - 5	321,039	56,479
Total	*6,745,315*	*1,229,351*

Table 5.2: Number of accepted events in each centrality bin for 62 GeV (second column) and 200 GeV (third column) Au+Au collisions. The centralities listed in the first column are uncorrected.

Corrected centrality fractions were estimated using power-law methods and a Monte Carlo Glauber simulation incorporating efficiency and background estimates. A general overview of Glauber modeling is given in [59], while details of this particular simulation are given in [60] with results showing uncorrected versus corrected centrality fractions listed in table 5.3. Additionally, this Glauber simulation also provides estimates for other geometric centrality measures such as N_{part} and N_{bin} which will be used later to check for possible scaling trends.

5.1.3 Event Mixing

The final consideration in event selection remains in choosing sets of different but similar events for use in forming mixed event pair density ρ_{ref}. Two criteria are examined: event multiplicity differences, and separation distance of the z-coordinate of event vertices.

Raw Centrality (%)	**62 GeV Corrected**	**200 GeV Corrected**
100	95	93
90	84	84
80	75	74
70	65	64
60	56	55
50	46	46
40	37	38
30	28	28
20	18	18
10	9	9
5	5	5
0	0	0

Table 5.3: Estimated corrected centrality bin divisions listed as percentages of total cross section for 62 GeV (second column) and 200 GeV (third column).

Multiplicity

The multiplicity difference $\Delta n \equiv |n_1 - n_2|$ constraint provides two important corrections for the uncorrelated reference. First, the correlation structure may vary rapidly with multiplicity, so limiting the Δn range ensures the structures in the reference closely match those in sibling pairs. Second, setting an upper limit on Δn guarantees that approximately the same number of sibling and mixed event pairs are produced for each event.

During the analysis, events are only mixed within the same centrality bin. The data samples are divided into eleven centrality bins: nine bins covering a nominal ten percent of the total cross section each as 90-100%, 80-90%, ..., 10-20%; while the top ten percent most central events are subdivided into two bins as 0-5% and 5-10%. The correlation structure evolves most rapidly with multiplicity in peripheral events, so using this centrality binning scheme with many peripheral bins ensures that structure does not change too much within a single bin. Tests with further subdividing peripheral bins showed no significant difference compared to the statistical error. For more central bins, an upper limit of $\Delta n < 50$ is imposed, so centrality bins more than 50 tracks "wide" are subdivided into two or more multiplicity bins. Differences between Δn of 50 and 75 are small, though setting Δn at or above 100 introduced some artifacts, particularly at large η_Δ.

Using this method, the eleven centrality bins are formed by combining 18 (22) multiplicity bins at 62 (200) GeV, each with $\Delta n < 50$. The multiplicity bin divisions are

62 GeV: 2, **10, 24, 46, 81, 129, 194**, 237, **280**, 335, **389**, 437, 484, **532**, 597, **622**, 672, 722, 2000

200 GeV: 2, **15, 35, 68, 117**, 152, **187**, 234, **281**, 341, **401**, 451, 501, **551**, 614, 676, **739**, 796, **852**, 902, 952, 1002, 2000

The bold numbers represent centrality bin divisions also given in table 5.1 For example, in 62 GeV **10** is the uncorrected 90% fraction, and **24** is 80%; thus events with 10-23 tracks are assigned to the 80-90% bin (events on bin edges go into more central bins). Non-bold numbers are used for multiplicity bins which subdivide centrality bins. Thus, a correlation is formed in 62 GeV events with 194-237 tracks separately from events with 238-279 tracks. Then 30-40% bin is formed by combining these using a pair-weighted average as described in the previous chapter.

Vertex Position

Event cuts specify a range of longitudinal event vertex position $|z| < 25$ cm. Even within this range there is significant variation of the η acceptance as illustrated in figure 5.2. The left panel shows the measured η distribution for events with vertex z-coordinate from -25 to -20 cm, while the right panel contains events from +20 to +25 cm. There is a substantial loss of tracks near the acceptance boundaries at $\eta = \pm 1$.

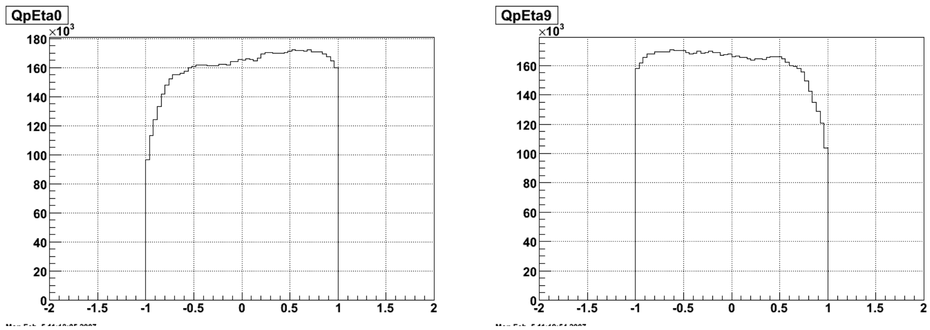

Figure 5.2: The measured η distributions of tracks in a sample of 200 GeV events with a vertex from $z = -25$ to -20 cm (left panel) and $z = +20$ to $+25$ cm (right panel).

To correct for this effect, events are placed in 10 z-vertex bins each 5 cm wide covering the full range from -25 to +25, and events are only mixed within a z-vertex bin. Constraining the difference Δz avoids producing unphysical structures at large η_Δ. Figure 5.3 shows the difference between mixing across all $|\Delta z| < 50$ cm (left column) and using the z-vertex bins where $|\Delta z| < 5$ cm (center column). 2D axial autocorrelations are shown with the view looking along the ϕ_Δ axis (the data have not been projected onto η_Δ). The right column shows the difference, which is found to be large for the 0-5% central events (top row) and rapidly diminishing with decreasing centrality. The difference is barely significant within statistical error for the 10-20% bin (bottom row), and insignificant for all other centralities from 20-100%. Therefore, z-vertex binning is only used for the three most central bins 0-5%, 5-10%, and 10-20%.

As with multiplicity bins, the correlation is found within each individual z-vertex bin and combined using a weighted average. The final correlations for each centrality bin are the weighted average of 10 z-vertex bins per multiplicity bin. Thus the 0-5% centrality at 200 GeV is the weighted average of 40 individual correlations.

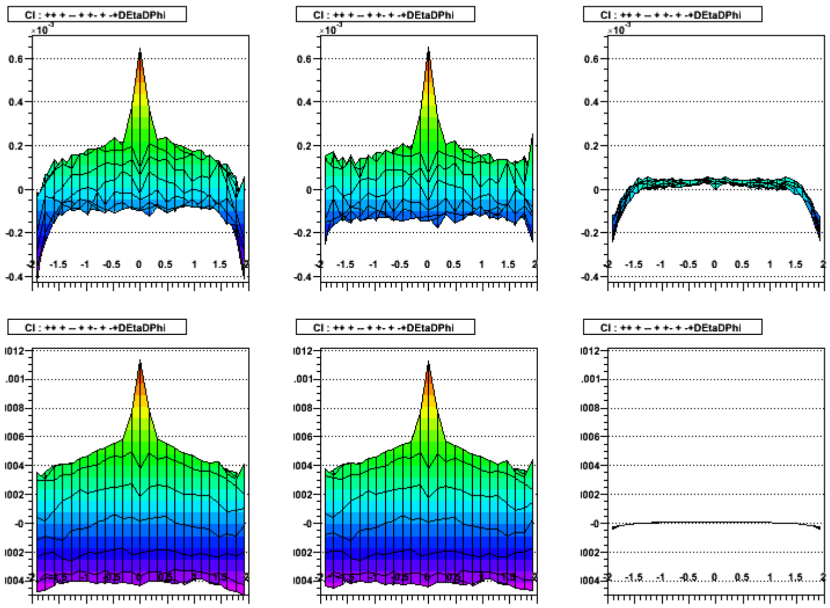

Figure 5.3: The effect of z-vertex position on event mixing. The first two columns show front-end views of axial autocorrelations for a sample of 200 GeV events mixed across $|\Delta z| < 50$ cm (left column) and $|\Delta z| < 5$ cm (center column). The difference is shown in the right column. Events are sampled from the 0-5% (top row) and 10-20% (bottom row) centralities.

5.2 Track Selection

Once events have been chosen, it is necessary to select tracks from these events for use in forming pairs. In general, the favored approach is to minimally-bias the track sample by requiring only basic reconstruction quality over as large a kinematic range as possible. Table 5.4 gives a complete list of track cuts used in these analyses. Many of these cuts are shown in figure 5.4 where accepted tracks are shown as red histograms and combined accepted and rejected tracks are shown in black. Track cuts fall into three categories: kinematics, reconstruction, and particle identification.

Cut	Min	Max	Comments
p_t (GeV/c)	0.15	15.45	Only excludes a few high p_t tracks
ϕ	$-\pi$	π	Entire azimuth
η	-1.0	1.0	Range of high acceptance in TPC
Global DCA (cm)	0	3.0	Distance of closest approach from track to vertex
NFitPoints	15	50	Number of fit points
NFitPerNMax	0.52	1.1	Corrects for track splitting
χ^2	0.0	3.0	Quality of helix fit to hit points
Flag	0	2000	Excludes negative values
Charge (e)	-1	1	Only accept tracks with charge of ± 1
NSigmaElectron	-1.5	1.5	loose dE/dX cut in certain momentum ranges

Table 5.4: Complete list of track cuts where the second and third columns give the minimum and maximum of the accepted range of values. The various cuts are described in the text.

5.2.1 Kinematic Cuts

The kinematic cuts include almost the full acceptance of STAR's TPC. For full magnetic field strength (0.5 T) the minimum detectable p_t is 0.15 GeV/c, as slower particles curl into helices before reaching the inner field cage. Occasionally tracks reconstructed with a very high p_t are problematic, so an upper limit of 15.45 GeV/c is set. As shown in the top-left panel of figure 5.4 this upper limit excludes a very tiny fraction of tracks. The next panel plots the distribution on transverse rapidity y_t.

The η range is set to ± 1 unit of pseudorapidity. Though the TPC extends further in η, the reconstruction efficiency drops rapidly beyond these limits as seen in the top-right panel in figure 5.4. The full azimuthal range from $\phi = \pm\pi$ is accepted. The small variations shown in the bottom-left panel of this figure are due to track losses at the twelve sector boundaries.

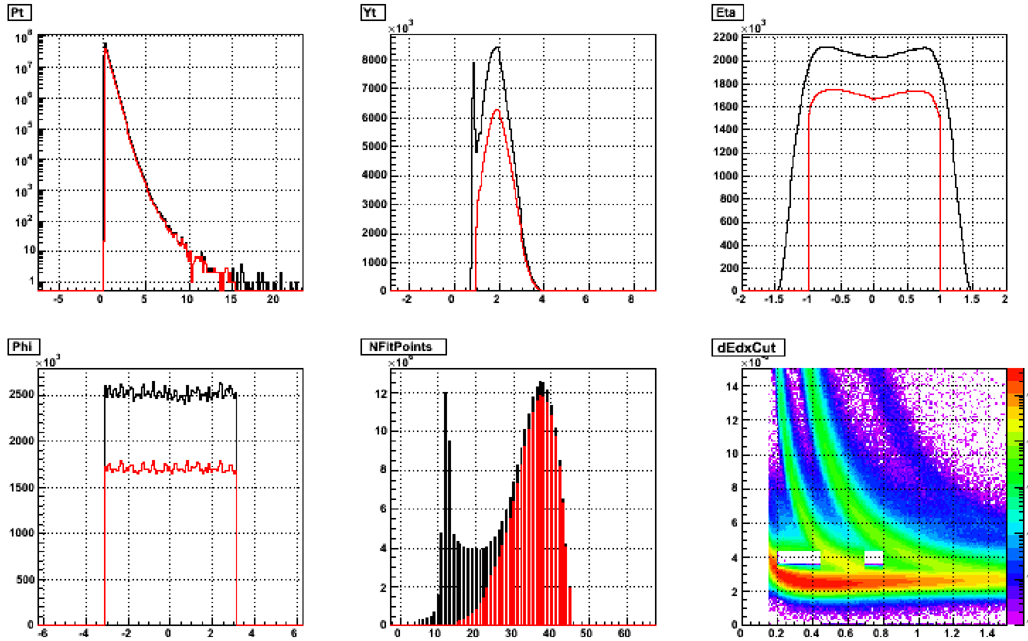

Figure 5.4: Track-level distributions for all tracks (black histogram) and only accepted tracks (red histogram) for all centralities in 200 GeV collisions. The top row shows p_t, y_t, and η from left to right. The bottom row shows ϕ (left), the number of fit points per track (center), and the dE/dx energy loss versus momentum for accepted tracks (right).

5.2.2 Track Reconstruction

A distance of closest approach (DCA) cut is used to distinguish primary particles produced in the original collision from secondary particles from weak decay or interactions with detector material. The DCA cut requires the reconstructed track to project back to within 3 cm of the event vertex.

Each track is required at have a minimum of 15 fit points in the TPC. The distribution of fit points is shown in bottom-center panel of figure 5.4. The minimum was chosen to avoid the large number of track fragments with 11-13 points. To avoid split tracks, where fit points from a single particle are reconstructed as two separate tracks, an estimate is made on the expected number of fit points based on the track's position within the TPC, and tracks are required to have at least 52% of the estimated maximum number of fit points.

Additional cuts include setting a limit on the χ^2 quality of the helix fit to the track hit points, and checking for errors flagged by the track reconstruction program as negative values of the `flag` variable. As a final check, only particles assigned a charge of $+e$ or $-e$ are accepted.

5.2.3 Particle Identification

No attempt was made in this analysis to identify particular hadron species, but it is still desirable to suppress the electron and position background relative to the hadron yield. The bottom-right panel of figure 5.4 shows dE/dx, the energy loss per unit path length in the TPC, versus particle momentum (using total rather than transverse momentum) of accepted particles. Cuts are made in places where the electron band is clearly distinguishable from other hadrons. A particle is excluded if it is within 1.5σ of the expected energy loss for electrons and in the momentum ranges $0.2 < p < 0.45$ GeV/c or $0.7 < p < 0.8$ GeV/c.

5.3 Pair Selection

Once events and particles have been chosen, the final step is to form pairs. The correlation analysis at 130 GeV devised methods of correcting for pair loss during track reconstruction. Since this pair loss affects sibling but not mixed event pairs non-physical structures may persist in the final correlation. The single-track cut based on the ratio of actual to estimated fit points removes track splitting artifacts where a single particle is reconstructed as two or more tracks. However, the reverse process, called track merging, is known to occur when hits from two nearby particles are reconstructed as a single track. Track crossing is an additional source of pair loss where one or both of the overlapping particles are not reconstructed correctly. This section examines and corrects for the effects of track splitting and merging. Additionally, the end of this section discusses the pair weighting procedure for acceptance corrections.

In the 130 GeV analysis an HBT/Coulomb cut was applied to help isolate the minijet correlations from the short-range quantum correlations and final-state interactions, since the quality of the data were not high enough to separate these structures in the same-side peak. However, at 62 and 200 GeV we now have enough events to isolate these contributions based on the different shapes of these structures. Additionally, the HBT/Coulomb cuts left sharp cut-offs which could be observed in the data, thus the final decision was to perform the analysis without using these cuts.

5.3.1 Reconstructed Pair Densities

If two nearby tracks are reconstructed as a single track, or if one or both overlapping particles are not reconstructed when tracks cross, then the sibling pair density at small relative angles will be lower than the mixed pair density causing an artificial anti-correlation. We can look for this effect directly by taking the ratio of sibling to mixed pair densities as functions of track separation distance. The η and ϕ dependences of pair loss will be decoupled by distinguishing between longitudinal (along the z-axis) and transverse (in the x-y plane) separation.

Figure 5.5 shows the sibling to mixed pair density ratio for ten centrality bins as a function of average transverse and longitudinal separation distances. The average separation is found by using the helix fits to find the track separation at the TPC entrance, midpoint, and exit (r = 50, 127, and 200 cm) and taking the average. This was found for every pair constructed in both sibling and mixed events. The ratio is approximately uniform (unit normalization, orange on this color scale) but

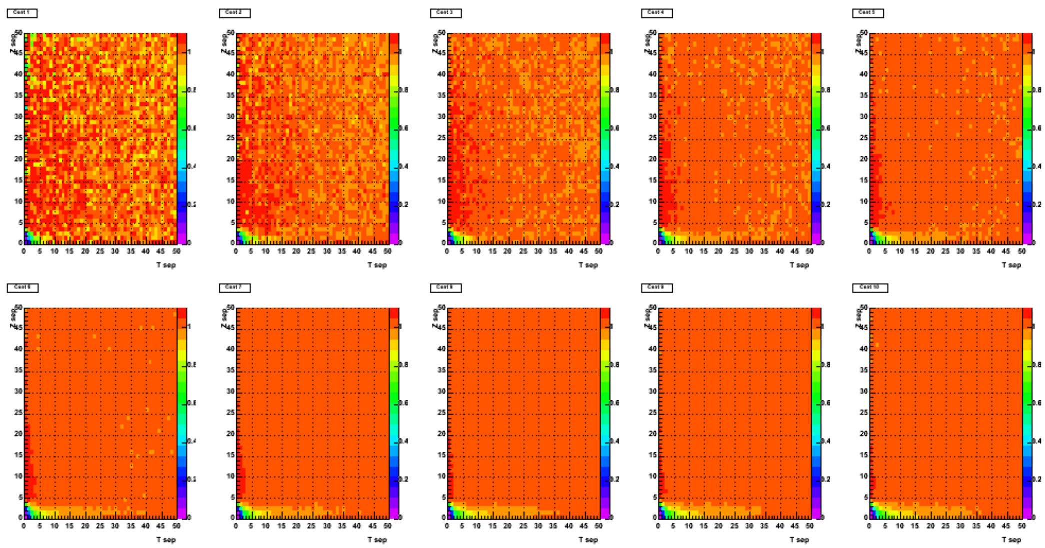

Figure 5.5: Ratio of sibling to mixed event pair densities as a function of transverse and longitudinal separation in cm for ten centralities from peripheral (top-left) to central (bottom-right).

sharply approaches zero near the origin in all centrality bins with an additional long tail following the transverse axis and increasing with more central events. Physical correlations also contribute to the sibling density, but at a smaller magnitude compared to pair loss effects. Physical correlations on $(\eta_\Delta, \phi_\Delta)$ are spread out and diluted when projected onto TPC separation distances due to track curvature variations within the p_t range.

The two known pair reconstruction inefficiencies are manifested in different ways. Track merging depends only on the absolute separation distance, thus it is symmetric on transverse and longitudinal separation and independent of centrality. Pair loss from track crossing is largely limited to the ϕ plane, or small longitudinal but a wide range of transverse separations. Track crossing effects are more pronounced at higher multiplicities where reconstruction is more difficult. Overall, the pair densities in figure 5.5 clearly show two different types of pair loss consistent

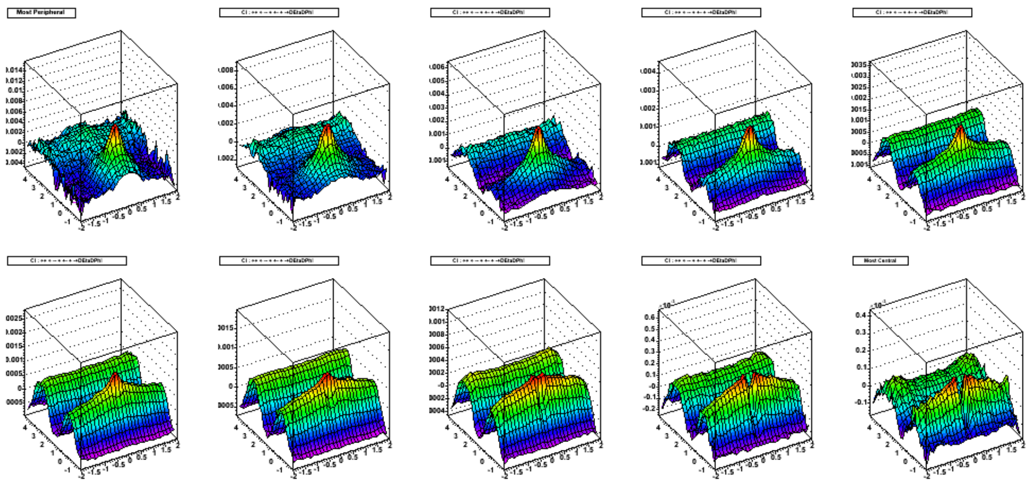

Figure 5.6: A sample of axial autocorrelations with no pair cuts in ten centrality bins. The most peripheral (top left) are not significantly affected by pair loss, whereas the most central (bottom right) show a large deficit.

with track merging and crossing.

Before attempting to correct for pair loss, it is reasonable to see how substantially this affects the final correlations. Figure 5.6 shows axial autocorrelations, to be studied extensively in the next chapter, with no corrections for pair loss. Track merging was found to have little effect in proton-proton collisions and is largely centrality-independent, so as expected no large structures due to track merging are visible. However, track crossing does depend on centrality, and the three most central histograms in the bottom-right show significant pair loss at small η_Δ (longitudinal separation) and within a range of ϕ_Δ (transverse separation). Careful pair selection and corrections will in fact be necessary to remove these artifacts.

5.3.2 Track Merging

The pair density ratios in figure 5.5 show pair losses from track merging in the lower-left corner of each panel where the ratio approaches zero for small distances.

The ratio is well below unity for separations of less than 5 cm for both longitudinal and transverse separations. This observation compares well with the 130 GeV result [61] where the magnetic field was at half strength and the ratio deviates significantly from unity up to separations of 10 cm.

Based on these measurements, pairs with average longitudinal and transverse separation distances both less than five cm will be excluded to correct for track merging. To avoid over-correction, pairs are excluded from both the sibling and mixed event sets to remove pair loss artifacts from the ratio.

5.3.3 Pair Crossing

When two tracks cross in the TPC, one or both tracks may be split near the intersection point. These split tracks will then be removed by the track cut requiring at least half of all possible fit points. Overall, this will cause a deficit of sibling event pairs relative to mixed event pairs. To correct for track crossing we must remove pairs which may cross, so for each pair we consider the relative charge signs, momenta, azimuth, as well as the sign of the magnetic field. Examples of pair crossing geometries are shown in figure 5.7 from [61].

Since the magnetic field bends particles in the ϕ plane only, track crossing is only relevant at small longitudinal separations but over a wide range of transverse separations. However, many other factors apply. Considering particles with the same charge sign and same azimuth difference, the relative momentum determines whether these tracks will cross. The potential crossing geometries in a positive magnetic field are:

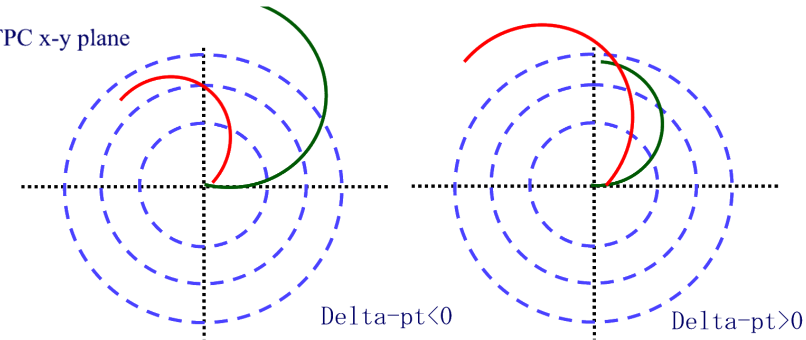

Figure 5.7: An example of track crossing geometries for negative particles in a full field. If the red track is particle 1 and green is particle 2, then $\Delta\phi$ is positive in both panels. In the left panel Δp_t is negative and the tracks do not cross, while the right panel shows positive Δp_t and crossing tracks [61].

Charges	May cross if...
$++$	$\Delta\phi$ and Δp_t have opposite signs
$--$	$\Delta\phi$ and Δp_t have the same sign
$+-$	$\Delta\phi > 0$
$-+$	$\Delta\phi < 0$

For a reversed magnetic field, either flip the charge signs or logically reverse the rules. In this discussion, pair order matters when $\Delta\phi$ or Δp_t are taken as signed quantities. *i.e.* for $\Delta\phi \equiv \phi_1 - \phi_2$ and $\Delta p_t \equiv p_{t1} - p_{t2}$ the same particle must be used for both ϕ_1 and p_{t1}, and reversing the order of the particles reverse the signs of both $\Delta\phi$ and Δp_t.

Considering this complex dependence on azimuth and momentum, *if* the pair loss observed in central bins in figures 5.5 and 5.6 is due to track crossing then these dependences should exist in the pair density ratios. The sibling to mixed density ratio is shown in figure 5.8 for only pairs with $\Delta\phi > 0$ as a function of transverse (top row) and longitudinal (bottom row) separation for every possible combination of charge types. In addition, pairs with $\Delta p_t > 0$ are shown in black, $\Delta p_t < 0$ in red.

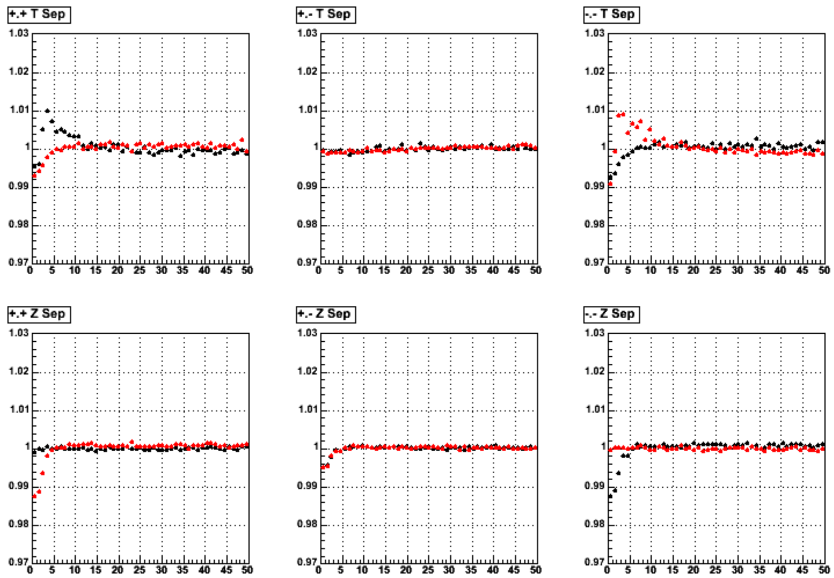

Figure 5.8: Effects of track crossing in a full field. Points show sibling to mixed pair ratios for all pairs with positive $\Delta\phi$ as a function of transverse (top row) and longitudinal separation (bottom row). Color distinguishes Δp_t with positive in black and negative in red. Columns show different pair charge types.

No pair cuts have been applied, and the η_Δ range is not restricted.

To illustrate the effect of track crossing, the top-left panel shows the positively charged pairs. Since all pairs in this figure have $\Delta\phi > 0$, from the table above only pairs with $\Delta p_t < 0$ (red points) may cross. The black points show the expected positive correlation from HBT, being same-signed nearby particles. Both have a negative correlation (the ratio is less than one) as the separation approaches zero. Comparing the other panels the unlike-sign pairs (center column) do not depend on Δp_t, as the red and black points lie on the same line, and are unaffected by track crossing. To summarize, if pair loss was due to merging only, the red and black points would agree. Instead we see losses precisely consistent with the track crossing geometries listed above.

As further evidence of track crossing, figure 5.9 shows the same analysis for

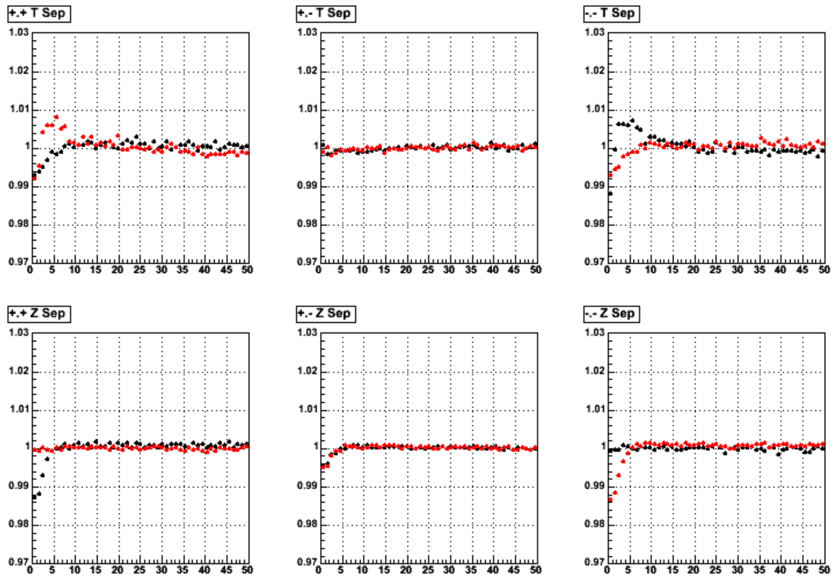

Figure 5.9: Same as previous figure except for reversed magnetic field. All pairs have positive $\Delta\phi$, while Δp_t is shown in black for positive and red for negative.

events with a reversed magnetic field. Comparing the two figures we observe that the dependence on the sign of Δp_t flips under a reversed magnetic field.

Track crossing effects, seen in the figures as differences between the black and red points, clearly extend to longitudinal separations of 5 cm. The exact placement of the cut is more difficult in transverse separation. The ratios are normalized by total number of pairs which introduces a relative shift between points with and without pair loss from crossing. Since the points without pair loss have a small negative slope, the normalization difference causes shifts in the crossing point.

To determine the transverse range of the crossing cut, I began at 10 cm and slowly extended the range until the pair loss visible in the correlation plots (figure 5.6) was acceptably small compared to the nearby structures. The emphasis on this process was to exclude as few pairs as possible, so some residual track crossing inefficiencies remain. The final track crossing cut removes both sibling and mixed pairs that have a crossing geometry as listed above, an average longitudinal separation of < 5 cm, and an average transverse separation of < 35 cm.

5.3.4 Pair Weighting

Forming pairs by randomly sampling particles within an η range of ± 1 creates far more pairs at $\eta_\Delta = 0$ then $\eta_\Delta = \pm 2$. Assume we divide the η range into 25 bins, and particles are uniformly distributed among these bins. To form a pair with $\eta_\Delta = 0$, the first particle may be in any bin, while the second has a 1/25 chance of being in that same bin. However, forming a pair at $\eta_\Delta = +2$ requires a 1/25 chance that the first particle is in the $\eta = 1$ bin and another 1/25 chance that the second is at $\eta = -1$. Thus, for 25 bins we are 25 times more likely to find pairs at $\eta_\Delta = 0$ than $\eta_\Delta = 2$ or -2. The probability is linear with η_Δ, since there is one valid bin pair which forms $\eta_\Delta = 2$, two valid bin pairs which form the next smallest η_Δ, three bin pairs for the next smallest η_Δ, and so on. Thus the overall pair acceptance function has a triangular shape. Mathematically this can be derived from convoluting the single-particle η distribution with itself. The convolution of two functions $f(t)$ and $g(t)$ is defined as (see *e.g.* [62])

$$(f * g)(t) \equiv \int_{-\infty}^{\infty} d\tau f(\tau) g(t-\tau). \tag{5.1}$$

The procedures in chapter 4 use a mixed event reference to remove this acceptance in the axial autocorrelations. However, in a transverse (y_t, y_t) analysis this procedure cannot correct the bias for small η_Δ pairs over large η_Δ pairs. Therefore, every pair will be weighted based on the pair's η_Δ value to correct both the η acceptance in axial autocorrelations and the bias in transverse correlations. The pair weight must be the inverse of the pair acceptance, so for a triangular pair acceptance the weighting is

$$\text{weight} = (1 - |\eta_\Delta|/\eta_{\Delta,max})^{-1} \tag{5.2}$$

(*i.e.* triangle^{-1}) with maximum range $\eta_{\Delta,max} = 2$. The weights are applied when the pairs are binned, and the η_Δ value used above is from the bin center of the η_Δ histogram instead of the each individual pair's η_Δ.

Chapter 6

Charge-Independent Axial Autocorrelations

The previous chapters have developed all of the framework necessary for a physics analysis using the procedures described in chapter 4 and the data selected in chapter 5. This chapter presents the charge-independent axial autocorrelations $\frac{\Delta\rho}{\sqrt{\rho_{ref}}}(\eta_\Delta, \phi_\Delta)$ for $\sqrt{s_{NN}}$= 62 and 200 GeV Au+Au collisions.

6.1 Autocorrelation Data

For a reference, $\frac{\Delta\rho}{\sqrt{\rho_{ref}}}(\eta_\Delta, \phi_\Delta)$ in $\sqrt{s_{NN}}$=200 GeV proton-proton collisions is shown in the left panel of figure 6.1. The correlation measure has been constructed to be independent of multiplicity, so if heavy ion collisions behave exactly as a series of independent nucleon-nucleon collisions this correlation structure will not change in Au+Au collisions. Deviations from this reference represent new physics accessible at RHIC.

A previous study [41] has decomposed this structure into soft and hard as well as like-sign (LS) and unlike-sign (US) components as discussed in chapter 3

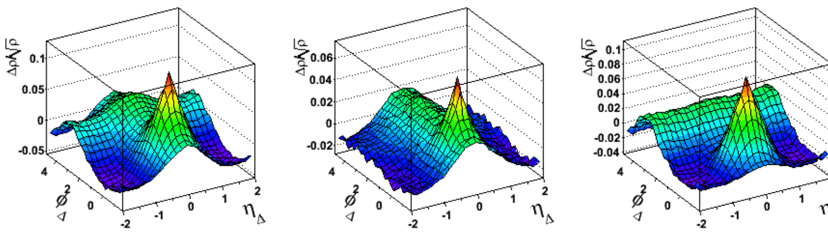

Figure 6.1: Charge-independent axial autocorrelations in 200 GeV p+p collisions for all pairs (left panel), soft pairs (center), and semi-hard pairs (right).

(see figure 3.11). There are three primary contributions to these correlations. Soft particle correlations, shown in the center panel of figure 6.1, are due to longitudinal fragmentation into unlike-sign pairs which produce a 1D Gaussian correlation centered along η_Δ=0. It is easiest to visually discriminate this piece by either looking at the very front edge of the plot along the η_Δ axis or as a bump in the center of the away-side ($|\phi_\Delta| > \pi/2$) ridge. The second contribution is the large peak centered at the $\eta_\Delta = \phi_\Delta = 0$ origin. Several physical processes produce small relative angle correlations [41]. Quantum interference, as studied in HBT analyses [42], produces a sharp exponential peak that dominates the LS soft particle component. For semi-hard pairs shown in the right panel of figure 6.1, minijet fragmentation produces a 2D Gaussian peak. A single bin precisely at the origin contains electron-positron pair contamination, though these have been suppressed with a dE/dx cut. The third contribution to the p+p axial autocorrelations is the away-side ridge centered at ϕ_Δ=π, which is due to momentum conservation in semi-hard scattering. For an inclusive p_t range, as in figure 6.1, the away-side is completely represented by function $-\cos(\phi_\Delta)$ (which also contributes the negative regions seen at $\phi_\Delta = 0$ and large $|\eta_\Delta|$). This cosine approximates a wide Gaussian which narrows with increasing p_t [41]. These three contributions will form the basis of the fit function used in the next section. It is worth noting that while in the p+p analysis y_t cuts were used to

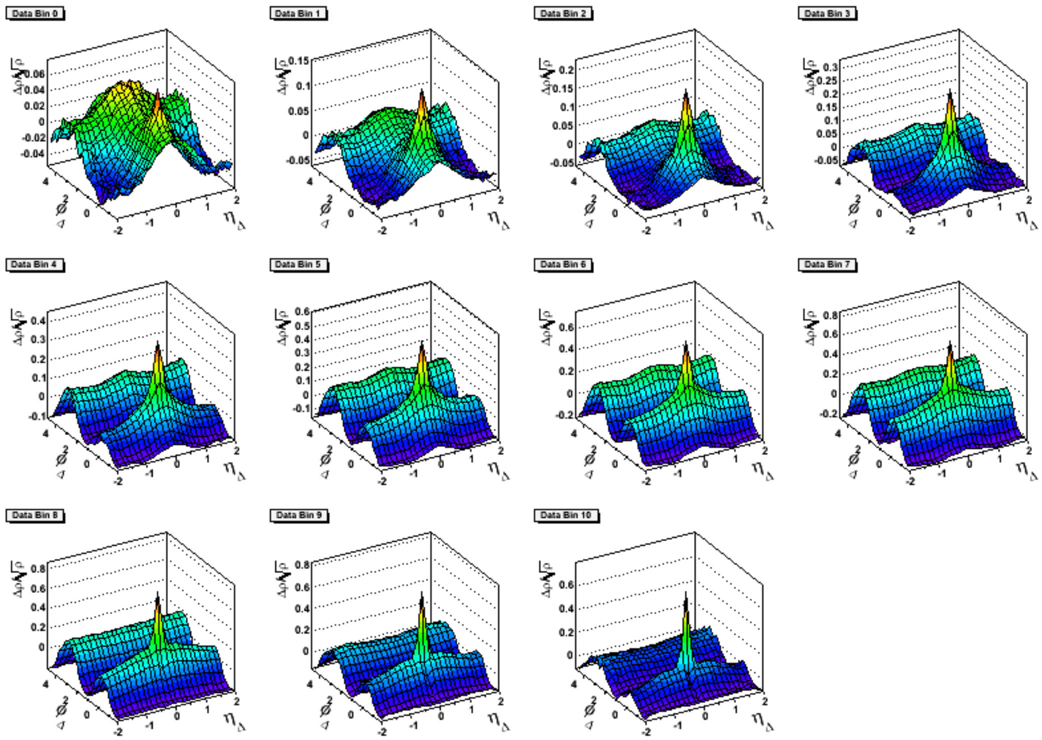

Figure 6.2: Axial autocorrelations in 62 GeV Au+Au from peripheral (top left) to central (bottom right) events.

isolate the soft and semi-hard components and examine their individual structures, the Au+Au correlation results shown here use the entire y_t range. The components will instead be decoupled based on correlation shape instead of a momentum range.

The axial autocorrelations in Au+Au collisions in eleven centrality ranges are shown in figure 6.2 for 62 GeV and figure 6.3 for 200 GeV collisions. The centrality bin numbers correspond to the cross section fractions listed in chapter 5 where bin 0 is 90-100% (uncorrected), bin 1 is 80-90 %, and so on. The peripheral collisions (top left panels) in 200 GeV Au+Au are very similar to p+p as expected, since peripheral heavy ion collisions approach the nucleon-nucleon limit at 100% centrality. The 62 GeV peripheral gives the first indication of energy dependence by

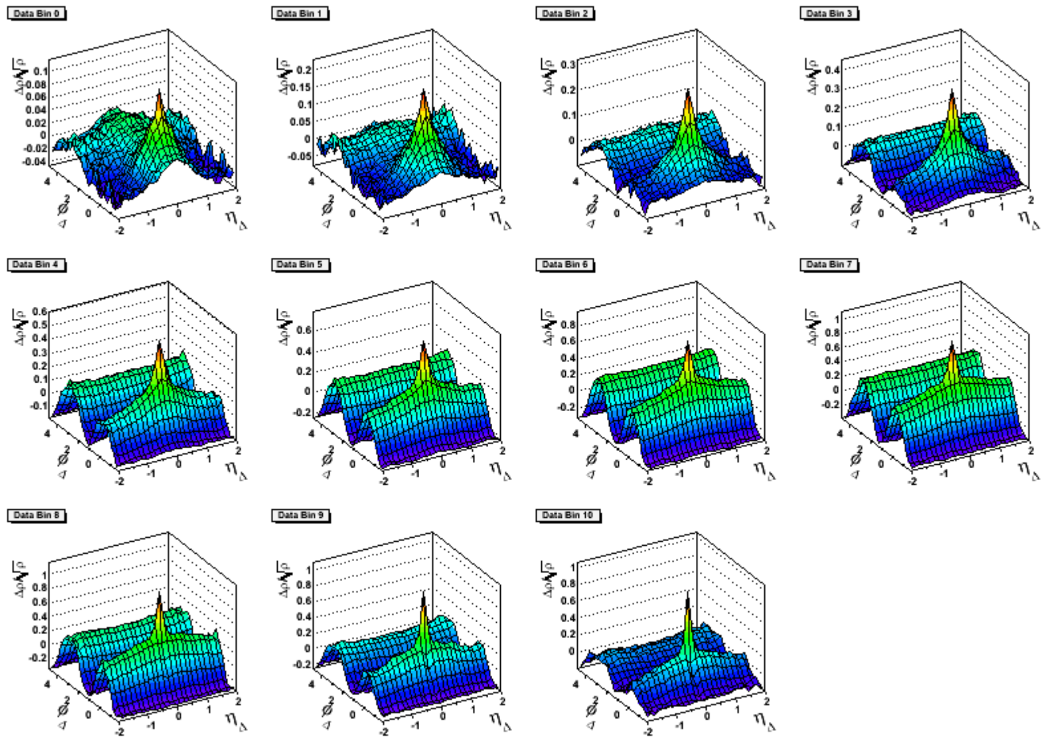

Figure 6.3: Axial autocorrelations in 200 GeV Au+Au from peripheral (top left) to central (bottom right) events.

showing a relatively larger soft component and a diminished semi-hard component. Three general trends may be observed with increasing centrality at either energy: a general growth in amplitude, the development of same-side ridge, and a dissipation in the soft component (most easily seen as a flattening of the away-side ridge).

The histograms in figures 6.2 and 6.3 are binned using 25 bins on the η_Δ axis and 24 bins on ϕ_Δ. The bins have been arranged so that the (0,0) origin is exactly centered within a bin, also this binning scheme ensures that all major angles ($\pi, \pi/2, \pi/6$, *etc.*) are also centered in a bin. For aesthetic reasons these histograms are shown with a redundant row of bins where the $\phi_\Delta = -\pi/2$ bins have been wrapped around and copied over to $\phi_\Delta = 3\pi/2$.

6.2 Fitting Procedure

Overall, the correlation structures observed in p+p and peripheral Au+Au are substantially modified in central collisions. To quantify the change we must fit each histogram with a model function and study the evolution of the fit parameters with energy and centrality.

6.2.1 Fit Function

As discussed above, these autocorrelations in p+p are modeled with a same-side (SS) 2D Gaussian, a SS 2D exponential, a 1D Gaussian centered at $\eta_\Delta = 0$, and a $-\cos(\phi_\Delta)$. To ensure the simplest possible fit function for Au+Au collisions, we use these components from p+p collisions with only one additional $\cos(2\phi_\Delta)$ term to account for correlations conventionally attributed to elliptic flow [52], which will be discussed in greater detail below. Since this fit function now has two sinusoid components, it is appropriate to adopt the terminology of a multipole moment expansion, which also has the benefit of providing labels for these terms which are independent of any physical process or model. In this nomenclature the $\cos(\phi_\Delta)$ term is referred to as the dipole, and the $\cos(2\phi_\Delta)$ as the quadrupole. Higher order moments are possible in principle, but will be excluded from this analysis to simplify the fit function and reduce the number of parameters as far as possible. The eleven parameter fit function used for the autocorrelation structures in figures 6.2 and 6.3 is then:

$$\begin{aligned} F &= A_{\phi_\Delta} \cos(\phi_\Delta) + A_{2\phi_\Delta} \cos(2\,\phi_\Delta) \\ &\quad + A_0 \exp\left[-\frac{1}{2}\left(\frac{\eta_\Delta}{\sigma_0}\right)^2\right] + A_1 \exp\left\{-\frac{1}{2}\left[\left(\frac{\phi_\Delta}{\sigma_{\phi_\Delta}}\right)^2 + \left(\frac{\eta_\Delta}{\sigma_{\eta_\Delta}}\right)^2\right]\right\} \\ &\quad + A_2 \exp\left\{-\left[(\phi_\Delta/w_{\phi_\Delta})^2 + (\eta_\Delta/w_{\eta_\Delta})^2\right]^{1/2}\right\} + A_3. \end{aligned} \tag{6.1}$$

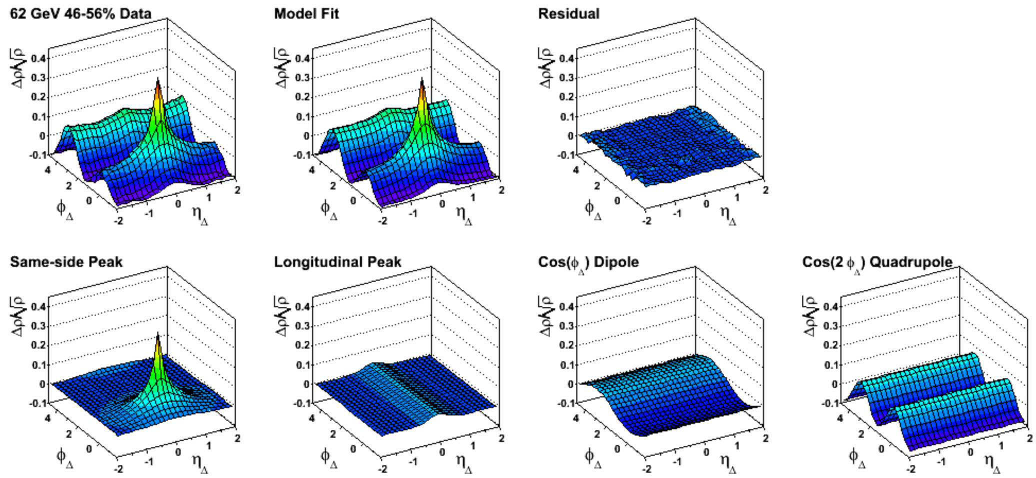

Figure 6.4: Example of fit components. Top row: mid-central 62 GeV data (left), complete model function fit (center), and residual (right). Bottom row: 2D Gaussian and 2D exponential peaks (left), 1D Gaussian (center-left), dipole (center-right), and quadrupole (right).

An example of the data are decomposed into these terms is given in figure 6.4. A mid-central 62 GeV histogram which has significant contributions from every component was chosen to illustrate the model. The top row shows the data along with the entire model fit and the residual (data minus the model). The bottom row shows how the fit function models individual components of the data. The bottom left panel shows the same-side peak model, which is the sum of the 2D Gaussian and exponential peaks. The second panel shows the measured amplitude and width of the 1D Gaussian, while the third and fourth panels show the dipole and quadrupole terms.

Parameter fits were performed using χ^2 minimization from the standard packages in ROOT [63]. All parameters are fit simultaneously. During the fitting process parameters were constrained as little as possible. Widths were constrained to be positive. The only constraint which affected the fit was requiring the 1D

Gaussian amplitude A_0 to be non-negative. Without this constraint this component was used by the fitter in the three most central bins to describe the small deficit from two-track inefficiencies seen along $\eta_\Delta = 0$ in the SS peak. In all other bins this component represents longitudinal fragmentation, so the non-negativity constraint was imposed to exclude contributions from tracking artifacts. The outermost bins at large $|\eta_\Delta|$ have the fewest contributing pairs and the highest statistical noise. The large χ^2 from the noise is this region introduced instabilities into the fit; bins from $1.84 < |\eta_\Delta| < 2.0$ were therefore excluded from the fit.

6.2.2 Alternative Fits

The $-\cos(\phi_\Delta)$ dipole adds a negative contribution on the SS ($\phi_\Delta < \pi/2$) which is not always visually apparent in the data. One potential problem could occur causing instability in the fit when an amplitude increase in the dipole is compensated by an increase in the 2D Gaussian artificially inflating these parameters. This instability would likely cause large non-monotonic variations in fit parameters for different centralities, so smooth centrality trends would show that this effect is minimal. Regardless, two different approaches were taken to study this affect.

In one test the fitting process was broken into two stages. First, only the away-side bins were fit with the dipole, quadrupole, and 1D Gaussian. These components were subtracted from the SS region which was then fit with the 2D Gaussian and exponential. This two-stage fit manually decouples any possible covariance between the dipole and 2D Gaussian. The results were entirely consistent within errors with the original fits.

In the second test, the dipole was removed from the fit function and replaced with a 1D Gaussian on $\phi_\Delta = 0$ and another at $\phi_\Delta = \pi$. To ensure periodicity the $\phi_\Delta = 0$ Gaussian was copied to other even multiples of π, and similarly the $\phi_\Delta = \pi$ Gaussian was copied to odd multiples of π. Again, fits to the data recovered

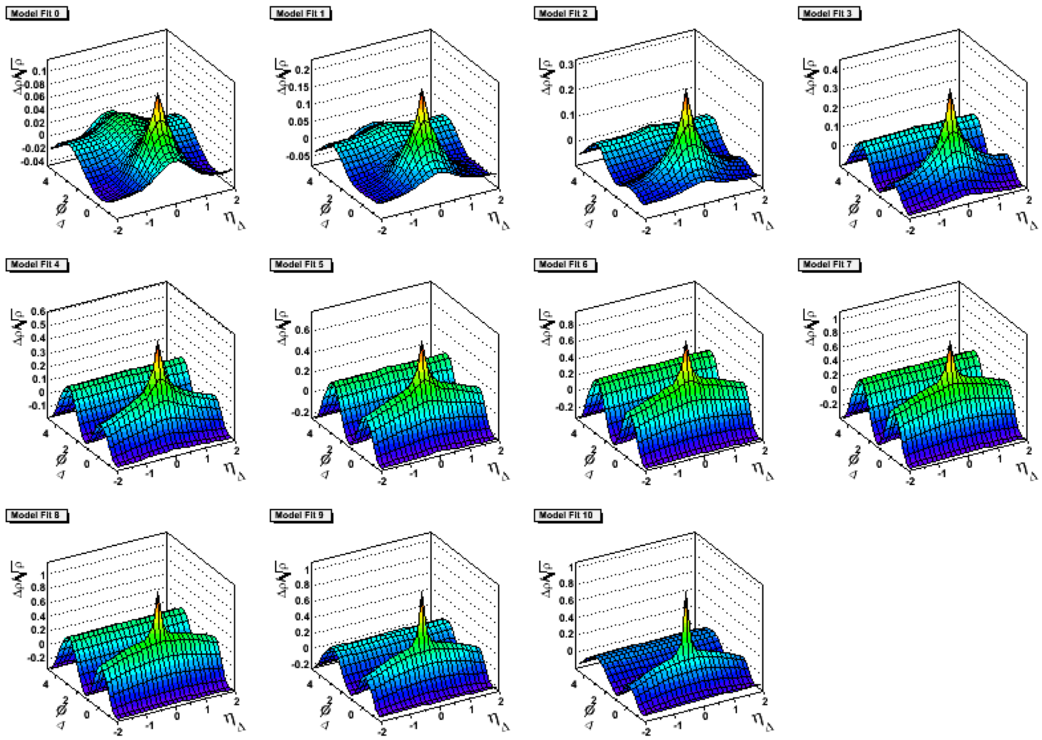

Figure 6.5: Model fits of 200 GeV data in figure 6.3.

the original fit values for all remaining parameters, while the trial Gaussians and constant offset (A_3) conspired to accurately reproduce the dipole component of the original fits.

6.3 Fit Results

Figure 6.5 gives the results of fitting the 200 GeV data from figure 6.3 with the function in figure 6.1. The fit residuals defined as the data minus the model fit are shown in figure 6.6. These figures illustrate that this fit function, which was constructed from the p+p fit components with a single additional quadrupole term, describes the data well. There are no remaining structures in the residual which are

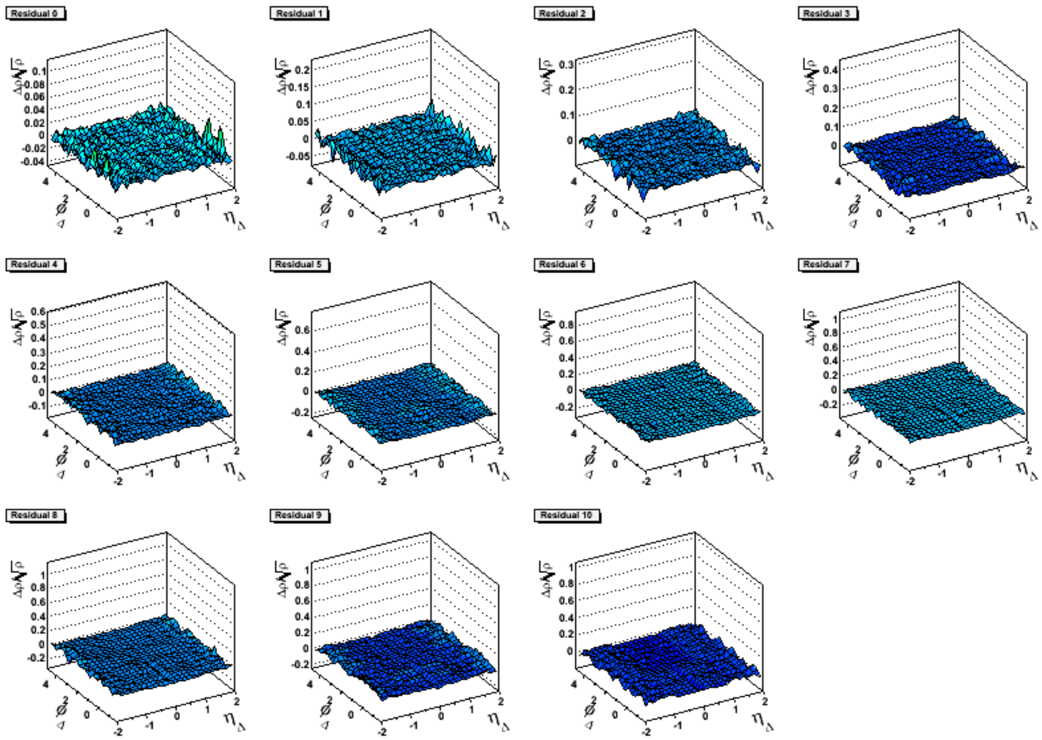

Figure 6.6: Residuals from model fits in previous figure.

large compared to the statistical noise. The residuals at 62 GeV are not shown, but are comparable to those in figure 6.6.

The fit parameters are listed in tables 6.1 and 6.2, and are also shown in figure 6.7 for 62 GeV (red points) and 200 GeV (black points) where centrality is measured by geometrical path length ν at 200 GeV. The top row of the tables list centrality as cross section fraction. The bottom section of each table also lists several other measures of centrality. The first is $dN_{ch}/d\eta$ estimated as corrected charged particle multiplicity per unit pseudorapidity measured at mid-rapidity. The second is geometrical path length $\nu \equiv 2N_{bin}/N_{part}$ also used in figure 6.7 (to aid in comparison the values of ν for 200 GeV are used for both data sets). N_{part} is listed

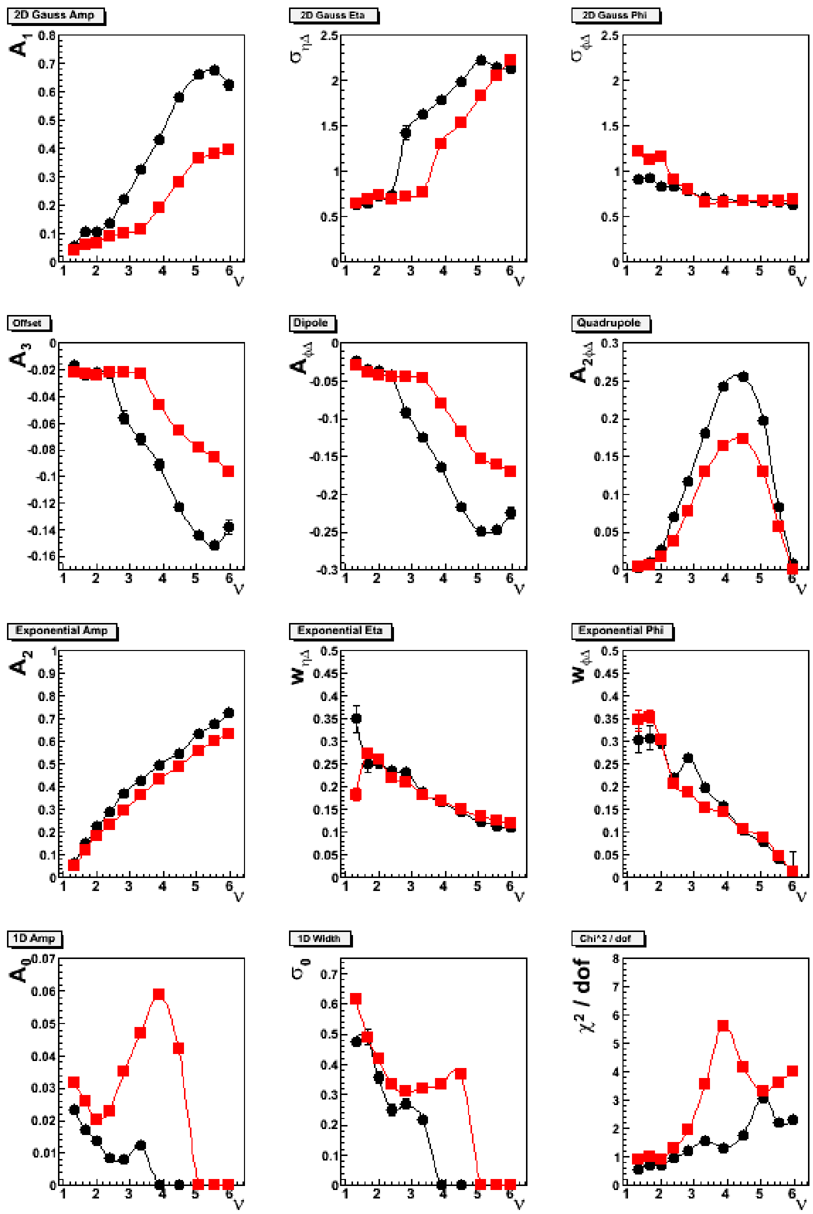

Figure 6.7: Fit parameters for 62 GeV (red) and 200 GeV (black) Au+Au collisions. First row: 2D Gaussian amplitude A_1 and widths σ_{η_Δ}, σ_{ϕ_Δ}. Second row: Offset A_3, dipole A_{ϕ_Δ}, quadrupole $A_{2\phi_\Delta}$. Third row: Exponential amplitude A_2 and widths w_{η_Δ}, w_{ϕ_Δ}. Last row: 1D Gaussian amplitude A_0 and width σ_0, χ^2 per degree of freedom.

next in the table. Transverse particle density, defined as

$$\tilde{\rho} \equiv \frac{3}{2}\frac{dN_{ch}}{d\eta}/\langle S\rangle, \tag{6.2}$$

calculates the density of final state particles per unit η, also using the factor 3/2 to account for neutral hadrons, per initial collision overlap area $\langle S\rangle$. This overlap was estimated as $\langle S\rangle = \pi R^2$ where R is an effective transverse system radius in the initial collision stage given by $0.95N_{part}^{1/3}$ normalized to Monte Carlo Glauber model calculations from [64] and [67], which agree within 10% for more-central collisions. The same overlap areas were adopted for both collision energies.

The final row is each table lists the Bjorken energy density [65],

$$\epsilon_{Bj} = \frac{dE_t}{dy}/\langle S\rangle c\tau, \tag{6.3}$$

where E_t is transverse energy and τ is the formation time. In this equation $\frac{dE_t}{dy}$ measures the energy of a system with volume $\langle S\rangle c\tau$, where $c\tau$ estimates the longitudinal size of a system that is expanding at the speed of light. Bjorken energy density is intended to characterize a longitudinally expanding, equilibrated system. Although the RHIC data do not confirm a system in thermodynamic equilibrium, the quantity in figure 6.3) can be calculated nevertheless. To obtain numerical values for $\epsilon_{Bj}c\tau$, measured $dE_t/d\eta$ data for 200 GeV Au+Au collisions from STAR [66] was used along with an interpolation of 62 GeV data from PHENIX measurements at 20, 130, and 200 GeV [67]. The previous estimates of overlap area $\langle S\rangle$ were used. Formation time τ is very difficult to estimate as it is highly model-dependent and extremely sensitive to input parameters, therefore it is standard practice to simply report the product $\epsilon_{Bj}c\tau$. Motivations for examining transverse particle density and Bjorken energy density will be discussed below.

6.4 Discussion

6.4.1 Semi-hard scattering

Components

Four of the fit parameters shown in figure 6.7 are related to semi-hard scattering and minijet fragmentation, including The first row shows the 2D Gaussian peak amplitude A_2 and widths σ_{η_Δ} and σ_{ϕ_Δ} for 62 GeV (red points) and 200 GeV (black points) Au+Au collisions. The amplitude shows a gradual increase from the most peripheral events ($\nu \sim 1$) for several centrality bins. A sudden departure from this trend is observed at approximately 55% centrality in 200 GeV and 40% in 62 GeV where the amplitude increases more rapidly. The growth is nearly linear with ν until the most central events. The η_Δ width of this peak shows much more dramatic behavior. These widths show a very slight increase from peripheral to mid-central then depart from this trend at the same centralities where the amplitude begins rapidly increasing. This point of departure appears to mark an energy-dependent transition from one behavior to another. The σ_{η_Δ} widths nearly double at the transition point and continue to increase quickly. The 200 GeV data show a slight decrease in amplitude η_Δ width for the two most central bins. The ϕ_Δ width shown in the right panel has very different behavior. σ_{ϕ_Δ} follows a near-monotonic decrease with centrality with no change in behavior at the transition point.

The first panel in the second row of figure 6.7 shows the constant offset A_3. While not directly related to semi-hard scattering, this term accounts for the overall normalization of the histograms by becoming increasingly negative in more central collisions to offset positive correlations. As such, the offset mirrors the centrality trends of the 2D Gaussian amplitude which is the largest correlation structure observed in these data (the sinusoids do not contribute to the normalization). As discussed in chapter 4 the offset may be connected to multiplicity fluctuations, however the values are very sensitive to centrality bin width and the measurement conveys much less information than the autocorrelations.

The next panel in the second row gives the dipole amplitude A_{ϕ_Δ}, which measures the away-side ridge associated with semi-hard scattering. Additionally, global momentum conservation of the entire system produces a dipole autocorrelation as $\vec{p}_{t1} \cdot \vec{p}_{t2} = p_{t1} p_{t2} \cos(\phi_\Delta)$ [68]. This is estimated to contribute approximately between 0.015 and 0.02 to the dipole amplitude at both energies for all centralities. Therefore roughly half of the dipole in peripheral events may be due to global momentum conservation, though in central collisions this contribution in insignificant compared to the local momentum conservation from semi-hard scattering. The dipole neatly mirrors the centrality behavior of the 2D Gaussian amplitude further supporting the connection of the dipole to semi-hard scattering. Section 6.2.2 determined that this is not due to an artifact in the fitting procedure, instead the semi-hard scattering which produces a same-side minijet peak also produces a dipole to conserve momentum.

Expectations

It is important to consider what the expected centrality trends are for minijet production. In a heavy ion collision each interacting nucleon may undergo several successive collisions, as measured by path length ν, meaning that Au+Au systems trivially contain a larger fraction of semi-hard scattering than p+p systems, and that this fraction increases with centrality. This scaling is often not accounted for, particularly in studies of single-particle spectra, though the effect is easy to calculate. Using the two-component formalism, the multiplicity density in ion collisions is

$$\frac{dn_{ch}}{d\eta} = (1-x) n_{pp} \frac{\langle N_{part} \rangle}{2} + x n_{pp} \langle N_{bin} \rangle \tag{6.4}$$

$$= \frac{\langle N_{part} \rangle}{2} n_{pp}[1 + x(\nu - 1)] \tag{6.5}$$

by the definition of ν. Assume that the minijet production scales with N_{bin}. Then the minijet correlation amplitude should scale with N_{bin}/n_{ch} for a per-particle correlation measure. If correlation amplitude A_{pp} is measured in p+p collisions, then the expectation for heavy ion collisions is

$$A(\nu) = A_{pp} \, N_{bin}/n_{ch} \tag{6.6}$$

$$= A_{pp} \frac{\nu}{[1 + x(\nu - 1)]} \tag{6.7}$$

using equation 6.5. This model assumes independent binary interactions, so while the minijet amplitudes increase the widths of the minijet peak should remain constant.

Figure 6.8 compares the minijet parameters, measured as the fits of the same-side 2D Gaussian, to the binary scaling reference of 6.7. The amplitudes are shown in the first panel for 62 GeV (red) and 200 GeV (black) compared to binary scaling shown as dotted and dashed blue lines for 62 and 200 GeV respectively. The choice of centrality measure for the horizontal axis will be discussed below. Similarly, the center panel shows the η_Δ width of the 2D Gaussian, and the right panel shows the 2D Gaussian volume ($= 2\pi A_1 \sigma_{\eta\Delta} \sigma_{\phi\Delta}$). The agreement of the data with binary scaling is excellent for peripheral events. The amplitudes follow binary scaling closely, while the η_Δ widths show a very slight increase above the expected behavior. The data and binary scaling trends diverge sharply at the transition point.

Implications

The correspondence between the data and binary scaling in peripheral collisions indicates that the minijets observed in p+p collisions are also being observed in Au+Au. However, above the transition point the correlation structures are very

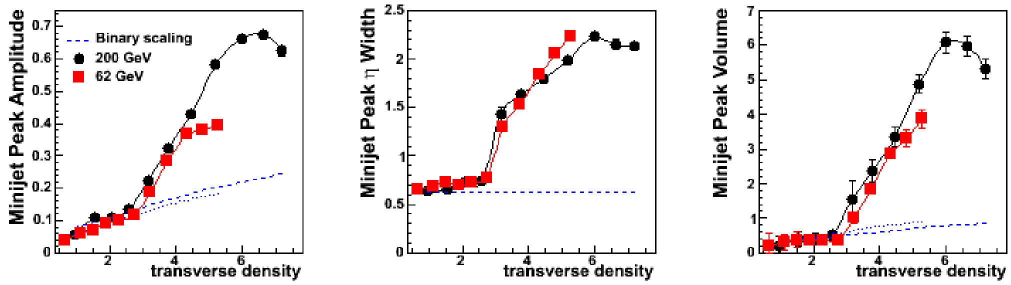

Figure 6.8: The same-side peak amplitude, η_Δ width, and volume for 62 GeV (red points) and 200 GeV (black) as a function of transverse particle density. The blue lines show binary scaling expectations for 62 GeV (dotted line) and 200 GeV (dashed line).

different, but are still likely to be associated with minijets for several reasons. First, these results, particularly when compared with a similar analysis of p_t correlations [31], show that contributions from a new physical mechanism unrelated to minijets are unlikely. Any such hypothetical process must have ϕ_Δ widths and p_t correlations that match seamlessly with minijets, which would be a remarkable coincidence. Second, the amplitude and η_Δ width increases are consistent with further minijet interactions, which may be possible due to path-length considerations [69]. Finally, it is possible that the new correlation structures are due to changes in minijet fragmentation. A minijet from a nucleon-nucleon collision is essentially produced *in vacuo*, whereas a minijet produced in a RHIC heavy ion collision can be embedded is the densest matter ever produced in a laboratory. Thus it is reasonable to expect some kind of modifications in minijet production. Considering all of these factors we hypothesize that the same-side correlations observed above the transition are still due to minijets, and the change in structure represents a modified minijet rather than an unrelated mechanism.

It is also instructive to calculate the number of particles associated with the modified minijet peaks. The large excess in amplitude and η_Δ contribute to a roughly factor of eight increase in volume over binary scaling at the highest point. Since $\frac{\Delta\rho}{\sqrt{\rho_{ref}}}$ measures number of correlated pairs per particle the volume measurements of the minijet peak times the multiplicity gives the number of pairs—about 7,180 in central 200 GeV. Due to the combinatorics of pair counting, we must estimate the number of individual minijet structures per event to convert number of pairs to number of particles, so the calculation requires many steps. The average number of minijets per event is estimated as $2 * 0.0125 * N_{bin}$ based on the probability of 0.0125 of observing a minijet per unit η in a p+p collision. This works out to about 26 minijets per event at central 200 GeV, and 7,180 / 26 = 276 pairs per minijet on average. Taking the square root gives 17 particles per minijet. Multiplying by the number of minijets and dividing by the total multiplicity, we see that approximately 30% of all particles in central 200 GeV Au+Au collisions are related to minijets. An independent analysis of single-particle spectra [38] discussed in chapter 3 also finds that approximately 1/3 of all particles are associated with the semi-hard component, showing excellent agreement between the two estimates.

Scaling

Centrality is shown in figure 6.8 as transverse particle density defined in equation 6.2. The primary goal of this analysis is to study deviations from expected behavior observed in p+p collisions which would indicate new physics accessible at RHIC. It is natural to question if these deviations occur due to interactions with surrounding particles, and transverse particle density provides an intensive estimate of the environment experienced by each particle. Figure 6.8 shows an apparent scaling of minijet correlations with transverse density. This scaling may suggest that the transition point is then a critical density of particles, and beyond this critical point particles undergo stronger interactions. A much more rigorous test of this scaling will be provided by comparing different beam ion species rather than the same ions at different energies. The Cu+Cu data from RHIC run 5 will add this crucial information.

Transverse particle density may be converted into Bjorken energy density (equation 6.3) by estimating mean transverse energy per particle, or measuring transverse energy in a calorimeter, and longitudinal system size. The latter quantity is usually determined based on a system expanding at the speed of light for a certain formation time τ. The formation time cannot be measured directly, instead it is inferred based on a number of model calculations. The large uncertainty in τ, and more importantly the unknown energy dependence of τ made it a poor choice to use for comparing the 62 and 200 GeV data in this analysis. Additionally, Bjorken energy density is intended to be used for systems in thermodynamic equilibrium, a picture which is often at odds with experimental results particularly several discussed in chapter 3. However, taking the standard estimate of $\tau = 1$ fm/c for both energies shows a scaling very similar to the scaling observed in transverse particle density with a transition point at approximately 2.2 GeV / unit rapidity / fm^3.

6.4.2 Quadrupole

Returning to the other fit components shown in figure 6.7, the last panel on the second row shows the quadrupole amplitude $A_{2\phi_\Delta}$ which measures an azimuthal anisotropy of particle distributions. The amplitude approaches zero at peripheral and central collisions. The 62 and 200 GeV have similar centrality trends but an approximate factor of 1.5 difference in amplitude for all centralities. The Wiener-Khinchin theorem, as discussed in [52], relates the autocorrelation to power-spectrum elements in a Fourier transformation. This relation directly connects the quadrupole amplitude to elliptic flow measure v_2 [49], defined as the second Fourier component in the ϕ distribution relative to the event plane (plane determined by the beam axis and impact parameter). A large number of v_2 measures exist, each implementing different strategies for dealing with the event plane and separating the signal (referred to as "flow") from the large correlated background ("non-flow") [70]. The analysis here addresses both of these problems. First, autocorrelation methods do not require the determination of an event plane [52]. Algebraically, the event plane becomes a phase angle in the azimuthal distribution which is averaged out in the autocorrelation. Second, conventional v_2 measures only use 1D azimuthal information to attempt to remove all "non-flow" correlations. This analysis examines the 2D correlations and is able to use the η-dependence to isolate the quadrupole from all other terms. A final benefit is that this analysis is able to make accurate measures at all centralities regardless of event multiplicities due to careful construction of the correlation measure, whereas conventional v_2 measures are limited in centrality range. Figure 6.9 shows one comparison of quadrupole amplitudes measured in this analysis for 200 GeV collisions converted to v_2 (the notation $v_2\{2D\}$ is commonly used to distinguish this from other v_2 measures). The quadrupole amplitude is equal to $\frac{\bar{n}v_2^2\{2D\}}{4\pi}$ [52]. The black points in the figure represent this conversion in comparison to other methods. The detailed study of and implications of this method is the subject of an ongoing analysis.

6.4.3 Exponential Peak

The third row of figure 6.7 shows the parameters of the sharp 2D exponential peak. Due to the contamination of electron-positron pairs and residual pair inefficiencies reliable measurements cannot be made at very small opening angles. Comparing LS to US pairs shows that HBT [42] makes a much smaller contribution to the same-side peak than semi-hard scattering in this analysis. The effect of HBT is maximized by projecting correlated LS particles onto relative momentum difference. The consequence of these factors is that whereas these results add new insight to conventional v_2 analyses, they do not offer an improved method of examining HBT.

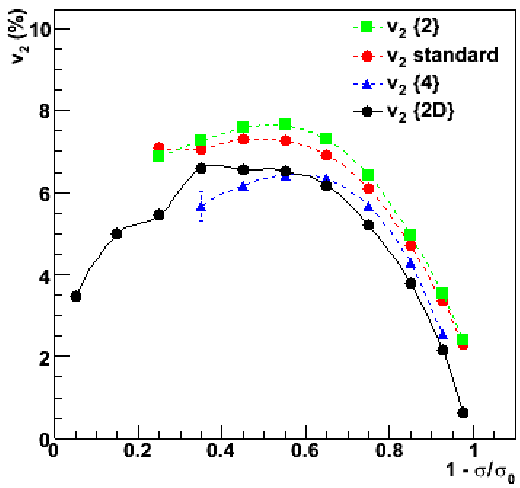

Figure 6.9: Comparison of quadrupole amplitude at 200 GeV transformed to v_2 (black points) along with the two-particle (green), event plane (red), and four-particle (blue) v_2 measures [70].

Therefore, the exponential peak in this analysis is treated as a background instead of a physics measurement.

The amplitudes in figure 6.7 show a very smooth increase with centrality, providing evidence that the exponential and Gaussian peaks are being distinguished correctly. The amplitudes show a slight energy dependence where the 200 GeV data are roughly 10% higher than the 62 GeV data. The widths show that the exponential peak is approximately symmetric on η_Δ and ϕ_Δ, though showing a slight elongation in η_Δ in central collisions. The decrease in widths with increasing centrality reflects the increase in HBT source size.

As a final test of modeling this structure, correlation data from previously published HBT analyses were converted into $\frac{\Delta\rho}{\sqrt{\rho_{ref}}}(\eta_\Delta, \phi_\Delta)$. The exponential peak in the fit function was replaced with the HBT structures from these conversions scaled by an adjustable amplitude. Both approaches yielded consistent results for the other eight fit parameters.

6.4.4 Longitudinal Fragmentation

The amplitude of the 1D Gaussian, left panel in the bottom row of figure 6.7, shows the most energy dependence of any fit parameter. Contrary to other terms, the amplitude is much greater at 62 GeV than 200 GeV for most centralities. This amplitude shows a non-monotonic centrality dependence not seen in other correlations. Charge-dependent studies of LS, US, and CD correlations, discussed in the next chapter, suggest that two distinct physical mechanisms contribute: a charge-dependent component (larger amplitude in US than LS pairs) which monotonically decreases with centrality, and a charge-independent component (appearing equally in LS and US pairs) which is small in peripheral and central collisions but large at mid-centrality.

The Gaussian widths also support this observation. The charge-dependent component is wider than the charge-independent component. Therefore σ_0 is largest in the most peripheral events where the charge-dependent component dominates. Then the measured width decreases with centrality and becomes approximately flat where the charge-independent term is dominant.

The 1D Gaussian observed in p+p collisions is charge-dependent and well-described by the phenomenological Lund string model [44], where local charge conservation during longitudinal fragmentation generates a correlation. This structure is also observed in peripheral Au+Au collisions with an amplitude that diminishes with centrality. It is not clear why this correlation should be absent in central collisions. The additional charge-independent contribution to this 1D Gaussian is entirely unexpected. This component has the puzzling energy and centrality dependence as the amplitude is approximately five times larger in 62 GeV than at 200 GeV at the peak, which then shows a sharp cut-off in more central events.

6.5 Comparison with 130 GeV

Figure 6.10 shows the fit parameters exactly replotted from figure 6.7 with the addition of the 130 GeV results from [48] as green triangles. In this figure the point markers have been removed from the 62 GeV (red) and 200 GeV (black) data sets to show the underlying error bars often not visible in figure 6.7. Also, the vertical scale of σ_0, the 1D Gaussian width, in the bottom row was enlarged to accommodate the new point.

Nominally, one would expect the 130 GeV results to fall in between the 62 and 200 GeV results, however there are three significant differences in the analyses. First, the 130 GeV analysis imposes an upper p_t limit of 2.0 GeV/c. While this only excludes a small number of particles, these particles are strongly correlated. Second, a pair cut was used to suppress HBT and Coulomb correlations. Since these additional correlated pairs have been removed, the fit function did not include the 2D exponential peak. Finally, the fit procedure was slightly different as the away-side components were fit first, followed by the SS components. This procedure is the same as the two-stage fit discussed in section 6.2.2 which was found to have no significant effect for the 62 and 200 GeV data other than increased fit parameter errors.

To study the effects of these differences, the 130 GeV correlation data were re-fit using exactly the same method as for the 62 and 200 GeV data. The quadrupole and σ_{ϕ_Δ} agreed at all centralities. The other components associated with hard scattering (offset, dipole, and 2D Gaussian amplitude and η_Δ width) increased by roughly 25%. Even with this increases these components still had smaller amplitude than the 62 GeV data, most likely due to the lower p_t range and additional pair cut. The 1D Gaussian was in agreement for all but the most peripheral bin, where instead of the extremely wide structure in the original analysis the fit closely matched the 62 GeV data in this centrality range. Finally, a small 2D exponential was added

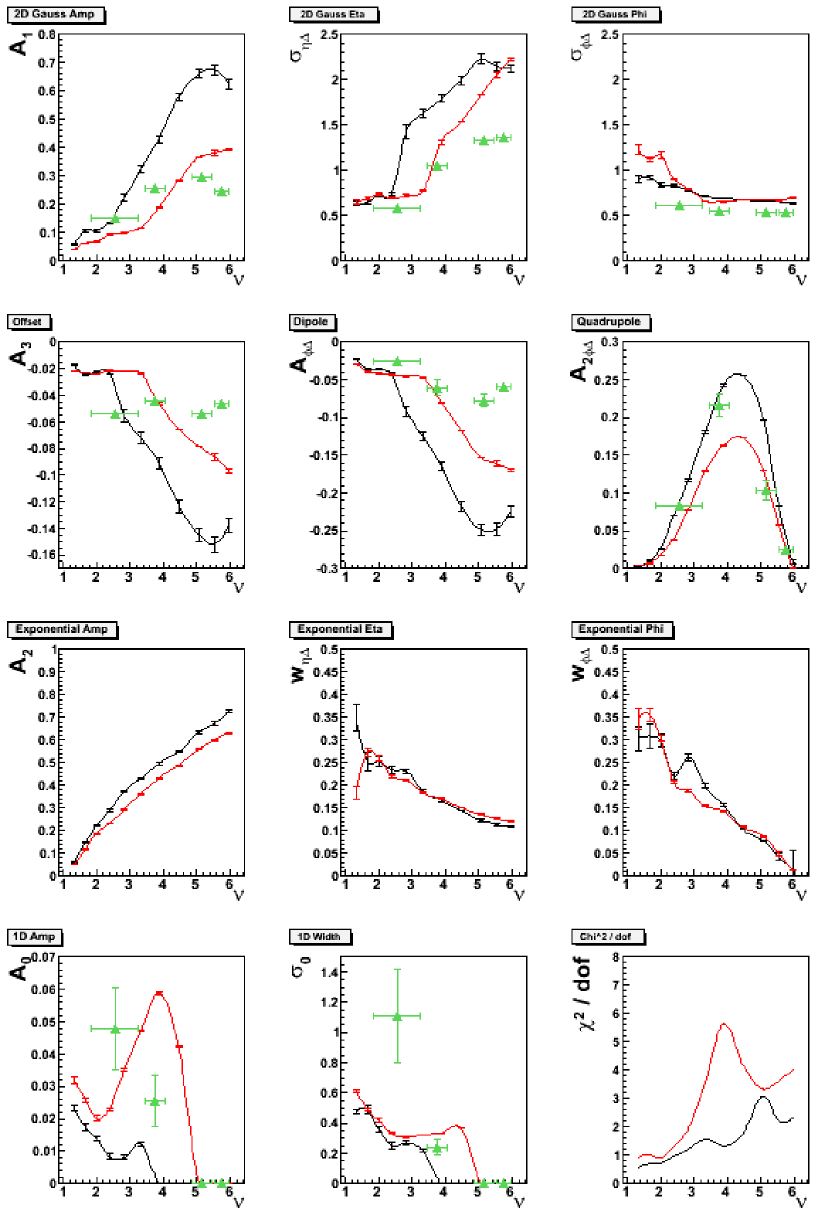

Figure 6.10: Same as figure 6.7, except that the 130 GeV data (green) have been added. The data symbol size was reduced for the 62 GeV (red) and 200 GeV (black) points to better reveal the fitting error bars.

with an amplitude of approximately 1 for all centralities.

It is interesting to note that when tracing through the history of the 130 GeV analysis we found that one of the preliminary fits to the data (called fit “five” of ten total fits) was in excellent agreement with these 62 and 200 GeV results. Unfortunately we were unable to determine what changes had taken place between this preliminary fit and the final published results, which may include changes in the analysis, cut parameters, and/or fitting procedure.

6.6 HIJING Predictions

The HIJING simulation model was originally designed to study minijets in heavy ion collisions [37]. One million 200 GeV Au+Au collisions were simulated using HIJING 1.382 with default parameters for each of three settings: jets off, jet quenching off, and jet quenching on. Only hadrons within an acceptance range equivalent to STAR's TPC were used in the analysis. The jets off simulations bear little resemblance to data, however they provide a test of the analysis method and fit model. These simulations showed only a dipole and a 1D Gaussian of approximately equal magnitude with no other components in the correlation structures. The 1D Gaussian width varied from 1.5 to 2.0; much broader than observed in real data.

The HIJING quench off simulations include minijets which undergo no additional interactions after the initial fragmentation. This model simulates the binary scaling principle by modeling a series of independent nucleon-nucleon collisions. In this way the quench off simulations provide the best reference with which to compare real data, as shown in figure 6.11. Fits to HIJING simulations are shown as green triangles alongside the real 200 GeV data from figure 6.7 as black points. The dashed blue lines show binary scaling extrapolations for the HIJING 2D Gaussian parameters in the top row of figure 6.11. The excellent agreement verifies the extrapolation procedure. No transition is observed in HIJING confirming that trivial

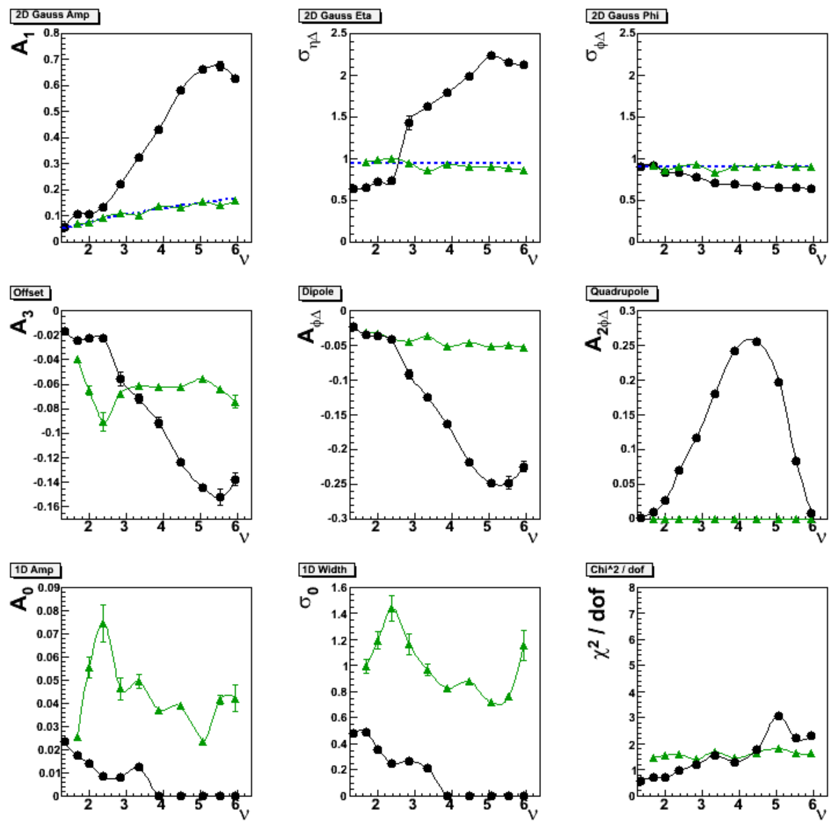

Figure 6.11: HIJING simulations of 200 GeV collisions (green triangles) compared to data (black points). Dashed blue lines show binary scaling extrapolations of HIJING.

overlapping of minijets does not cause this phenomenon. The quadrupole fits are consistent with zero for all centralities. The HIJING model does not include HBT or final-state interactions, and consequently HIJING does not show a sharp peak at the origin. A 2D exponential peak was included in preliminary fits and amplitudes were extremely small, though with large error. Since this structure was not present in the correlations this term was ultimately excluded from the fit to remove any potential instabilities. The last row of figure 6.11 shows that the 1D Gaussian is largely over-predicted in HIJING both in amplitude and width. The fit parameters are also listed in table 6.4. In general, the default parameters of HIJING are tuned to match single-particle spectra. It is likely that the model could be tuned to agree somewhat well with real data below the transition, excepting the quadrupole and HBT, however HIJING is much less relevant in central collisions.

An *ad hoc* jet quenching model has been added to HIJING as an attempt to more closely resemble RHIC data. The energy loss from a minijet traveling through the collision system is modeled with gluon bremsstrahlung and a dE/dz energy loss parameter. The points where gluons are radiated are found by the probability $dP = \frac{d\ell}{\lambda} e^{-\ell/\lambda}$ for mean free path λ and distance ℓ since last interaction. The induced radiation $\Delta E(\ell) = \ell dE/dz$ is subtracted from the minijet. By default dE/dz is taken as 2 GeV/fm for a gluon jet and 1 GeV/fm for a quark jet. In this analysis, including this quenching mechanism causes the correlations to deviate further away from the data. Fits revealed that the amplitude of the 2D Gaussian decreases slightly below binary scaling with a small broadening in both the η_Δ and ϕ_Δ widths. The 1D Gaussian increased hugely to amplitudes of roughly 4, thus becoming much larger than the minijet amplitude, with widths around 2.5. Apparently, this quenching mechanism is a step backwards in accurately modeling real data.

Overall, these HIJING tests have been useful in validating the analysis and fitting procedures as well as providing more evidence for the correspondence of fit components with physical mechanisms. The simulations confirm the two-component binary scaling extrapolation with a more realistic approach. HIJING shows that even if every single minijet produced is detected, the correlation amplitude is still a factor of four smaller than real data for central collisions. However, the lack of agreement with data in other correlation components limits the usefulness of HIJING, though these minimum-bias correlation analyses could be extremely valuable in tuning HIJING to match real data.

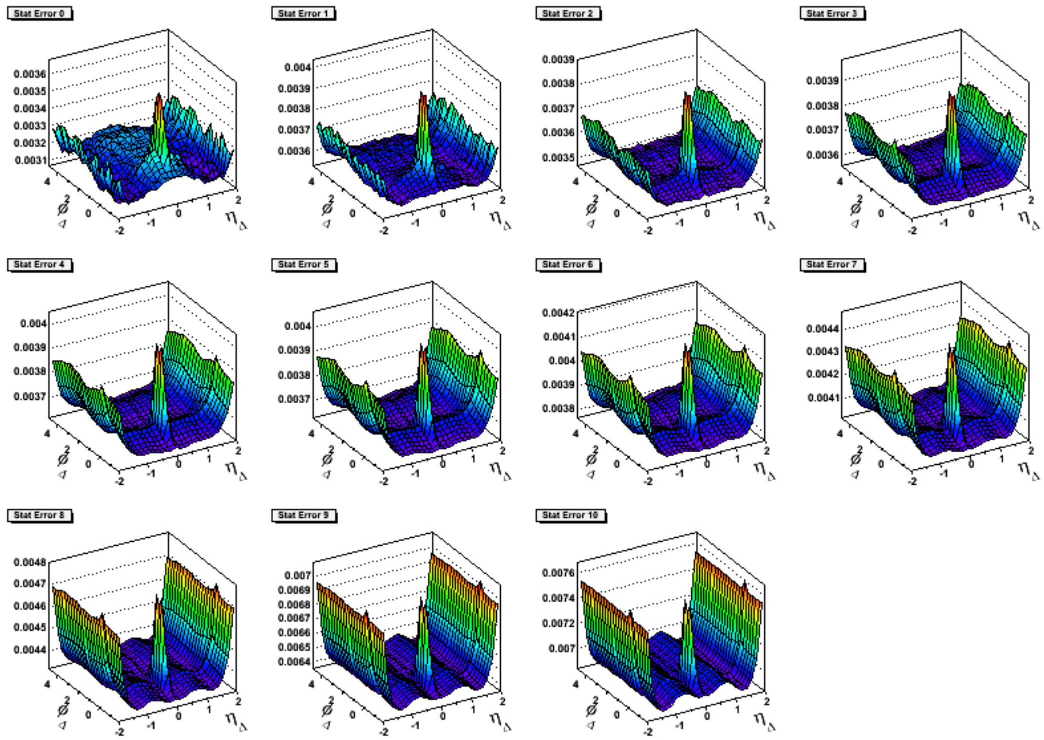

Figure 6.12: Statistical error distribution in 200 GeV correlations.

6.7 Errors

The statistical error distribution of the measured autocorrelations is shown in figure 6.12 for the 200 GeV data in all centrality bins. Within each histogram, the error is maximal for large $|\eta_\Delta|$ and in the SS region affected by pair cuts. The average error generally increases linearly with centrality from approximately 0.0032 in peripheral bins to 0.0045 to the 10-20% (uncorrected) bin, and then jumps to 0.0066 and 0.0071 for the narrower 5-10% and 0-5% bins respectively. For the 62 GeV statistical errors (not shown), the distributions on $(\eta_\Delta, \phi_\Delta)$ are very similar, though the overall amplitude is reduced by half due to the larger number of events.

Fit parameters errors reported by ROOT take into account these statistical errors as well as any uncertainties during minimization. A test computing asymmetric error bars showed no significant difference from the original parabolic errors. These errors are shown in all figures of fit parameters and listed in table 6.3.

The dominant source of systematic error is caused by the contamination of non-primary particles in the data sample due to weak decays and interactions with the detector material. The distance of closest approach (DCA) cut of less than 3 cm away from the reconstructed event vertex, as discussed in chapter 5, includes an approximately 12% background contamination [71, 64] to the true primary hadrons. The potential error was estimated by studying the dependence of $\frac{\Delta\rho}{\sqrt{\rho_{ref}}}$ on the DCA cut. When varying the amount of background by lowering DCA cut from 3 to 1 cm no significant change within statistics was observed in the correlations, resulting in a 5% upper limit on systematic error of correlation amplitudes due to background contamination. The efficiency correction included in the prefactor $\sqrt{\rho'_{ref}}$ defined in chapter 4 adds a $\pm 8\%$ uncertainty in the amplitudes at 62 GeV and $\pm 7\%$ in 200 GeV [64, 71]. Other sources of systematic error including photon conversions, two-track inefficiencies, intermittent electronics outages, collision vertex position dependence in the TPC, etc. [61]) add a few percent error near $(\eta_\Delta, \phi_\Delta) = (0, 0)$. The total systematic errors for the 62 and 200 GeV data combined in quadrature are $\pm 9\%$ of the overall correlation amplitudes at both energies. These systematic errors are not included in table 6.3.

Table 6.1: Model fit parameters for 200 GeV Au+Au collisions from most-peripheral (left column) to most-central (right column). The upper portion contains parameter names as defined in the fit function (equation 6.1). The volume of the 2D same-side Gaussian is also listed. The lower portion contains additional centrality information including corrected multiplicities, Monte Carlo Glauber centrality measures ν and N_{part}, and the transverse particle and Bjorken energy densities (defined in text).

200 GeV Au+Au

centrality(%)	84-93	74-84	64-74	55-64	46-55	38-46	28-38	18-28	9-18	5-9	0-5
A_{ϕ_Δ}	-0.023	-0.036	-0.036	-0.042	-0.092	-0.125	-0.164	-0.218	-0.249	-0.248	-0.224
$A_{2\phi_\Delta}$	0.002	0.011	0.026	0.070	0.117	0.180	0.242	0.256	0.197	0.083	0.008
A_0	0.023	0.017	0.014	0.008	0.008	0.012	0.000	0.000	0.000	0.000	0.000
σ_0	0.476	0.490	0.358	0.250	0.269	0.217	–	–	–	–	–
A_1	0.058	0.107	0.108	0.135	0.223	0.325	0.430	0.581	0.663	0.676	0.625
σ_{η_Δ}	0.635	0.651	0.721	0.736	1.428	1.631	1.789	1.988	2.231	2.153	2.128
σ_{ϕ_Δ}	0.904	0.923	0.839	0.835	0.778	0.709	0.693	0.671	0.654	0.655	0.635
volume	0.210	0.404	0.409	0.520	1.558	2.359	3.348	4.873	6.074	5.985	5.312
A_2	0.061	0.149	0.223	0.289	0.373	0.428	0.497	0.547	0.635	0.675	0.727
w_{η_Δ}	0.350	0.252	0.253	0.235	0.231	0.187	0.167	0.143	0.123	0.113	0.109
w_{ϕ_Δ}	0.303	0.309	0.299	0.221	0.263	0.199	0.157	0.103	0.077	0.042	0.013
A_3	-0.017	-0.024	-0.022	-0.023	-0.056	-0.072	-0.091	-0.123	-0.145	-0.152	-0.137
$dN_{ch}/d\eta$	5.2	13.9	28.8	52.8	89	139	209	307	440	564	671
ν	1.40	1.68	2.00	2.38	2.84	3.33	3.87	4.46	5.08	5.54	5.95
N_{part}	4.6	10.5	20.5	36.0	58.1	86.4	124.6	176.8	244.4	304.1	350.3
$\tilde{\rho}$	1.00	1.54	2.05	2.58	3.16	3.78	4.46	5.19	5.98	6.63	7.19
$\epsilon_{Bj} c\tau$	1.03	1.44	1.78	2.18	2.64	3.09	3.60	4.18	4.75	5.17	5.45

Table 6.2: Same as table 6.1 except for 62 GeV Au+Au collisions.

62 GeV Au-Au

centrality(%)	84-95	75-84	65-75	56-65	46-56	37-46	28-37	18-28	9-18	5-9	0-5
A_{ϕ_Δ}	-0.029	-0.039	-0.041	-0.044	-0.045	-0.047	-0.081	-0.117	-0.154	-0.160	-0.170
$A_{2\phi_\Delta}$	0.004	0.007	0.017	0.038	0.078	0.129	0.163	0.173	0.129	0.057	0.000
A_0	0.032	0.026	0.020	0.023	0.035	0.047	0.059	0.042	0.000	0.000	0.000
σ_0	0.615	0.489	0.417	0.332	0.309	0.320	0.332	0.367	–	–	–
A_1	0.041	0.062	0.068	0.093	0.099	0.117	0.190	0.283	0.366	0.382	0.395
σ_{η_Δ}	0.652	0.689	0.734	0.693	0.722	0.776	1.304	1.534	1.835	2.055	2.229
σ_{ϕ_Δ}	1.229	1.123	1.168	0.908	0.798	0.661	0.656	0.670	0.679	0.670	0.697
volume	0.204	0.300	0.368	0.368	0.360	0.376	1.019	1.829	2.863	3.306	3.862
A_2	0.050	0.118	0.185	0.234	0.293	0.362	0.432	0.486	0.561	0.601	0.632
w_{η_Δ}	0.183	0.274	0.260	0.220	0.212	0.183	0.171	0.151	0.136	0.127	0.121
w_{ϕ_Δ}	0.348	0.356	0.305	0.208	0.187	0.155	0.143	0.108	0.088	0.049	0.012
A_3	-0.022	-0.023	-0.024	-0.021	-0.022	-0.023	-0.047	-0.065	-0.078	-0.086	-0.097
$dN_{ch}/d\eta$	3.3	9.3	19.8	36.9	62.8	99.0	149	217	312	403	488
ν	1.34	1.59	1.87	2.22	2.62	3.05	3.49	3.96	4.46	4.82	5.13
N_{part}	4.0	9.3	18.7	33.8	55.7	84.8	122.0	171.6	238.4	297.6	344.6
$\tilde{\rho}$	0.70	1.12	1.49	1.88	2.29	2.73	3.23	3.74	4.32	4.81	5.28
$\epsilon_{Bj} c\tau$	0.67	0.97	1.24	1.53	1.83	2.17	2.52	2.90	3.27	3.55	3.72

Table 6.3: Errors for fit parameters listed in previous tables. Does not include systematic errors discussed in text.

200 GeV Au+Au Parameter Errors

centrality(%)	84-93	74-84	64-74	55-64	46-55	38-46	28-38	18-28	9-18	5-9	0-5
A_{ϕ_Δ}	0.0006	0.0008	0.0009	0.0010	0.0071	0.0058	0.0061	0.0067	0.0074	0.0089	0.0081
$A_{2\phi_\Delta}$	0.0004	0.0004	0.0005	0.0006	0.0020	0.0019	0.0020	0.0005	0.0004	0.0033	0.0030
A_0	0.0009	0.0010	0.0007	0.0008	0.0007	0.0007	0.0000	0.0000	0.0000	0.0000	0.0000
σ_0	0.0144	0.0248	0.0185	0.0205	0.0163	0.0106	–	–	–	–	–
A_1	0.0028	0.0051	0.0044	0.0035	0.0123	0.0107	0.0115	0.0126	0.0139	0.0174	0.0158
σ_{η_Δ}	0.0233	0.0175	0.0198	0.0160	0.0796	0.0483	0.0400	0.0440	0.0484	0.0454	0.0413
σ_{ϕ_Δ}	0.0353	0.0247	0.0170	0.0146	0.0131	0.0081	0.0065	0.0013	0.0010	0.0064	0.0062
volume	0.266	0.193	0.166	0.138	0.513	0.315	0.264	0.288	0.316	0.308	0.280
A_2	0.0049	0.0054	0.0049	0.0043	0.0040	0.0040	0.0041	0.0044	0.0047	0.0070	0.0076
w_{η_Δ}	0.0301	0.0192	0.0115	0.0075	0.0057	0.0034	0.0026	0.0019	0.0017	0.0022	0.0022
w_{ϕ_Δ}	0.0272	0.0256	0.0140	0.0071	0.0071	0.0041	0.0027	0.0023	0.0026	0.0111	0.3870
A_3	0.0004	0.0005	0.0007	0.0007	0.0053	0.0041	0.0043	0.0047	0.0052	0.0060	0.0055

62 GeV Au+Au Parameter Errors

centrality(%)	84-95	75-84	65-75	56-65	46-56	37-46	28-37	18-28	9-18	5-9	0-5
A_{ϕ_Δ}	0.0003	0.0004	0.0004	0.0004	0.0004	0.0006	0.0017	0.0018	0.0020	0.0009	0.0008
$A_{2\phi_\Delta}$	0.0002	0.0002	0.0002	0.0002	0.0002	0.0003	0.0006	0.0002	0.0000	0.0014	0.0002
A_0	0.0012	0.0008	0.0009	0.0004	0.0004	0.0003	0.0003	0.0003	0.0001	0.0000	0.0000
σ_0	0.0102	0.0087	0.0118	0.0051	0.0030	0.0021	0.0016	0.0024	–	–	–
A_1	0.0012	0.0018	0.0014	0.0012	0.0014	0.0012	0.0030	0.0033	0.0036	0.0015	0.0014
σ_{η_Δ}	0.0181	0.0139	0.0129	0.0078	0.0091	0.0117	0.0220	0.0242	0.0266	0.0148	0.0134
σ_{ϕ_Δ}	0.0506	0.0284	0.0319	0.0099	0.0081	0.0045	0.0046	0.0012	0.0001	0.0050	0.0021
volume	0.338	0.199	0.217	0.079	0.077	0.079	0.143	0.154	0.169	0.098	0.086
A_2	0.0018	0.0021	0.0018	0.0018	0.0020	0.0021	0.0020	0.0020	0.0003	0.0031	0.0031
w_{η_Δ}	0.0134	0.0098	0.0056	0.0033	0.0028	0.0019	0.0014	0.0010	0.0001	0.0012	0.0010
w_{ϕ_Δ}	0.0223	0.0137	0.0070	0.0034	0.0028	0.0021	0.0016	0.0012	0.0001	0.0047	0.0001
A_3	0.0002	0.0003	0.0004	0.0003	0.0003	0.0004	0.0011	0.0012	0.0014	0.0007	0.0007

Table 6.4: Model fit parameters for 200 GeV Au+Au HIJING simulations from most-peripheral (left column) to most-central (right column). Default parameters are used with pet production on, but no jet quenching.

200 GeV Au+Au HIJING Quench-off Simulations

centrality(%)	80-100	70-80	60-70	50-60	40-50	30-40	20-30	10-20	5-10	0-5
A_{ϕ_Δ}	-0.031	-0.033	-0.040	-0.044	-0.037	-0.051	-0.046	-0.053	-0.051	-0.053
$A_{2\phi_\Delta}$	0.0018	0.0028	0.0034	0.0043	0.0037	0.0035	0.0038	0.0032	0.0055	0.0009
A_0	0.025	0.056	0.075	0.046	0.049	0.037	0.039	0.023	0.042	0.042
σ_0	1.00	1.20	1.44	1.16	0.97	0.83	0.88	0.72	0.76	1.16
A_1	0.070	0.076	0.095	0.110	0.104	0.138	0.131	0.154	0.142	0.158
σ_{η_Δ}	1.09	0.98	1.00	0.95	0.85	0.93	0.90	0.91	0.89	0.86
σ_{ϕ_Δ}	0.92	0.86	0.91	0.93	0.84	0.91	0.91	0.93	0.91	0.91
A_3	-0.040	-0.065	-0.091	-0.068	-0.061	-0.063	-0.062	-0.056	-0.064	-0.074
$dN_{ch}/d\eta$	11.7	29.3	57.7	107	179	290	463	688	909	1125

Chapter 7

Charge-Dependent Axial Autocorrelations

This is the first of two chapters covering preliminary results. Though the analyses are not final, these correlation structures provide some additional insight into the heavy ion collision system. Moreover, these chapters will serve to document current progress on ongoing research.

While the previous chapter studied charge-independent (CI) autocorrelations, the results can be extended following the methods in chapter 4 to search for dependence on electric charge. The charge-dependent (CD) correlation measure is constructed to measure differences between the like-signed ($++$ and $--$) and unlike-signed ($+-$ and $-+$) pairs. Some physical processes are unique to a pair's relative electric charge. For example, quantum correlations only exist in like-signed pairs, while the Coulomb interaction in final-state hadrons may be either attractive or repulsive depending on the charges. Quark or lepton pair production creates nearby unlike-signed pairs, but a quark fragmenting into many hadrons, as in minijet fragmentation, may form correlations in like-signed pairs. Alternatively, processes such as momentum conservation or an effect on the system as a whole will be equally prevalent in both charge types and is expected to cancel out in the CD correlations.

Much effort has been spent on studying net-charge fluctuations in heavy ion collisions. As discussed in chapter 3, these fluctuations are related to the integral of correlations, therefore an analysis of minimum-bias CD correlations should give a much more detailed and differential study of charge distribution. The analysis of 130 GeV Au+Au data [50] found correlations that appear quite similar to the eye across all centralities, though model fits suggested a two-dimensional $(\eta_\Delta, \phi_\Delta)$ structure increasing in amplitude and narrowing with centrality. The one-dimensional structure so prevalent in p+p collisions [45] is observed to decrease, however the width of this component was fixed and fitting errors on the amplitudes range from 33.5% to $>$ 100% [61], so the behavior is largely unclear. The goal of this chapter is to use the 62 and 200 GeV Au+Au data to study in detail the energy and centrality dependences of these structures.

7.1 Autocorrelation Data

The axial CD autocorrelations for 200 GeV Au+Au collisions are shown in figure 7.1. The eleven centrality bins, which are identical to those in the CI analysis and defined in chapter 5, are arranged from most peripheral in the top left to most central in the bottom right. Compared to the CI data, it is evident that while there are fewer structures in CD correlations, these structures show an evolution with centrality which is just as dramatic. The 62 GeV results, not shown, are comparable.

Two structures are observed in axial CD autocorrelations from 200 GeV p+p collisions [45]. Longitudinal fragmentation forms a 1D Gaussian that is small and narrow in like-sign (LS) but large and broad in unlike-sign (US) pairs. Schematically CD = LS − US (see chapter 4), so this difference manifests itself as a large, broad negative 1D Gaussian related to the charge dependence of longitudinal frag-

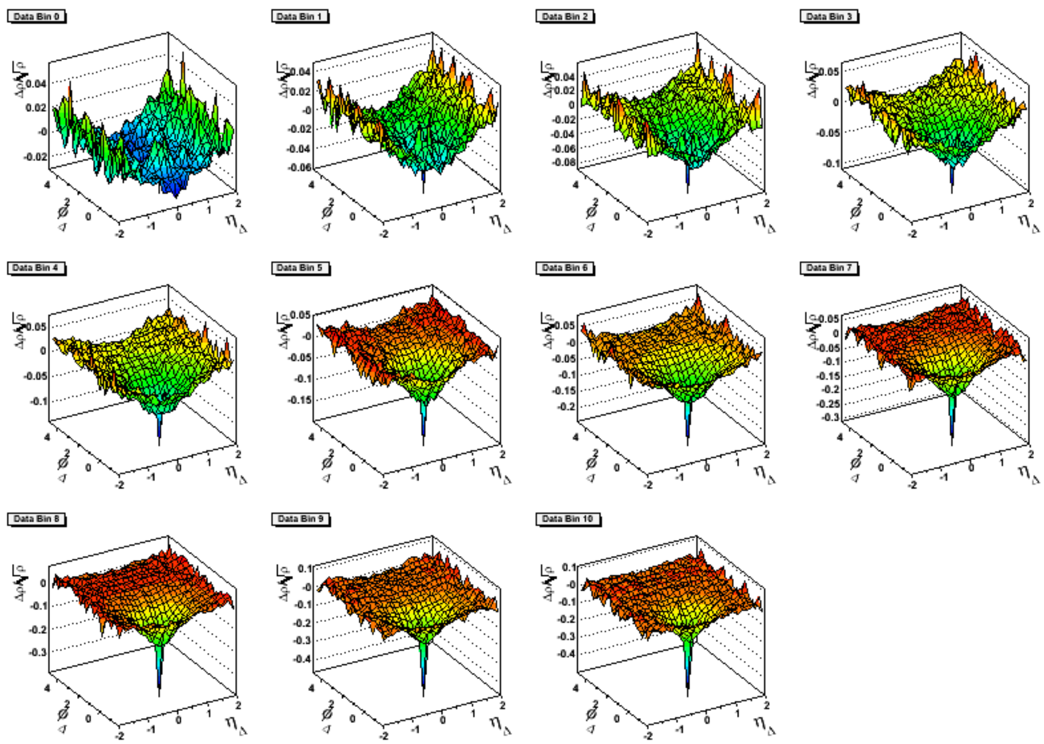

Figure 7.1: Charge-dependent axial autocorrelations in 200 GeV Au+Au from peripheral (top left) to central (bottom right) events.

mentation. The other structure is the positive peak at the $\eta_\Delta = \phi_\Delta = 0$ origin due to HBT in the LS pairs. This peak has a hole localized in the center-most bin due to electron-positron pairs causing a sharp spike in the US correlations. The analysis in [45] also includes a smaller, more elongated Gaussian at the origin due to the suppression of same-side US pairs in longitudinal fragmentation which is not considered here.

The CI results in the previous chapter showed that the HBT peak reduced in amplitude and narrowed while the 1D Gaussian followed a non-monotonic centrality dependence but was not present in central collisions. At first inspection, the CD results in figure 7.1 generally confirm these trends by showing a diminishing positive peak near the origin and a negative 1D Gaussian (most easily visible along the $\phi_\Delta = 3\pi/2$ top edge of the histogram) showing an overall decrease in amplitude. The 130 GeV analysis incorporated a negative 1D Gaussian with fixed width of 1.5 and suppressed the HBT peak by using pair cuts. Also apparent in the data is a large amplitude, negative, 2D structure at the origin. The 130 GeV analysis modeled this structure as a 2D exponential.

7.2 Fitting Procedure

Considering the CD correlations in p+p collisions, the model used in 130 GeV, and the structures observed in the data, a simple fit function was chosen for this preliminary analysis. The model function consists of a negative 1D Gaussian, a negative 2D exponential, and a constant offset. Since only the large-scale structures are of primary interest, no attempt is made to model the small positive peak at the origin. The center-most bin at $(0,0)$, dominated by background, must be excluded from the fit. In this analysis the eight neighboring bins will be excluded as well, effectively eliminating the contribution from HBT. Future studies will attempt the more delicate procedure of including terms such as a positive exponential or structures from projections of HBT analyses onto $(\eta_\Delta, \phi_\Delta)$, as well as potentially including the smaller, elongated 2D Gaussian from [45].

The model function for this analysis is defined as

$$\begin{aligned} F &= A_0 + A_1 \exp\left[-\frac{1}{2}\left(\frac{\eta_\Delta}{\sigma_1}\right)^2\right] \\ &\quad + A_2 \exp\left\{-\left[\left(\frac{\phi_\Delta}{\sqrt{2}\sigma_{\phi_\Delta}}\right)^2 + \left(\frac{\eta_\Delta}{\sqrt{2}\sigma_{\eta_\Delta}}\right)^2\right]^{1/2}\right\}. \end{aligned} \tag{7.1}$$

with offset A_0, 1D Gaussian amplitude A_1, and 2D exponential amplitude A_2. This function is essentially the same as used in the 130 GeV analysis in [50], except that the 1D Gaussian width is allowed to vary.

7.3 Fit Results

The model fits to the data are shown in figure 7.2, with the fit residuals in figure 7.3. The residuals show that the model function in equation 7.1 accommodates the large-scale correlation structure well. The only significant residuals are, as expected, the positive HBT peak at lower centralities and the negative spike from e^+e^- pairs.

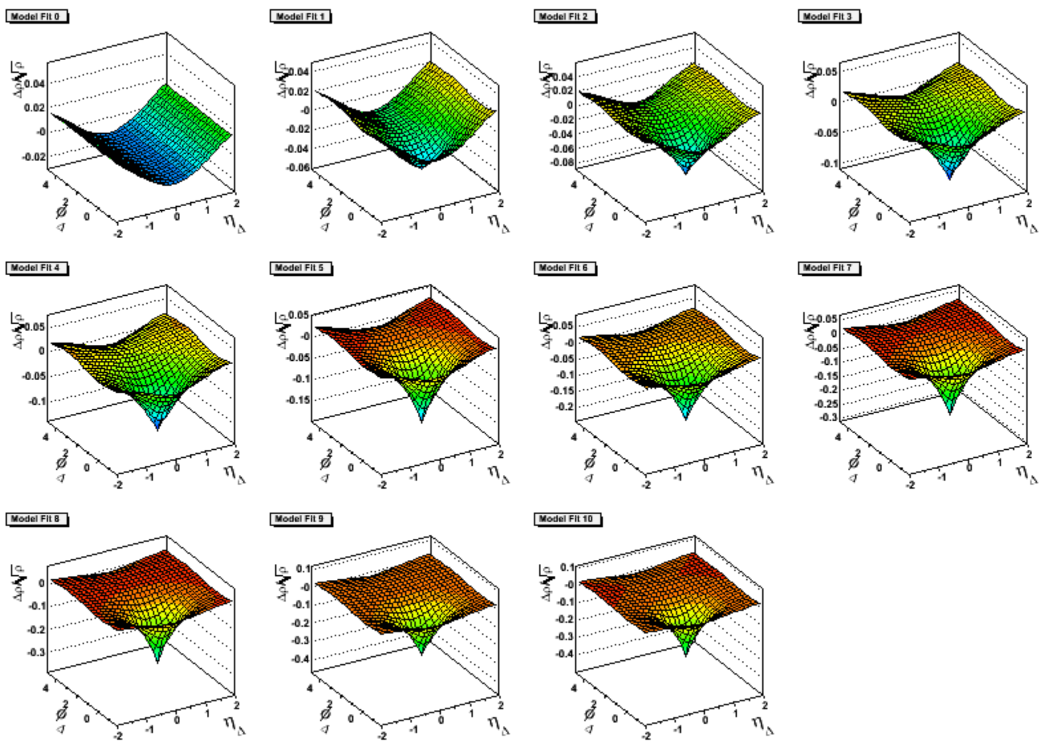

Figure 7.2: Model fits of 200 GeV data in figure 7.1.

The fit parameters for both energies are shown in figure 7.4 with 200 GeV in black, 62 GeV in red, and 130 GeV converted to $\frac{\Delta\rho}{\sqrt{\rho_{ref}}}$ in green. The horizontal axis represents centrality with (energy dependent) path length ν. The agreement

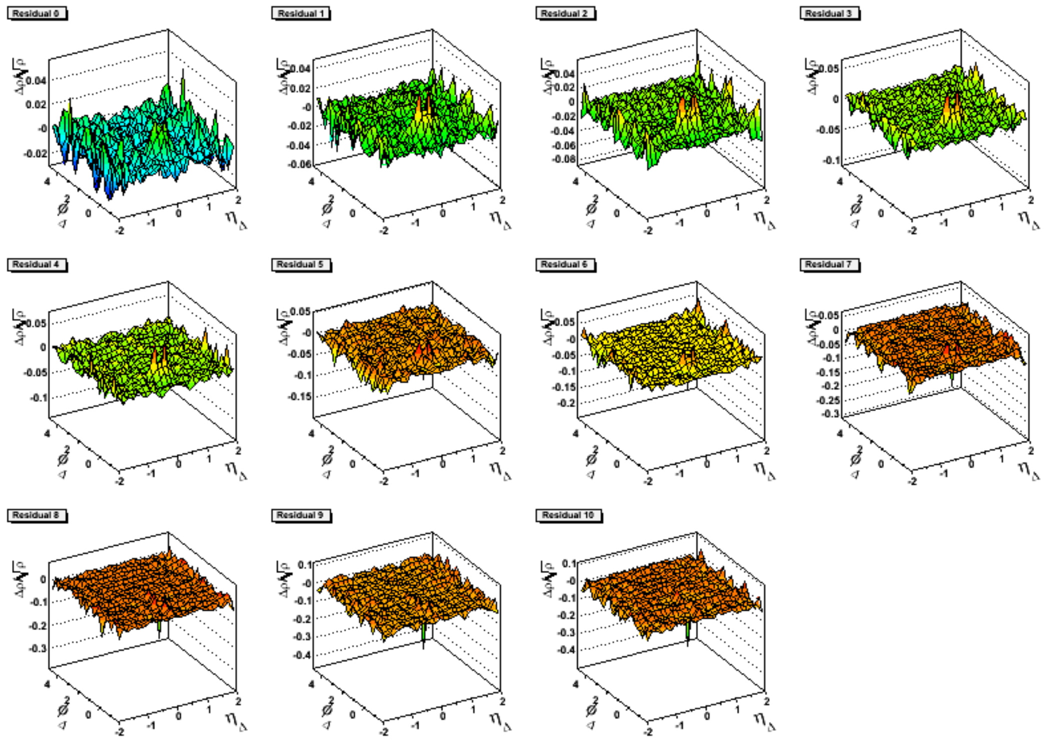

Figure 7.3: Residuals from model fits in previous figure.

among all three energies is immediately evident.

7.4 Discussion

It is first worth mentioning the structures present in CI but absent in CD correlations. Neither of the sinusoids are found in the charge-dependent correlations, meaning that the dipole and quadrupole amplitudes are equivalent for LS and US pairs. Both global (system-wide) and local (from semi-hard scattering) momentum conservation as measured by the dipole are expected to be charge-independent. The absence of a dipole in the CD correlations gives convincing evidence that the correlation measure is properly constructed and normalized between LS and US pairs.

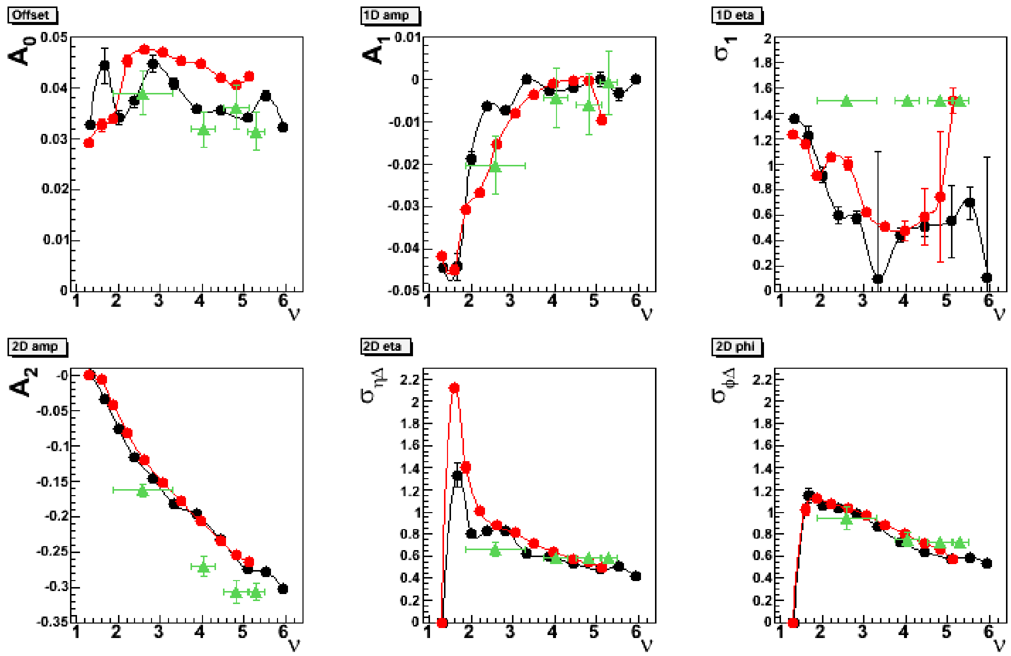

Figure 7.4: Fit parameters for axial CD autocorrelations in 62 GeV (red), 130 GeV (green), and 200 GeV (black) Au+Au collisions. First row: Offset A_0, 1D Gaussian amplitude A_1 and width σ_1. Second row: 2D exponential amplitude A_2 and widths σ_{η_Δ}, σ_{ϕ_Δ}.

This analysis provides the most precise separation of the quadrupole from other correlation sources, and the observation of the quadrupole's charge independence here is notable.

Returning to the model function components, the second and third panels in the top row of figure 7.4 show the 1D Gaussian amplitude and width. Within expected errors the amplitude monotonically approaches zero for all energies. This result contrasts with the non-monotonic 1D Gaussian amplitude in CI correlations revealing that two distinct processes contribute. A CD piece, observed here with slightly larger amplitude at 62 than at 200 GeV, diminishes in amplitude monotonically with centrality. This piece relates directly to longitudinal fragmentation as observed in p+p collisions, and as discussed in the previous chapter, it is not understood why this correlation dissipates in central heavy ion collisions. The non-monotonic portion of the CI 1D Gaussian must then come from a separate process that does not distinguish electric charge.

The widths of the CD 1D Gaussian become less well determined as the amplitude approaches zero. The centrality trends show that the assumption of a width of 1.5 taken in the 130 GeV is a reasonable approximation of the most peripheral data. However the measured widths decrease with centrality, ultimately approaching one third of the value assumed previously.

The signal of interest is the negative 2D exponential structure which dominates central collisions. The data show a small amplitude in peripheral events which increases (*i.e.* becomes more negative) approximately linearly with ν for several centrality bins, after which the rate of increase slows. The widths are not well determined in the peripheral events where the amplitude is nearly zero. The second-most peripheral bin in 62 GeV also shows unusual behavior due to the presence of a large HBT peak not accounted for in the model function. For all other centralities, the widths show a roughly linear decrease with centrality. The structure is nearly symmetric on η_Δ and ϕ_Δ, though the ϕ_Δ width is slightly larger.

7.4.1 Soft and Semi-hard Components

To help interpret this 2D exponential structure, it is instructive to consider the CD autocorrelations in proton-proton collisions, see figure 7.5. The left panel shows data including all pairs, while the other panels show a decomposition into soft ($y_{t\Sigma} \leq 3.3$) and semi-hard ($y_t \geq 2.0$ for each particle) components. The charge dependence of minijet fragmentation is shown in the right panel. As was true with longitudinal fragmentation, the signal is larger and broader in US than LS pairs. The shape more closely resembles a Gaussian than an exponential, though the best fit most likely has a non-integer exponent in between the functional forms of these two shapes. The decomposition reveals that this negative structure is buried under the positive peaks at the origin, including HBT and the elongated Gaussian in the center panel, which may only be extracted through precise fitting and careful modeling of these components. The problem is exacerbated due to the large HBT peak in p+p (also peripheral Au+Au) collisions. To summarize, these reference data show that the large, negative, approximately symmetric structure is due to minijet fragmentation, however competing correlation sources near the origin hide this signal.

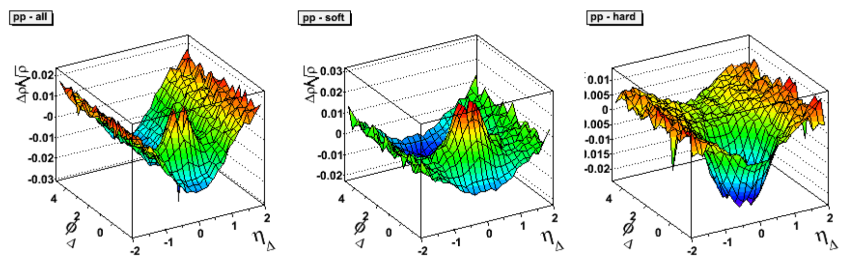

Figure 7.5: Axial CD autocorrelations in 200 GeV p+p collisions for all pairs (left panel), soft pairs (center), and hard pairs (right).

Extrapolating these results, we may hypothesize that the negative 2D exponential is due to minijet fragmentation, at least as the primary contribution. The most apparent implication is that there is no transition in the CD correlations. There are no sudden changes in either the amplitude or widths, and no places where the 62 and 200 GeV data deviate enough to allow for a transition. Consequently, there is no charge dependence to the extra particles which become associated with the minijet above the transition. The absence of a CD dipole further supports this conclusion.

To examine this feature in more detail, figure 7.6 uses the same soft and semi-hard decomposition from figure 7.5 although for 62 GeV Au+Au collisions. The top row shows selected centralities (bins 0, 3, 7, and 10) for soft pairs, while the bottom row shows hard pairs. The most peripheral events, given in the first column, closely correspond to the p+p results above (*i.e.* the center panel in figure 7.5 relates to the top-left in figure 7.6, while the right in panel in figure 7.5 relates to the bottom-left in figure 7.6). The soft pairs show the diminishing 1D Gaussian, the narrowing HBT peak (with a hole in the center from the US e^+e^- pairs), and interestingly the development of a 2D structure in central events. In contrast, the hard pairs show much less evolution with centrality. A 1D Gaussian with an approximate amplitude of 0.05 is present in all centralities. The 2D structure increases in amplitude and narrows slightly.

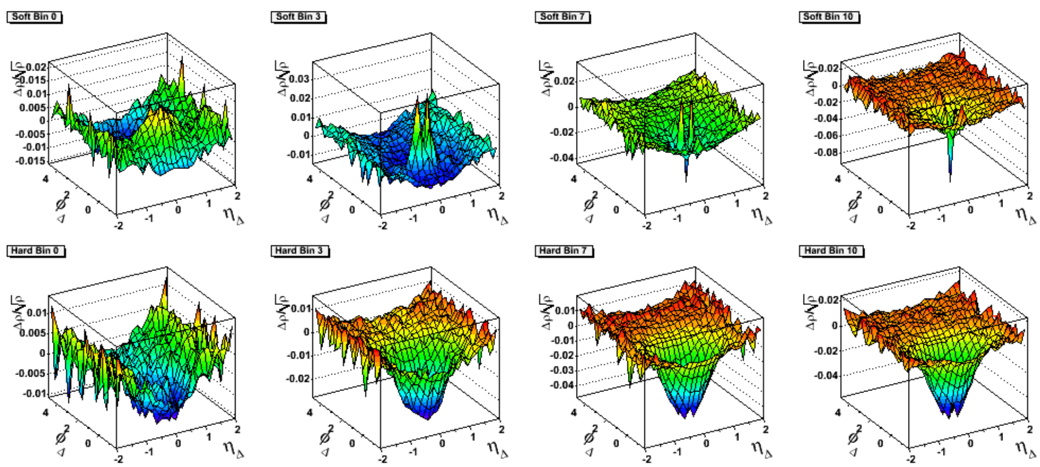

Figure 7.6: Axial CD autocorrelations in 62 GeV events for soft pairs (top row) and semi-hard pairs (bottom row). Columns show the selected centrality bins (0, 3, 7, and 10) from most peripheral (left) to most central (right) with two intermediate steps.

Since the placement of the y_t cuts should be tuned based on observed correlation structures, this decomposition is somewhat oversimplified. It is not unreasonable to expect some leakage from one component to the other. On the other hand, the possibility exists that the momentum range of certain correlations may vary with centrality. Particles may lose momentum through interactions, or may even receive a boost from a system-wide expansion which is predicted in some models. What then do we make of the presence of the 2D structure in soft pairs, or the 1D structure in hard pairs? The only solution lies in the future mapping of the detailed p_t-dependence of these structures based on the (y_{t1}, y_{t2}) correlations. For present purposes, it will suffice to note that the 2D exponential structure used in the fit function (equation 7.1) is predominately due to hard pairs, and the 1D Gaussian is due to soft pairs. This brief study of p_t-dependence may be concluded to support the above hypothesis that the 2D exponential measures minijet fragmentation in p+p as well as Au+Au collisions.

7.5 Conclusions

Returning to the y_t-inclusive data, the evolution with centrality may be seen as a natural consequence of the diminishing 1D Gaussians and narrowing HBT peaks contrasting with the increasing amplitude of the 2D exponential. In fact, it is remarkable that the correlation structures are not *more* radically altered. The hard CD correlations (figure 7.5 right and figure 7.6 bottom row) show an amplitude increase but a slow change in width from p+p collisions through the most central Au+Au collisions. This result is also found in the momentum range $0.8 \leq p_t \leq 4.0$ GeV/c [72]. The y_t-inclusive fits show a narrowing of the widths but no major modifications. Future work will determine how the amplitude compares with binary scaling expectations. Should a dense, thermalized medium develop early in central Au+Au collisions, one would expect minijet particles to undergo many successive interactions and rescattering. Neither the measured amplitudes nor widths show evidence supporting this picture.

The primary motivation for studying axial CD autocorrelations is to gain insight into the distribution of charge during hadronization. Net-charge fluctuations have been studied extensively on the expectation that a system hadronizing through a phase transition will arrange charges differently than a system of normal nuclear matter. However, fluctuations which integrate over the axial space are insensitive to the change from 1D hadronization on η_Δ to 2D on $(\eta_\Delta, \phi_\Delta)$. The so-called "balance function" [73] was designed to study 1D net-charge correlations on pseudorapidity, however it has been found to contain significant distortions and detector acceptance effects [74], and many of the assumptions behind the balance function have been called into question [75]. Regardless, the balance function has been reported to narrow with increasing centrality [76] in Au+Au collisions. The results shown in this chapter also show that the correlation structures narrow on relative η, however the ϕ_Δ and p_t dependences suggest that this due to minijet fragmentation.

In summary, the axial CD autocorrelations show that several of the features in the axial CI analysis affect like-sign and unlike-sign pairs equally. The absence of the dipole and quadrupole CD correlations is naturally expected, however the lack of a transition in minijet fragmentation (and in the corresponding dipole) is an interesting result. Instead, the 2D exponential shows a p_t-dependence and amplitude growth consistent with minijet correlations. While the widths decrease approximately by a factor of two across the full range of centrality, it is surprising that the shape of the minijet fragmentation correlations changes so little from p+p to central Au+Au events. Combining these results suggests that at the transition point, additional particles become associated with the minijet leading to a charge-independent correlation.

Chapter 8

Transverse Correlations

8.1 Introduction

The final analysis to be discussed is the measurement of transverse correlations $\frac{\Delta\rho}{\sqrt{\rho_{ref}}}(y_{t1}, y_{t2})$. This is the most preliminary analysis in this work since efficiency corrections have not been applied, and correlation histograms have not been fit to a model function. Only the 200 GeV Au+Au data set has been analyzed, so the energy dependence is not accessible. However, the available results complement the axial autocorrelations by examining the final two dimensions of the six-dimensional correlation space. One goal of this analysis aside from the general mapping of the correlation structures is to determine the momentum range of particles associated with the transition in minijet correlations.

The transverse analysis is more complex than the axial analysis for several reasons. The primary factor is the shape of the distribution for detected particles. Consider again figure 5.4 from chapter 5, where red histograms show accepted tracks. The distributions on η (top-right panel) and ϕ (bottom-left panel) are uniform within a few percent, providing a nearly constant mixed event reference which was exploited in creating an idealized reference free from detector effects. The y_t distribution (top-center panel) affords no such luxuries. Efficiency and background corrections must be applied to the final correlations bin-by-bin. These corrections, as well as the degree of correlation in the background particles, are likely to vary with beam energy and centrality, further complicating the effort. These corrections have not been attempted in this preliminary analysis.

Additionally, the shape of the y_t distribution necessitates a careful relative normalization of sibling to reference pairs. In the axial analysis, this relative factor resulted in a constant offset to the correlations which may be related to multiplicity fluctuations or simply ignored. For a transverse analysis, the relative normalization could significantly alter the observed correlation structures. A conservative approach was developed for an analysis of p+p data of adjusting the relative sibling to reference pair normalization to minimize the final correlation structure with a constraint penalizing negative bins. This procedure, essentially a χ^2 minimization of the correlations, is adopted here and described below.

These problems were avoided in the 130 GeV analysis [47] by using a transformation to $X(p_t)$ as a way to flatten the distribution. More recent studies of proton-proton correlations and single-particle spectra in p+p and Au+Au collisions have favored use of transverse rapidity y_t over $X(p_t)$, determining that the benefits of simplified structures outweigh the additional difficulties. As a final practical matter, subdividing the histograms into same-side ($|\phi_\Delta| < \pi/2$) and away-side ($|\phi_\Delta| > \pi/2$) pairs in addition to the divisions on multiplicity and event z-vertex complicates the transverse analysis beyond the axial analyses by generating a great deal more data to process.

8.2 Charge-Independent Correlations

8.2.1 Relative Normalization

The relative normalization of sibling to reference pairs in this preliminary analysis is addressed through a penalty function minimization procedure. The normalization is adjusted with a parameter β using

$$\Delta\rho = \rho_{sib} - \beta\,\rho_{ref}. \tag{8.1}$$

For each value of β the correlation $\frac{\Delta\rho}{\sqrt{\rho_{ref}}}$ is calculated and a penalty function P is assigned as

$$P = \sum_{a,b\in y_t>1.7} \lambda \frac{\Delta\rho}{\sqrt{\rho_{ref}}}(a,b)^2/\sigma(a,b)^2, \qquad \lambda = \begin{cases} 1 & : \quad \frac{\Delta\rho}{\sqrt{\rho_{ref}}}(a,b) \geq 0 \\ \alpha & : \quad \frac{\Delta\rho}{\sqrt{\rho_{ref}}}(a,b) < 0 \end{cases} \tag{8.2}$$

where $\sigma(a,b)$ is the error in bin (a,b). The sum is taken only over bins for which $y_t \geq 1.7$. The α parameter adjusts the penalty factor for negative bins in the correlation. The value $\alpha = 10$ was used in this analysis, though the results were not found to be sensitive to the particular choice of α. Overall, this minimization achieves the smallest amplitude for $\frac{\Delta\rho}{\sqrt{\rho_{ref}}}$ relative to error $\sigma(a,b)$ with the least amount of negative correlation.

In this analysis the parameter β is adjusted to minimize P. Examples of this penalty function minimization are shown in figure 8.1. The horizontal axis shows β and the vertical axis shows penalty function values. The columns show like-sign and unlike-sign pairs, respectively, while the rows show peripheral (top) and central (bottom) events. This process was performed a total of 66 times, once for the like-sign (LS) and unlike-sign (US) pairs in every individual correlation histogram (eleven centralities for the three pair types shown below).

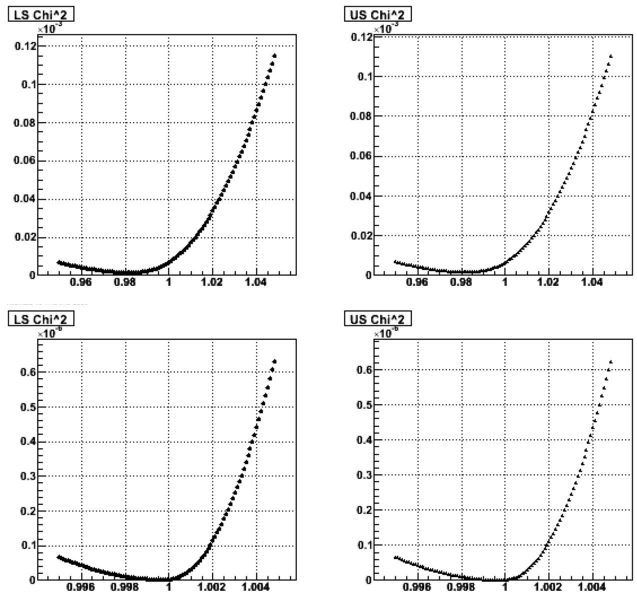

Figure 8.1: Graphs of β vs. penalty function for peripheral (top row) and central (bottom row) events. Columns show LS (left) and US (right) pairs.

8.2.2 Correlations

The charge-independent $\frac{\Delta\rho}{\sqrt{\rho_{ref}}}(y_{t1}, y_{t2})$ correlations in 200 GeV Au+Au collisions are shown in figure 8.2. The analysis uses the same eleven centrality bins as in the axial analyses, though bin 5 is omitted from the figure to conserve space. The most-peripheral bin (top-left) is similar to the p+p results shown in chapter 3 (figure 3.8) although the low-y_t soft peak is less pronounced. This correlation evolves with centrality, causing the originally distinct correlation structures to shift and merge. While the axial analyses revealed many well-defined correlation surfaces, the transverse correlations at first glance are somewhat reminiscent of a lava lamp. The mid-central bins show the development of a ridge along the $y_{t\Sigma}$ axis (the line defined by $y_{t1} = y_{t2}$ along the main diagonal). This ridge seems to begin between bins 3 and 4 (the fourth and fifth panels in the top row), where the transition in minijet

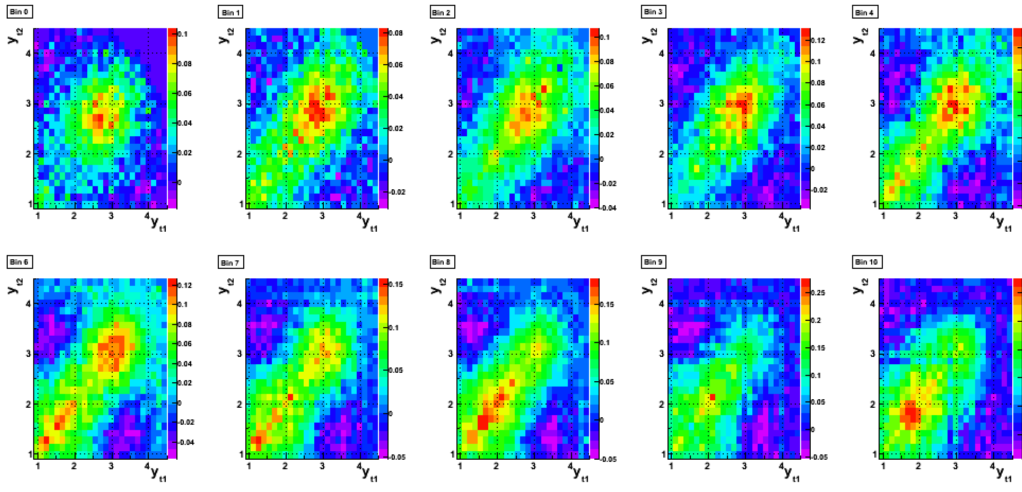

Figure 8.2: Transverse correlations in 200 GeV Au+Au collisions. Ten of the eleven centralities are pictured.

behavior was observed. There is a corresponding enhancement in correlations in the approximate region of $y_t < 2.5$ in this centrality range. The semi-hard scattering peak, near $y_t = 3$, grows in amplitude with centrality, and also appears to move to lower y_t in the most central bins.

8.3 Proton-Proton Reference

To aid in the interpretation of these data, we return to the transverse correlations in p+p collisions discussed in chapter 3, and displayed again below as figure 8.3. In general, three components contribute to these correlations. The top-left panel shows the same-side (SS) LS correlations, which are dominated by an HBT peak at low y_t. The SS US correlations (top-right panel) show a structure peaked in the semi-hard region which runs continuously into the soft component. The bottom-left panel, which shows the away-side (AS) LS pairs, gives the cleanest signal for the semi-hard component. The final panel, with AS US pairs, has an additional peak

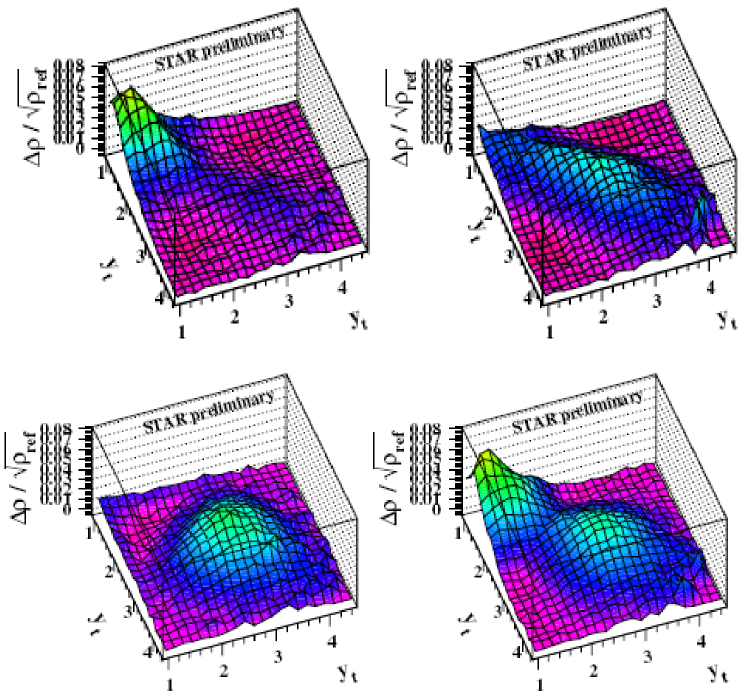

Figure 8.3: Transverse correlations in 200 GeV p+p collisions for four different cases of charge sign and opening angle. Top row: same-side; bottom row: away-side. Left column: like-sign; right column: unlike-sign. From [41].

corresponding to longitudinal fragmentation.

Using these results as our guide, we can expect to find these three primary features in the Au+Au data: the soft component with HBT in SS LS pairs and longitudinal fragmentation in the AS US pairs, and the semi-hard component best observed in the AS LS pairs. Based on binary scaling as well as axial correlation results, we would expect the longitudinal fragmentation in the soft component to diminish with increasing centrality while the semi-hard component grows and becomes dominant. The rest of this chapter is devoted to searching for these signals and comparing how the data match these expectations.

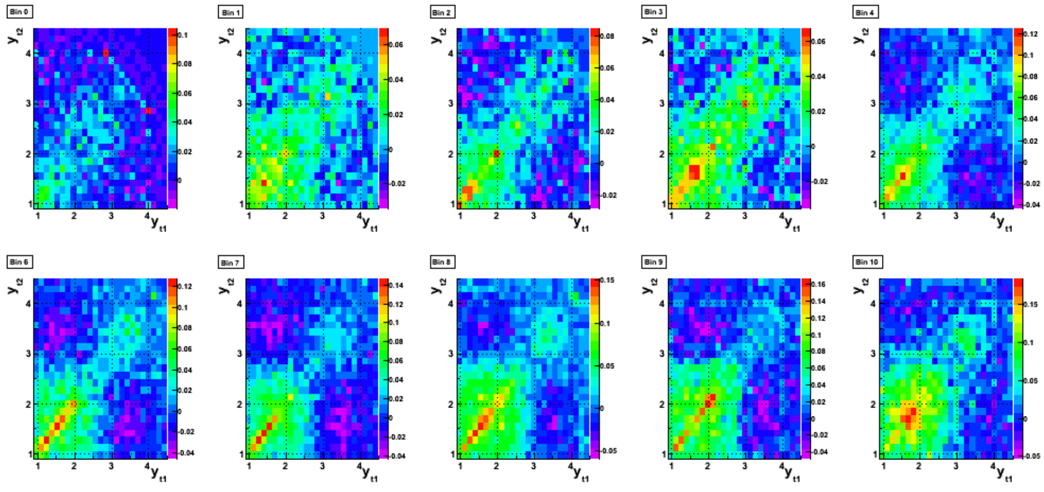

Figure 8.4: Transverse correlations in like-sign, same-side pairs.

8.4 Same-side Pairs

In p+p collisions, the like-signed same-side pairs are dominated by an HBT peak. The corresponding Au+Au correlations are shown in figure 8.4. Indeed, the largest amplitude in all centralities is localized along the main diagonal. The peak, which is a Gaussian in p+p, has become a very sharp ridge by the 70-80% (uncorrected) centrality bin in the third panel. The amplitude of this sharp ridge grows with centrality, following the same trend as the amplitude of the sharp 2D exponential in the axial CI analysis attributed to HBT (since this peak in not modeled in the CD analysis we cannot confirm this further). Based on these observations, only the very sharp ridge in the $y_{t1} = y_{t2}$ bins along the main diagonal is attributable to HBT, thus not explaining the excess low-y_t correlations from figure 8.2.

There are other soft correlations present in all centralities which grow in amplitude. To determine if this is due to HBT, we compare the unlike-sign pairs on the same-side in figure 8.5. This figure also shows significant soft correlations, which become prominent in bin 4 and above. This structure is then seen in both

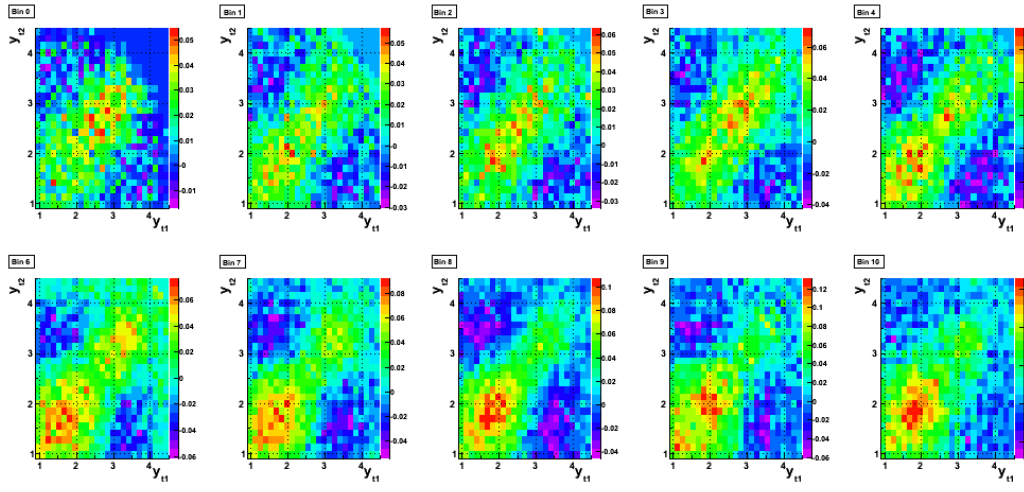

Figure 8.5: Transverse correlations in unlike-sign, same-side pairs.

LS and US pairs, and cannot be due to HBT. The SS CD correlations, not shown, suffer from large statistical noise. although they do suggest that correlations in the low-y_t region are charge-independent aside from the known contributions of HBT and longitudinal fragmentation.

8.5 Away-side Pairs

The proton-proton analysis shows that the away-side, like-sign pairs provide the cleanest signal for studying the semi-hard component. These pairs are shown for Au+Au collisions in figure 8.6. The first four panels show an isolated semi-hard component, but above the transition point (starting in the fifth panel), soft correlations arise. The semi-hard component shows a small growth in amplitude but little change in shape with centrality, while the low-y_t correlations grow much more rapidly.

The final combination of away-side, unlike-sign is shown in figure 8.7. In p+p collisions the AS LS and US differ in the soft component due to longitudinal

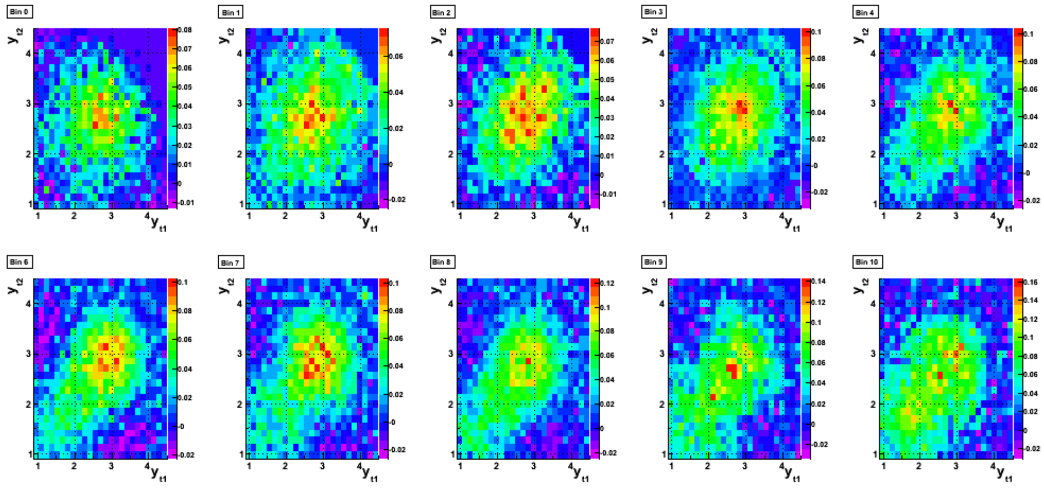

Figure 8.6: Transverse correlations in the away-side, like-sign pairs for Au+Au collisions.

fragmentation. However, this feature is hidden in Au+Au collisions by the low-y_t correlations found in both LS and US pairs. The net result is that the away-side LS and US transverse correlations are very similar in the Au+Au data.

8.6 Summary

The features found in transverse correlations in p+p collisions may be isolated and studied with cuts on relative azimuth and charge type for each pair of particles. Using the same procedure for Au+Au collisions not only revealed the centrality dependence of these features, but an additional (though not unexpected) feature as well. Comparisons with the axial CI and CD analyses aid in understanding and interpreting these results.

The soft component correlations in p+p collisions consist of HBT and longitudinal fragmentation. The HBT signal is found in same-side, like-sign pairs. The properties of the HBT peak result from the nature of quantum interference. When

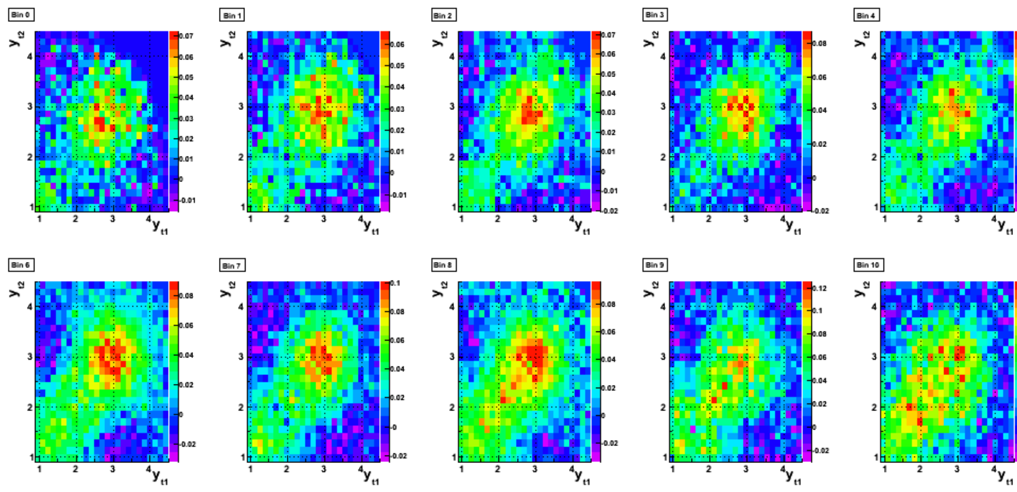

Figure 8.7: Transverse correlations in the away-side, unlike-sign pairs for Au+Au collisions.

the source size is small (considering the entire collision volume as the source of the identical particles), as in p+p collisions, the uncertainty in momentum is large. As the source size increases with increasing centrality in heavy ion collisions, the uncertainty in momentum drops reciprocally. In the axial CI analysis, the amplitude of the HBT peak increased with centrality, as would be expected for increased particle density, but the relative angular widths decreased. The same trends were observed in the transverse analysis, the amplitude increases while relative y_t range of the HBT peak decreases quickly, going from a Gaussian to a very sharp ridge along $y_{t1} = y_{t2}$ (or $y_{t\Delta} = 0$).

Longitudinal fragmentation is another primary source of soft component correlations. This feature is observed to dissipate by mid-centrality in both axial analyses. While the complete absence of this signal in central Au+Au collisions is unexpected, binary scaling predictions show that this feature should drop in amplitude relative to the semi-hard component. In p+p collisions, longitudinal fragmentation is the dominant correlation in away-side, unlike-sign, low-y_t pairs. A corresponding peak is observed for these pairs in peripheral Au+Au, though by mid-centrality it is hidden beneath correlations observed in like-sign and same-side pairs as well. Longitudinal fragmentation may only be accessible in a transverse analysis through the away-side CD correlations. These results, not shown, reveal a structure consistent with longitudinal fragmentation in the three most peripheral bins and no signal beyond the level of the substantial statistical noise at other centralities.

The semi-hard component is best isolated in p+p collisions by examining the away-side, like-sign pairs where no other correlations contribute. This correlation structure changes little from p+p to mid-central Au+Au, where additional low-y_t correlations emerge. At higher centralities, the amplitude of the semi-hard peak continues to increase slowly though no significant change in shape is observed. Meanwhile, the additional contribution at lower y_t grows in amplitude and expands in y_t range.

While the axial CI analysis shows a large increase at the transition point in same-side and away-side pairs associated with semi-hard scattering, no such transition point was found in the CD analysis. Instead, charge-dependent minijet fragmentation was observed with increasing amplitude and little change in correlation shape from p+p to central Au+Au collisions. Together, these results may suggest that minijet correlations exist at all centralities, and that the transition is due to extra particles becoming associated with the minijet. Constraints placed by the axial p_t correlations [31] discussed in chapter 3 limit the possibilities that the particles found in the transition are unrelated to minijet. This scenario would make several specific predictions for the transverse correlations studied here. First, the p_t correlations require that the particles associated with the transition have transverse momenta near, and possibly below if the negative component is included, the inclusive mean of all particles in the system. Taking $\hat{p}_t$ to be roughly 0.5 GeV/c suggests that the transverse rapidity range of the additional particles associated with semi-hard scattering is approximately $y_t < 2$. Second, the transition is observed in the axial CI analysis in both same-side pairs and away-side pairs in the dipole, so the same is expected for the transverse correlations. Third, since the axial CD analysis shows no transition, these correlations must appear in both like-sign and unlike-sign pairs. Fourth, as in the axial CD results, a semi-hard peak similar to that in p+p collisions should be found in all centralities for Au+Au collisions due to the original minijets and not the transition. To summarize, if this scenario is valid, the transverse analysis must show a low-y_t correlation for centralities above the transition point in all combinations of same-side, away-side, like-sign, and unlike-sign pairs, as well as indications of the original minijet most clearly seen in away-side, like-sign pairs. In short, the behavior of $\frac{\Delta\rho}{\sqrt{\rho_{ref}}}(y_{t1}, y_{t2})$ is almost entirely mandated by this picture; the results shown in this chapter are consistent with all four predictions of this hypothesis.

The only deviation from this picture may occur in the most central bin, where the correlation peak moves to lower y_t. The same-side axial p_t correlations show a large drop in amplitude at the highest centralities, and combined with the present results may suggest the onset of a mechanism for dissipating momentum not present at other centralities. Extending to higher energies or larger systems, such as U+U collisions, could show if these results are an insignificant coincidence or a portent of new physics to come.

It must be emphasized that these results are preliminary, and that much more work is needed before proceeding further with the interpretation. The efficiency and background corrections must be put in place. These vary relatively slowly with p_t, so these corrections are likely to cause small shifts in the peak positions and amplitudes of the correlation structures, but should not cause further significant changes. The penalty function minimization procedure must also be studied more extensively to finalize the correlations. Unlike the axial analyses, it may not be beneficial or practical to fit these correlations with a model function. Projections onto the diagonals $y_{t\Sigma}$ and $y_{t\Delta}$ may be more useful in quantifying the behavior of the correlations. The two-component spectra analysis [38] shown in chapter 3 may provide the best approach for understanding these results in detail. Using either the analytic formulae for the soft and semi-hard component spectra or the measured correlations in p+p (or peripheral Au+Au) collisions and scaling them with N_{part} and ν provides a valuable reference for these data. Deviations from this reference may yield a precise correspondence between the correlations and single-particle spectra. Such an analysis could address many remaining questions. Have the minijets lost energy, and is this energy loss related to the new particles created in the transition? Does the y_t-dependence address the high-p_t suppression and jet quenching observed in other analyses? Ultimately, the analysis of $\frac{\Delta\rho}{\sqrt{\rho_{ref}}}(y_{t1}, y_{t2})$ with identified particles may be necessary to complete this picture.

Chapter 9

Conclusion

9.1 Summary

The analysis method motivated in chapter 3 evolved from a very complicated research program of searching for critical phenomena in non-statistical fluctuations to an almost stunningly simple idea: why not just measure all of the correlations at once? All previous correlation analyses have taken the opposite approach by trying to isolate a single correlation source through projections and cuts to reduce the backgrounds to a manageable level. Each analysis method has relative strengths and weaknesses. The "top-down" approach of isolating individual sources gives a more straightforward analysis projected onto the space most convenient for that particular system, however assumptions must be made to remove other correlation sources from the signal. Additionally, this method tailors an analysis to a specific physical process, often leaving little room to search for something unexpected. On the other hand, the "bottom-up" approach provides a way to measure the relative strengths and ranges of multiple correlation sources within the same analysis. Separating one source from another is non-trivial, but a great deal of information is available. This minimum-bias method also benefits by acknowledging and utilizing the relationship between correlations in particle and heavy ion collisions to the general study of statistical correlations. Ultimately, both approaches are necessary to complete the picture. Finding correspondence between results from the top-down and bottom-up methods yields new insights and improvements to both analyses.

Despite the simplicity of the underlying idea, implementing the bottom-up analysis requires effort and care. The correlation measure must be constructed to match each set of charge types, multiplicities, and event vertices with the correct statistically uncorrelated reference and finally combine the results in way that does not introduce new bias.

The charge-independent axial autocorrelations show five distinct components, each with their own energy and centrality dependence. A same-side 2D Gaussian measures correlations between associated fragments from semi-hard scattered particles within the same minijet. The correlations follow expected trends established by scaling minijets observed in p+p collisions, and then show a dramatic increase in amplitude and η_Δ width while the ϕ_Δ width decreases with centrality. The results at 62 and 200 GeV appear to scale with transverse particle density. The $\cos(\phi_\Delta)$ dipole is also related to semi-hard scattering, and the dipole amplitude mirrors the 2D amplitude trends. The dipole also contains contributions from global momentum conservation which are insignificant in central collisions. The $\cos(2\phi_\Delta)$ quadrupole follows centrality trends observed in measures of elliptic flow. The quadrupole amplitudes show general agreement with other analyses of azimuthal anisotropy, though there are significant deviations. A sharp 2D exponential shows increasing amplitude and narrowing widths with centrality, consistent with HBT correlations. Finally, a 1D Gaussian shows unexpected energy dependence and non-monotonic behavior on centrality.

9.2 Interpretation

Ascribing physical meaning to this much data is a daunting and uncertain process. However, there are many interesting possibilities to be explored. Taking creative license to speculate about these results may be useful in exploring theoretical models and proposing future experiments.

The 2D Gaussian and dipole measurements in axial CI correlations, the 2D structure in axial CD correlations, and the semi-hard peak in transverse correlations in p+p and peripheral Au+Au firmly establishes the connection between minijet fragmentation of semi-hard scattered partons and these correlation structures. The binary scaling trends show that these minijets are almost entirely unaffected by the surrounding medium up to the transition point at mid-centrality. Measurements of high-p_t jet correlations show suppression of away-side correlations "consistent with large energy loss in a system that is opaque to the propagation of high momentum partons or their fragmentation products" [77]. More recent 2D high-p_t studies show that the same-side correlations are enhanced by the development of a "ridge" extending across several units in η [78]. Following the first observation, we would expect that this opaque medium would also strongly suppress minijets, particularly since lower momentum particles are more susceptible to large-angle deflection. This suppression would cause a decrease in minijet correlations below the expected binary scaling trends. On the other hand, the development of a same-side ridge as seen in high-p_t may or may not cause an enhancement above binary scaling, as it is presently unclear on these results alone whether the jet particles are simply redistributed or if another mechanism contributes. The high-p_t ridge does not show a corresponding increase on the away-side which is seen in the minimum-bias analysis, so even ridge formation may not account for all of the enhancement. Overall, combining a complete suppression of the away-side with only a modest enhancement of the same-side leads to the conclusion that, based on the high-p_t result, minijets will drop *below* binary scaling if the same energy loss mechanism(s) apply.

While the axial CI analysis shows a significant modification of the minijet correlations above the transition, the axial CD and transverse analyses show a significant component at all centralities which has changed little from the structures observed in p+p and peripheral Au+Au collisions. These additional analyses serve to disentangle the original minijet from the extra associated correlations above the transition. While these features are superimposed in the axial CI correlations, the axial CD analysis shows no transition and the transverse analysis shows that correlations attributed directly to the minijet and to the additional particles at the transition point occur in different momentum regions.

Therefore, instead of dissipation the minimum-bias results show that above the transition a huge increase is measured in minijet correlations above binary scaling. As argued in chapter 6, even though the observed structure is strongly modified above the transition point, the correlations are most likely still arising from minijets. This leaves two options: (1) above the transition there are suddenly more minijets, or (2) there are more particles associated with each minijet. There are many mechanisms of particle production but no likely scenarios for a sudden increase in minijet production beyond binary scaling, particularly since semi-hard scattering occurs early in the collision between partons in the original beam particles according to QCD, which are unlikely to be effected by later changes in the system. The axial p_t correlations [31], as discussed in chapter 3, further support this argument by showing no evidence for additional minijet production while suggesting the onset of correlated low-p_t particles near the transition point. Therefore, we will assume that the number of correlated particles per minijet increases, though this assumption does not require all particles to be directly created during minijet fragmentation.

Following the estimate in chapter 6, central 200 GeV Au+Au collisions have on average 17 particles associated with each minijet in two units of η, compared to about 6 in peripheral collisions. So then, where did these particles come from? First, the parton distribution functions are identical, so there is absolutely no reason to believe that the originating semi-hard scattered parton is three times more energetic in central collisions. Conservation of energy prohibits a single parton in this momentum range from fragmenting into 17 particles. Then we must consider interactions with the surrounding medium of particles, as suggested by the transverse particle density scaling. Making no assumptions about the medium's properties, if significant minijet-medium interactions caused the minijet to push out particles in the medium along with the minijet, we would expect that the multiple interactions would cause broadening of the minijet and a reduction in the minijet's transverse momentum. However, the lack of ϕ_Δ broadening and increase in p_t correlations at the transition point refute this picture.

As an alternative, there is a physical mechanism for creating particles through stimulated gluon emission which are correlated with minijets without causing additional loss of energy from the original semi-hard scattered parton. Since a gluon is a boson, a gluon in the minijet traversing an excited QCD medium might stimulate coherent gluon emission. This mechanism may also explain the particle density scaling, since the system must attain a sufficient density to provide sufficient overlap of gluon states. For maximum coherence these gluons would be in the same quantum state, and thus in the same direction as the original gluon. So while this hypothesis offers an explanation for the enhanced particle production, it does not explain the minijet η broadening. Though it may be an attractive picture for interpreting these results it incompletely describes the data, and more importantly it is merely speculation until rigorous theoretical treatment may be applied.

The research program of analyzing minimum-bias correlations undertaken here presents a great deal of data to challenge any hypothetical models. Tracing through these results again reveals a great deal about the dynamics of minijet production and fragmentation at RHIC which exclude many of the scenarios proposed to exist. First, the axial CI results show evidence for copious minijet-like correlations in Au+Au collisions producing the most dominant correlation in most centralities. Detailed analyses of the axial and transverse correlations compared to p+p collisions, model predictions, and binary scaling trends unambiguously show minijets in peripheral Au+Au collisions. While the axial CI results show a large modification to the minijet correlation structure at the transition point, the axial CD and transverse results show a significant minijet component persisting at all centralities, and that the correlations associated with the transition have several properties which differ from standard minijet fragmentation. On the other hand, the transition is observed in the axial CI analysis in the dipole as well as the same-side peak suggesting a minijet origin, while at the same time the transverse correlations along with the axial p_t correlations severely constrain the possibility that the transition is unrelated to minijets. The combined correlation results as well as simple energy conservation considerations show that the particles associated with the transition are not due to fragmentation of the original semi-hard scattered parton. Instead, the correlations from the transition are found to be charge-independent, both same- and away-side, and at low y_t, but still somehow associated with minijets. A possible physical mechanism which fits all of these criteria, particularly that of creating particles associated with the minijet without depleting the minijet's momentum, is stimulated emission. The passage of a gluon in a minijet through an excited medium may cause the medium to emit coherent gluons. In this picture, the transition correlations are charge-independent because they are not due fragmentation of a single parton, instead they are due to correlations among particles produced from the original minijet and from the stimulated gluon. Only the reverse process of an energetic parton losing energy by radiating gluons (also referred to as stimulated emission, see *e.g.* [79]) has received theoretical treatment at RHIC. The two-component spectra analysis [38] reviewed in chapter 3 shows that parton energy loss is related to the production of excess low momentum particles. Regardless, for the reasons outlined above, it is unlikely that the entire transition may be explained solely due to particles created from energy lost by the semi-hard scattered parton, though this may be a contributing factor. It is an open question if stimulated emission, by the semi-hard parton or the medium, can explain the η_Δ broadening and the y_t range of transition particles, or if another model can be found to simultaneously explain all of these results.

The asymmetry of the minijet η_Δ and ϕ_Δ widths above the transition poses a challenge to potential models. The small but significant decrease in ϕ_Δ width with centrality is difficult to interpret. Considering peripheral events, since minijets in 200 GeV collisions reach higher energy ranges it is possible that they are more tightly focused in opening angle than those in 62 GeV collisions. However, the minijet ϕ_Δ widths at 62 and 200 GeV reach the same value in central collisions. An analysis of 62 GeV p+p collisions could explore whether any potential nuclear effects are present in these correlations for peripheral Au+Au collisions. This energy dependence goes away in more central events where σ_{ϕ_Δ} for both energies is very similar to σ_{η_Δ} in peripheral events. The σ_{ϕ_Δ} trends may suggest a subtle scaling with ν, suggesting that ϕ_Δ distribution narrows with each successive collision of "wounded" nucleons. Another potential explanation is that an outward radial boost provides the focusing, however one would expect a larger boost at 200 GeV than 62 GeV, contrary to these data. The boost should also increase with centrality causing the ϕ_Δ width to become increasingly narrow, while the data show little change in ϕ_Δ width from mid-central to the most central collisions. As an additional consideration, a radial boost could also explain the disappearance of the 1D Gaussian in central collisions. In this correlation, soft hadrons of typically a few hundred MeV/c are emitted approximately uniformly on azimuth. Even a fairly modest radial boost could push these particles outward to be roughly the same azimuthal region in the lab frame, converting the 1D Gaussian to a 2D same-side Gaussian (note that the amplitudes and η_Δ widths are so small that this could not add appreciably to the signal from minijets). Again, the energy dependence is not consistent with the expected radial boost, moreover the extremely puzzling charge-independent piece of the 1D Gaussian interferes here. More work is necessary to determine whether these results provide evidence for or against radial flow.

9.3 Implications

The first striking feature about minimum-bias correlations in either proton-proton or heavy ion collisions is that there is a significant signal at all. The primary expectations were that substantial correlations only existed in higher momentum ranges, leaving a minimum-bias analysis to be dominated by soft, uncorrelated mush. The first look at correlations in 130 GeV shattered these expectations, and then a detailed analysis of p+p data allowed a close study of how many different physical mechanisms manifest themselves as correlations.

Undertaking this research program with Au+Au data is bringing a new understanding of the varied correlation sources in heavy ion collisions. It is possible to see for this first time how the relative strengths and ranges of these correlations vary with beam energy and centrality. While many of these correlations have been studied previously, no other analysis has been capable of measuring detailed jet correlations at low momenta. Minimum-bias correlations have brought pioneering methods of studying minijets, and these newly-accessible correlations have come with a great surprise. The transition in minijet correlations is unique among the experimental results at RHIC. No other analysis has shown the dramatic energy and centrality dependence of minijet correlations.

These results, coupled with single-particle spectra data, revealed the important role that semi-hard scattering plays in heavy ion collisions. By allowing multiple collisions per incident nucleon (seen by the increase of mean path length ν above one), the collision geometry trivially increases the relative fraction of semi-hard scattering. Unfortunately, this is often not accounted for in studies of transverse momentum or energy production, or in the search for outward boosts from collective expansion of the system. In this respect, the minimum-bias results presented here may be seen as a catalog of the backgrounds experienced in other analyses at RHIC. This work also shows that measurements of azimuthal anisotropy with two-particle correlations will also contain significant contributions from minijets (see also the theoretical treatment in [80]), or in reverse, measurements of jet correlations must also account for the dipole and quadrupole, though these sinusoids must be measured at higher p_t to be certain of the correspondence.

The relationship between the minimum-bias correlations and the high-p_t jet analysis, now including the ridge, will be explored by measuring the p_t-dependence of minijets and the transition. The high-p_t ridge may provide an interesting test of the stimulated gluon emission hypothesis, or conversely, the minijet transition may constrain many of the proposed models for high-p_t ridge formation. At first glance, the distinction between the jet and the ridge at large momentum matches axial CD and transverse analyses which show unique differences in the minijet and transition correlation structures. The jet and the minijet in Au+Au collisions are found to be very similar to those found in p+p collisions [78]. There are currently an insufficient number of high-p_t particles in the peripheral events, particularly in 62 GeV collisions, so show a clear onset of the ridge. Nonetheless, the transition and the ridge share many similarities, and many properties of the ridge seem consistent with stimulated gluon emission.

The abundance of semi-hard scattering observed in minimum-bias correlations has its most crucial implication in the question of thermalization at RHIC.

As discussed above, the most likely expectations suggested that minijet correlations drop below binary scaling estimates. Other studies have shown that minijets should thermalize quickly with the surrounding system, removing the observable correlation signal [81, 82]. Estimates using a gaseous quark-gluon plasma predict the mean free path of minijets to be a few fms [69]. Modern models often suggest that RHIC collisions form a strongly coupled system, in these cases the path length would certainly decrease. Regardless, these estimates predict that minijets embedded in a thermalized system will interact many times before escaping, rendering the minijet undetectable among the bulk of the system. The large drop in the minijet amplitude in p_t correlations and slight downturn in number correlations may well suggest a trend towards thermalization at higher energies, however the data show that central 200 GeV Au+Au collisions are at most partially thermalized. We are faced with the problem of determining why we observe so many minijets in a system that was previously thought to be opaque. Weighing heavily on this question is the early thermalization times required by hydrodynamics models of $\tau < 1$ fm/c, which is much less than the time it takes for light to traverse the system. Accommodating this theoretical conjecture with a physical mechanism that could provide such rapid thermalization has been a difficult challenge for theorists. The results shown here may offer a direct solution to this problem: the minimum-bias correlations suggest that thermalization, rapid or otherwise, does not occur.

The discovery of a large quadrupole moment, observed for the first time in 130 GeV Au+Au collisions by STAR, has been an important achievement for RHIC. In general, only hydrodynamics models have been able to generate a large enough quadrupole to compare with data. It is worth noting however that AMPT, a model based on partonic and hadronic scattering with no hydrodynamic evolution, is also able to produce sufficient quadrupole magnitudes to reach agreement with the data [83]. As the first generation of hydro models contained no viscosity, this agreement was the cornerstone of claims of discovering a "perfect liquid" at RHIC, often cited in the popular press and even named as the *Top Physics Story* of 2005 by the American Institute of Physics [84].

However, experimental summaries released by the STAR [25] and PHENIX [85] collaborations in the same year expressed some reservations about the applicability of hydrodynamics at RHIC. Examining the models in more detail, they are unable to reproduce measured spectra, quadrupole, and HBT data simultaneously, regardless of the large array of other RHIC results where the models do not apply. Of greater concern are the uncertainties in each component of the models. The initial conditions going from beam ions into a fluid are unclear; numerous models are invoked. Then the equation of state is also unknown, particularly when introducing viscosity. Finally, to quote the PHENIX summary, the "mapping of the fluid onto hadrons is somewhat ad hoc" [85]. Even if a particular set of assumptions and parameters is found to agree with this subset of experimental data, it does not guarantee that this model accurately reflects reality. These large uncertainties cause hydro models to lose much of their predictive power, and as a direct consequence, their ability to be falsified when confronted with data.

The STAR summary states that agreement of hydro models with spectra and quadrupole data is at the $\pm 30\%$ level, and that the assumptions and predictions such as longitudinal boost-invariance are being challenged by data [25]. Hydro models are progressing at a rapid pace, and the future matching of more precise data to more realistic, 3D viscous model predictions will be telling. Another important test will be the v_2/ϵ scaling in U+U collisions, since "it is thus unclear from the available data whether we are observing at RHIC the interesting onset of saturation of a simple physical limit particularly relevant to QGP matter, or rather an accidental crossing point of experiment with a necessarily somewhat simplified theory" [25]. Even if hydrodynamic limits are indeed imposed by nature, many features of RHIC physics lie beyond the scope of applicability of these models. The minimum-bias correlation results presented here would show this "perfect fluid" to be rife with imperfections. Ultimately, at best hydrodynamics provides an approximate description of a portion of RHIC data, and at worst a coincidental agreement with an uncertain model which has been pointing us in the wrong direction since the inception of RHIC.

Overall, the claim of thermalization is largely based on the agreement with hydro models, which may not be as secure at it would initially seem. The claim is crucial to the fundamental interpretation of RHIC data as "thermalization is viewed as a necessary condition to be dealing with a state of matter" [25]. Inversely, should new experimental evidence refute thermalization then the applicably of hydro models would be in question, as "the indirect evidence for a thermodynamic transition and for attainment of local thermal equilibrium in the matter produced at RHIC are intertwined in the hydrodynamics account for observed hadron spectra and elliptic flow results" [25]. Some recent studies have begun exploring the consequences of incomplete thermalization [86]. The minijet correlations may also show incomplete thermalization in central 200 GeV Au+Au collisions. Of the many fascinating results and exciting discoveries at RHIC, an unambiguous phase transition has not been observed. One possibility is that at these energies the collisions are not thermalized and therefore, by the condition above, do not form a well-defined state of matter. Predicted signals of phase transitions may yet be observed at higher energies upon the onset of thermalization. In many ways, the focus of RHIC has been on the discovery of an exotic new state of matter. Should we find thermalization to be untenable and many of the assumptions made before the first RHIC collision about the nature of these systems to be unfounded, the next era will hold a return to fundamental QCD physics. The community as a whole will benefit more from using RHIC to study the strong force and how it applies to extended systems than from searching for a QGP. Through the study of nuclei in extreme conditions, I am hopeful that the legacy of RHIC will be the time when physicists learned how to apply non-perturbative QCD to the fundamental building blocks of matter.

9.4 Future Work

This survey of the energy and centrality dependences of correlation structures in Au+Au collisions at RHIC invites many opportunities for future studies. Using data from previous RHIC runs, the next logical step is to perform this analysis on data from 62 and 200 GeV Cu+Cu collisions to map the beam species dependence. Do the minijet correlations show a transition in Cu+Cu? If so, does transverse particle density scaling hold? Quadrupole measurements in these collisions may help address the large systematic error incurred in conventional elliptic flow studies, while the puzzling behavior of longitudinal fragmentation can be further explored. Additionally, the very large event sample in 200 GeV Au+Au collisions in run 4 adds nearly an order of magnitude more data to the sample analyzed here. It will be possible to measure the p_t and y_t dependence of the axial correlations, isolating the transition point and map the evolution of minijets into jets. There is also interest in the p_t dependence of the quadrupole. Going farther back, the d+Au data of run 3 could provide an alternative reference to p+p collisions with normal nuclear matter.

The preliminary axial CD and transverse analyses offer a first look at the comprehensive correlation structures in Au+Au collisions. In the axial CI study, the minijet and transition correlations are superimposed together, while the complementary analyses allow us to disentangle these correlations. These studies, when complete, will provide more information on the nature of the correlations associated with the transition as well as the originating minijet. Additionally, the axial CD analysis will further study the relationship of the axial autocorrelations to HBT effects and net-charge fluctuations. The transverse correlations will show in detail the extent of energy loss suffered by the minijet, if any, and how that energy is manifested at lower y_t.

The future of RHIC and STAR offers many new possibilities. The time-of-flight upgrade promises a vast array of identified particle data. This correlation analysis can carefully study production of particle species and individual quark flavors to study the anomalous baryon to meson ratio in intermediate p_t regions. The coming years will offer U+U collisions at extremely high energy density, as well as a survey of low energy Au+Au collisions where the onset of observable minijet production may be measured.

Certainly, the physics program at RHIC has been more challenging than some initial conceptions. Instead of finding an unambiguous, "smoking gun" phase transition in the first year's data, we are now beginning to explore a rich and complex system. Just as hadron gas models failed to describe SPS data, the properties observed at RHIC defied description in terms of the gaseous quark-gluon plasma envisioned at the time [26]. Some, but no means all, of the measurements at RHIC may be approximately fit by a hydrodynamic model. Time will tell whether precise measurements and new calculations will improve the agreement or cause hydro models to pass the way of the gaseous QGP. This list of failures is quite exciting from a scientific standpoint since each system brought new discoveries and new insights, and progress was made by falsifying old models. The minimum-bias correlation analysis offers a new era in precise, differential measurements, which offer new challenges to our understanding, and hopefully, another step in the progress of science.

Bibliography

[1] W.-M. Yao *et al.*, *Journal of Physics G* **33** 1 (2006).

[2] M. Miller, *et al.*, *Annu. Rev. Nucl. Part. Sci.* **57** 205 (2007).

[3] M. Stanley Livingston and John P. Blewett, *Particle Accelerators* (New York: McGraw Hill, 1962).

[4] R. P. Crease, *Physics in Perspective* **7** 330 (2005).

[5] R. P. Crease, *Physics in Perspective* **7** 404 (2005).

[6] William J. Broad, *New York Times* July 14 1983.

[7] T. D. Lee, *Rev. Mod. Phys.* **47** 267 (1975).

[8] T. Ludlam, *Nucl. Phys. A* **750** 929 (2005).

[9] N. P. Samios, *J. Phys. G: Nucl. Part. Phys.* **34** S181 (2007).

[10] M. Harrison, T. Ludlam, S. Ozaki, *Nucl. Inst. and Methods A* **499** (2003) 235.

[11] *RHIC Design Manual*, currently available at: `http://www.agsrhichome.bnl.gov/NT-share/rhicdm/`.

[12] M. Harrison, S. Peggs, and T. Roser, *Annu. Rev. Nucl. Part. Sci.* **52** 42569 (2002).

[13] *Run overview of the Relativistic Heavy Ion Collider*,
http://www.agsrhichome.bnl.gov/RHIC/Runs/

[14] PHOBOS Collaboration, B. Back, *et al.*, *Phys. Rev. Lett.* **88** (2002) 022302.

[15] PHENIX Collaboration, K. Adcox, *et al.*, *Phys. Rev. Lett.* **87** (2001) 052301.

[16] K. H. Ackermann, *et al.*, *Nucl. Inst. and Methods A* **499** (2003) 634.

[17] F. S. Bieser, *et al.*, *Nucl. Inst. and Methods A* **499** (2003) 766.

[18] C. Adler, *et al.*, *Nucl. Inst. and Methods A* **499** (2003) 433.

[19] C. Adler, *et al.*, *Nucl. Inst. and Methods A* **499** (2003) 778.

[20] J. M. Landgraf , *et al.*, *Nucl. Inst. and Methods A* **499** (2003) 762.

[21] M. Anderson, *et al.*, *Nucl. Inst. and Methods A* **499** (2003) 659.

[22] F. Bergsma, *et al.*, *Nucl. Inst. and Methods A* **499** (2003) 633.

[23] J. Abele, *et al.*, *Nucl. Inst. and Methods A* **499** (2003) 692.

[24] *New State of Matter created at CERN*,
http://info.web.cern.ch/Press/PressReleases/Releases2000/PR01.00EQuarkGluonMatter.html

[25] STAR Collaboration, J. Adams, *et al.*, *Nuclear Physics A* **757** 102 (2005).

[26] M. J. Tannenbaum, *Rep. Prog. Phys.* **69** 2005 (2006).

[27] M. Stephanov, K. Rajagopal, E. Shuryak, *Phys. Rev. D* **60** 114028 (1999).

[28] STAR Collaboration, J. Adams, *et al.*, *Phys. Rev. C* **71** 064906 (2005).

[29] NA49 Collaboration, H. Appelshäuser , *et al.*, *Phys. Lett. B* **459** 679 (1999).

[30] CERES Collaboration, D. Adamová, *et al.*, *Nucl. Phys. A* **727** 97 (2003).

[31] STAR Collaboration, J. Adams, *et al.*, *J. Phys. G* **32** L37 (2006).

[32] K. Pearson, *Phil. Trans. Royal Soc.* **187** 253 (1896).

[33] R. Hanbury Brown and R. Q. Twiss, *Nature* **177** 27 (1956).

[34] T. A. Trainor, R. J. Porter, D. J. Prindle, *J. Phys. G* **31** 809 (2005).

[35] D. Kharzeev and M. Nardi, *Phys. Lett. B* **507** 121 (2001).

[36] T. Sjöstrand, *et al.*, *JHEP* **05** 026 (2006).

[37] X.-N. Wang and M. Gyulassy, *Phys. Rev. D* **44** 3501 (1991).

[38] T. Trainor, arXiv:0710.4504v1 [hep-ph] (2007)

[39] STAR Collaboration, J. Adams, *et al.*, *Phys. Rev. D* **74** 032006 (2006).

[40] G. Wilk and Z. Włodarczyk, *Phys. Rev. Lett.* **84** 2770 (2000).

[41] R. J. Porter and T. A. Trainor, *J. of Phys.: Conf. Ser.* **27** 98 (2005).

[42] M. Lisa, *et al.*, *Ann. Rev. Nucl. Part. Sci.* **55** 357 (2005).

[43] T. A. Trainor and D. J. Prindle, *J. of Phys.: Conf. Ser.* **27** 134 (2005).

[44] B. Andersson, *et al.*, *Phys. Rep.* **97** 31 (1983).

[45] R. J. Porter and T. A. Trainor, arXiv:hep-ph/0406330v1 (2004)

[46] X.-N. Wang and M. Gyulassy, *Phys. Rev. Lett.* **68** 1480 (1992).

[47] STAR Collaboration, J. Adams, *et al.*, *J. Phys. G* **34** 799 (2007).

[48] STAR Collaboration, J. Adams, *et al.*, *Phys. Rev. C* **73** 064907 (2007).

[49] STAR Collaboration, C. Adler, *et al.*, *Phys. Rev. C* **66** 034904 (2002).

[50] STAR Collaboration, J. Adams, *et al.*, *Phys. Lett. B* **634** 347 (2006).

[51] STAR Collaboration, J. Adams, *et al.*, *J. Phys. G* **34** 451 (2007).

[52] T. A. Trainor and D. T. Kettler, arXiv:0704.1674 [hep-ph] (2007).

[53] A. Einstein *Ann. Phys.* **17** 549 (1905).

[54] D. J. Prindle and T. A. Trainor, *J. of Phys.: Conf. Ser.* **27** 118 (2005).

[55] PHOBOS Collaboration, B. B. Back, *et al.*, *Phys. Rev. C* **74**, 021901(R) (2006).

[56] PHOBOS Collaboration, B. B. Back, *et al.*, *Phys. Rev. Lett.* **91** 052303 (2003).

[57] STAR Collaboration, J. Adams, *et al.*, *Phys. Rev. Lett.* **92** 112301 (2004).

[58] T. A. Trainor and D. J. Prindle, arXiv:hep-ph/0411217v3 (2007).

[59] M. Miller, *et al.*, *Ann. Rev. Nucl. Part. Sci.* **57** 205 (2007).

[60] R. L. Ray and M. Daugherity, arXiv:nucl-ex/0702039 (2007).

[61] A. Ishihara, Ph. D. Dissertation, University of Texas at Austin (2004).

[62] Weisstein, Eric W. *"Convolution."* From MathWorld–A Wolfram Web Resource. `http://mathworld.wolfram.com/Convolution.html`

[63] Rene Brun and Fons Rademakers, *Nucl. Inst. and Methods A* **389** 81 (1997). See also `http://root.cern.ch`.

[64] L. Molnar, Ph. D. Dissertation, Purdue University (2006).

[65] J. D. Bjorken, *Phys. Rev. D* **27** 140 (1983).

[66] STAR Collaboration, J. Adams, *et al.*, *Phys. Rev. C* **70** 054907 (2004).

[67] PHENIX Collaboration, S. S. Adler, *et al.*, *Phys. Rev. C* **71** 034908 (2005).

[68] Z. Chajecki and M. Lisa, arXiv:0803.0022 [nucl-th] (2008).

[69] K. Kajantie, *et al.*, *Phys. Rev. Lett.* **59** 2527 (1987).

[70] STAR Collaboration, J. Adams, *et al.*, *Phys. Rev. C* **72** 014904 (2005).

[71] STAR Collaboration, J. Adams, *et al.*, *Phys. Rev. Lett.* **92** 112301 (2004).

[72] STAR Collaboration, B. Abelev, *et al.*, arXiv:0806.0513v1 [nucl-ex] (2008).

[73] S. A. Bass, *et al.*, *Phys. Rev. Lett.* **85** 2689 (2000).

[74] S. Pratt and S. Cheng, *Phys.Rev. C* **68** 014907 (2003).

[75] T. A. Trainor, arXiv:hep-ph/0301122v1 (2003).

[76] STAR Collaboration, C. Adler, *et al.*, *Phys. Rev. Lett.* **90** 172301 (2003).

[77] STAR Collaboration, C. Adler, *et al.*, *Phys. Rev. Lett.* **90** 082302 (2003).

[78] J. Putschke, arXiv:nucl-ex/0701074 (2007).

[79] E. Wang and X.-N. Wang, *Phys. Rev. Lett.* **87** 142301 (2001).

[80] Y. V. Kovchegov and K. L. Tuchin, *Nucl. Phys. A* **708** 413 (2002).

[81] G. C. Nayak, *et al.*, *Nucl. Phys. A* **687** 457 (2001).

[82] G. R. Shin and B. Müller *J. Phys. G: Nucl. Part. Phys.* **29** 2485 (2003).

[83] Zi-Wei Lin, *et al.*, *Phys. Rev. C* **72** 064901 (2005).

[84] P. Schewe and B. Stein, *Physics News Update* **757** 1 (2005).

[85] PHENIX Collaboration, K. Adcox, *et al.*, *Nuclear Physics A* **757** 104 (2005).

[86] R. S. Bhalerao, *et al.*, arXiv:nucl-th/0508009 (2005).

Vita

Michael Scott Daugherity was born to Louis and Mary Daugherity in Oklahoma City, Oklahoma on March 6, 1979. After graduating Putnam City West High School in Bethany, OK in 1997, he received dual Bachelor of Science degrees in Physics and Computer Science from Abilene Christian University in Abilene, TX in May 2002. During this time, he married Elizabeth Ann Hull on May 21, 2000. He continued his education at the University of Texas at Austin enrolling in August 2002 and advancing to doctoral candidacy in October 2004, one month before his daughter, Molly Ann Daugherity, was born.

Permanent Address: 2265 Continental Ave
Abilene, TX 79601

This dissertation was typeset with LaTeX 2_ε[1] by the author.

[1] LaTeX 2_ε is an extension of LaTeX. LaTeX is a collection of macros for TeX. TeX is a trademark of the American Mathematical Society. The macros used in formatting this dissertation were written by Dinesh Das, Department of Computer Sciences, The University of Texas at Austin, and extended by Bert Kay, James A. Bednar, and Ayman El-Khashab.